



Salih, Jalal Mohammed (2016) *Quantitative atomic resolution characterisation of internal interfaces in doped bismuth ferrite*. PhD thesis.

<http://theses.gla.ac.uk/8283/>

Copyright and moral rights for this work are retained by the author

A copy can be downloaded for personal non-commercial research or study, without prior permission or charge

This work cannot be reproduced or quoted extensively from without first obtaining permission in writing from the author

The content must not be changed in any way or sold commercially in any format or medium without the formal permission of the author

When referring to this work, full bibliographic details including the author, title, awarding institution and date of the thesis must be given

Enlighten:Theses  
<http://theses.gla.ac.uk/>  
theses@gl.a.ac.uk

Quantitative atomic resolution  
characterisation of internal interfaces in  
doped bismuth ferrite

Jalal Mohammed Salih



University  
of Glasgow

Presented as a thesis for the degree of Ph.D. at the  
school of Physics and Astronomy, University of Glasgow

February 2016

© J. M. Salih 2016

# Acknowledgements

I would like to take this opportunity to thank deeply my supervisors Dr. Ian MacLaren and Prof. Robert Stamps for their invaluable support during my PhD project.

I would also like to thank the HCDP team who provided this invaluable opportunity as well as funded me through my study and my project.

I am also grateful to all other members within the MCMP group and all the colleagues who stayed together specially in room 408 for making my study time so enjoyable and memorable.

I am deeply indebted to my parents and siblings with their support and prayers, this project could not be done without their continuous support.

In particular, I would like to thank my wife and my daughters Shazad and Shadan. Writing this thesis would not have been possible without them.

# Declaration

This thesis is a record of the work carried out by myself in the Materials and Condensed Matter Physics (MCMP) Group under the supervision of Dr Ian MacLaren and Prof. Robert Stamps of the School of Physics and Astronomy at the University of Glasgow during the period 2012 - 2016. The work described herein is my own work except where otherwise stated: The NCSI HRTEM images were taken at Jülich performed by Dr Lei Jin (Ernst-Ruska Centre, Forschungszentrum Jülich). HRSTEM images were taken at the SuperSTEM facility using a Nion UltraSTEM by Prof. Quentin M. Ramasse and initial data-processing was performed by Dr LiQiu Wang. The simulation results presented in this thesis were performed by Dr Juri Barthel (Forschungszentrum, Germany). The local distortions have been removed from the HRSTEM images using Smart align by Dr L Lewys Jones.

This thesis has not previously been submitted for a higher degree.

Some parts of the work have been published in the following papers:

J. M. Salih, L. Wang, Q. M. Ramasse, L. Jones, J. Barthel, I. M. Reaney, A. J. Craven, and I. MacLaren “Maghemite-like regions at crossing of two antiphase boundaries in doped  $\text{BiFeO}_3$ ”, *Materials Science and Technology* 32 (2016), 242-247.

# Contents

<b>1</b>	<b>Introduction</b>	<b>1</b>
1.1	Multiferroics concept . . . . .	4
1.2	Ferroelectric state . . . . .	6
1.2.1	Curie-temperature and phase transitions dependent in ferro- electrics . . . . .	6
1.2.2	Domain formation in Ferroelectric structures . . . . .	8
1.2.3	Ferroelectricity in perovskite structures . . . . .	11
1.3	Ferromagnetism . . . . .	14
1.3.1	Hysteresis in magnets . . . . .	15
1.3.2	Magnetic ordering in perovskites . . . . .	16
1.3.3	Magnetoelectric coupling . . . . .	18
1.4	A review of structural studies of BiFeO <sub>3</sub> and its derivatives . . . . .	19
<b>2</b>	<b>Instruments and sample preparation</b>	<b>23</b>
2.1	Introduction . . . . .	23
2.2	The basic principles of transmission electron microscopy . . . . .	24
2.2.1	The Basic Principles of Scanning Transmission Electron Mi- croscopy . . . . .	27
2.2.2	Electron sources . . . . .	28
2.2.3	Electron lenses aberrations and corrections . . . . .	30
2.3	Imaging mode . . . . .	43

2.3.1	Diffraction contrast TEM . . . . .	43
2.3.2	Phase contrast HRTEM . . . . .	45
2.3.3	STEM Imaging mode . . . . .	51
2.4	Electron Energy Loss Spectroscopy (EELS) . . . . .	56
2.4.1	Elastic scattering . . . . .	57
2.4.2	Inelastic scattering . . . . .	58
2.4.3	Electron energy-loss spectroscopy (EELS) . . . . .	58
2.4.4	EELS spectra . . . . .	59
<b>3</b>	<b>Computational software and data preparation methods</b>	<b>63</b>
3.1	Introduction . . . . .	63
3.2	Alignment of multiple STEM images . . . . .	64
3.2.1	Simple rigid registration . . . . .	65
3.2.2	Non-rigid image registration . . . . .	67
3.3	Atom column position measurements . . . . .	67
3.4	Image simulation . . . . .	69
3.4.1	Multislice method . . . . .	70
3.4.2	Frozen phonon image simulation . . . . .	72
3.4.3	Dr. Probe - High-resolution (S)TEM image simulation package	74
3.5	EELS analysis . . . . .	76
3.5.1	Quantification . . . . .	76
3.5.2	Principal Component Analysis (PCA) . . . . .	77
3.6	Conclusion . . . . .	80
<b>4</b>	<b>Imaging polarisation around charged antiphase boundaries</b>	<b>81</b>
4.1	Introduction . . . . .	81
4.2	Quantification of the differences between HRTEM and HRSTEM for imaging polarisation around charged planar APBs . . . . .	83
4.2.1	Atomic column position determination . . . . .	83

4.2.2	Quantitative comparison of HRTEM and HRSTEM images of the same kind of APB . . . . .	84
4.2.3	Determining imaging parameters for HRTEM . . . . .	88
4.2.4	The effects of surfaces on HRTEM . . . . .	96
4.2.5	The effect of thickness on apparent atom positions in HRSTEM	103
4.3	The reliability of polarisation calculations from atomic resolution imaging in the electron microscopy . . . . .	107
4.4	Discussion and conclusion . . . . .	110
<b>5</b>	<b>Novel structures at the junctions of antiphase boundaries (APBs)</b>	<b>111</b>
5.1	Introduction . . . . .	111
5.2	STEM imaging of the crossing of APBs . . . . .	112
5.2.1	Quantitative analysis of a non-rigid registration procedure . .	114
5.2.2	Finding atom positions after non-rigid registration . . . . .	120
5.2.3	Atomic resolution chemical analysis . . . . .	121
5.2.4	Reconstructing the 3D model of the cross . . . . .	122
5.2.5	Model validation via image simulation . . . . .	126
5.2.6	Discussion . . . . .	131
5.3	Quantification of the structures of 90° corners on APBs . . . . .	133
5.3.1	The 3D model of the corner APBs . . . . .	135
5.4	Conclusion . . . . .	138
<b>6</b>	<b>Summary and future work</b>	<b>139</b>
6.1	Summary . . . . .	139
6.2	Future work . . . . .	142

# List of Figures

1.1	The unit cell of a simple cubic perovskite, with the composition $ABO_3$ , where red is used for O atoms, magenta for A-sites, and orange-yellow for B-sites. . . . .	3
1.2	A 3D corner shared network of $FeO_6$ octahedra, red is used for O atoms, magenta for A-sites, and orange-yellow for B-sites. . . . .	3
1.3	A schematic diagram showing Multiferroic materials that combine the ferroelectric and magnetism properties. Ideally, the magnetization of a ferromagnet in a magnetic field displays the usual hysteresis loop (pink), and ferroelectrics have a similar response to an electric field (blue). The multiferroics can be created that are simultaneously ferromagnetic and ferroelectric (green), which is a magnetic response to an electric field, or, vice versa. . . . .	5
1.4	A schematic diagram of relative permittivity of $BaTiO_3$ changes with the temperature displaying various phase transitions. When the ideal cubic system is cooled, the resulting structures are tetragonal, orthorhombic, and rhombohedral systems, respectively. . . . .	7
1.5	A schematic diagram of $90^\circ$ domain structures, as seen in simple tetragonal ferroelectrics like $BaTiO_3$ and Ti-rich $Pb(Zr,Ti)O_3$ . Spontaneous polarisation directions of the domains are shown by arrows. . . . .	9
1.6	A schematic diagram of ferroelectric hysteresis loop (Polarisation (P) <i>vs.</i> Electric field (E)).[22] . . . . .	10

1.7	A schematic drawing of the $\text{BiFeO}_3$ crystal structure where the direction of the ferroelectric polarisation by an arrow is shown in the figure [25]. The motion of the A-site is shown by red arrow. Red is used for O atoms, magenta for A-sites, and orange-yellow for B-sites.	12
1.8	A schematic diagram of the perovskite unit cell of $\text{PbZrO}_3$ which displays the behaviour of the crystal distortion due to the shifting Pb ions, Pb ions are marked in red, Zr ions in yellow, and O ions in cyan. The unit cell splits into two halves with Pb ions shifted in opposite directions resulted in formation of the polarisation trends that denoted by arrows up and down in each half of the cell [30]. . . .	14
1.9	Ordering possibility of the magnetic dipoles in the magnetic materials:(a) Paramagnetic; (b) Ferromagnetic; (c) Antiferromagnetic; (d) Ferrimagnetic.[8] . . . . .	15
1.10	A schematic diagram of G-type AFM structure where the direction of the magnetic orderings is shown by arrows. The polarisation axis of Fe (B-site) cations is along $[111]_{pc}$ and $[110]_{hex}$ directions. Red is used for O atoms, magenta for A-sites, and orange-yellow for B-sites.	17
1.11	The corresponding evolution of $c/a$ of the pseudocubic cell as a function of biaxial strain or substrate lattice parameter. [58] . . . . .	20
1.12	Phase diagram for $\text{Bi}_{1-x}\text{Nd}_x\text{FeO}_3$ presented using XRD, DSC, Raman, and TEM data together [27]. . . . .	22
2.1	Schematic diagram of the FEI Tecnai T20 TEM illustrating the illumination and magnification system, SIS camera and Gatan Image Filter (GIF), which are utilised to generate energy filtered images and EELS spectra. . . . .	25

2.2	A schematic diagram of the main components of an aberration-corrected STEM. Starting with an electron gun at the top that ultimately forms a nanoprobe that is focused on the specimen after a series of aberration correctors. A quadrupole lens module (QLM) is used for coupling the corrector electron-optically to the objective lenses. A quadrupole-octupole coupling module (QOCM) is used for optimised coupling of inelastically scattered electrons into the spectrometer. . . . .	28
2.3	A schematic diagram of thermionic (LaB <sub>6</sub> ) gun. Once a high voltage is applied between the cathode and the anode plates, the Wehnelt converges the electrons into a crossover. The electrons are then controlled and passed into the TEM illumination system [72]. . . . .	30
2.4	A schematic diagram of a pole-piece structure as well as the change in the direction of rays passing through the lens due to the radial component ( $\mathbf{B}_R$ ) of the magnetic field. . . . .	32
2.5	A schematic illustration of spherical aberration, where the off-axis rays are not focused at the same point in the Gaussian plane. . . . .	34
2.6	A schematic ray diagram illustrating axial astigmatism. Since the effect of the magnetic field is not the same in the x and y directions, rays may travel in the x-z plane with the long axis normal to the y-z plane resulting in an ellipse centered around the $F_x$ point or vice versa around $F_y$ , or into a circle of smallest radius (the disc of least confusion) [75]. . . . .	35
2.7	A schematic diagram of a comet-shaped aberration due to rays that travel near the optic axis, which results in off-axis rays being focused at different points. . . . .	35
2.8	A schematic ray diagram of the quadrupole-octupole corrector. The radial elongation of the beam through the corrector is indicated along two orthogonal x and y axes [85]. . . . .	38

2.9	A schematic diagram of a common CCD camera that is used in TEM [72]. . . . .	42
2.10	A schematic ray diagram showing the formation of BF and DF images after the direct beam interacts with a specimen. a) A BF imaging mode formation from the direct beam. b) A DF imaging mode formed from a specific diffracted beam selected by setting the objective aperture. c) A DF imaging mode formed by tilting the incident electron beam which in turn displays the scattered beam on axis. On the viewing screen under each ray diagram, the area of interest of a specimen is selected and displayed by the objective aperture in microscopy. . .	44
2.11	A schematic diagram of $\sin \chi$ curves calculated for different values of $\Delta f_{Sch}$ , at values of -30, -50 and -70, respectively. . . . .	47
2.12	A schematic diagram of $\sin(\chi)$ vs $\alpha$ displaying the CTF as a function of $\sin(\chi)$ within an uncorrected TEM. This has been calculated for the CM300 at NCEM (Berkeley, CA, USA), $C_s = 0.6\text{mm}$ and an accelerating voltage of $300\text{keV}$ ( $\lambda = 1.97\text{pm}$ ) result in Scherzer defocus = $-41.25\text{nm}$ . The maximum allowable spatial frequency, which gives intuitive image understanding, is determined by the first crossover. $E_t$ and $E_s$ represent the chromatic aberration and the spatial coherence envelopes, respectively. In fact, the parameters for the CM300 are exactly the same as those for an uncorrected TITAN 80-300, so this graph illustrates well the performance available on one microscope used in this research prior to aberration correction. . . . .	48

2.13	Amplitudes and phases in the Gaussian image plane illustrating phase contrast in a (WPO). $V_{in}$ is pointing along the real axis and that of the scattered wave $V_{diff}$ along the imaginary axis. The basic phase shift of the diffracted wave is $+\pi/2$ . (a) For positive phase contrast, an additional $+\pi/2$ phase shift is added to the diffracted wave, where the atom positions appear dark on a bright background. (b) For negative phase contrast, the corresponding additional phase shift is $-\pi/2$ , where the atom positions appear bright on dark (negative) background. . . . .	50
2.14	Plot of PCTF, which is the phase contrast transfer function and ACTF, which is the amplitude contrast transfer function vs spatial frequency ( $\alpha$ ). (a) A schematic plot of PCTF for an uncorrected microscopy, which is proportional to $-\sin 2\pi\chi(\alpha)$ . (b) Plot of PCTF for NCSI conditions in the aberration corrected microscopy, which is represented by a solid line. The dashed line shows the amplitude transfer function (ACTF vs $\cos 2\pi\chi(\alpha)$ ). . . . .	51
2.15	A schematic diagram of the essential elements of the electron-optical system for a) TEM and b) STEM are shown. . . . .	53
2.16	A schematic diagram showing the relative positions of multi-detectors. For BF imaging, semi-angle $\theta_1$ is estimated to be $< 10\text{mrad}$ , MAADF imaging $\theta_2$ is estimated to be $10\text{ mrad} < \theta_2 < 50\text{mrad}$ . . . . .	54
2.17	Plot showing the difference between the OTF and the PCTF for identical imaging conditions ( $V = 300\text{kV}$ , $C_S = 1\text{mm}$ , and $z = -40\text{nm}$ ). The OTF can be seen to extend to twice the spatial frequency ( $1/\text{\AA}$ ) of that corresponding to the aperture radius in CTEM. . . . .	56
2.18	A schematic diagram showing the signals produced when a direct beam of electrons interacts with a specimen. . . . .	57

2.19	A schematic diagram of a spectrometer that is attached after the viewing screen in the microscopy. . . . .	60
2.20	EELS showing different energy loss regions of the spectrum. A) a spectrum showing ZLP marked by an orange rectangle. The rest of the peaks are plasmons caused by multiple excitations; the plasmon peaks are rather high because the sample is very thick. B) a spectrum showing the core-loss region with the characteristic ionization edges labelled. . . . .	60
3.1	HAADF of the APB Cross structure in $\text{BiFeO}_3$ . a) One slice of cross structure image stack b) Combined multi-images after applying spatial drift correction. . . . .	66
3.2	The interface of the iMtools program. The “red” crosses indicate which peaks have been identified. The peak location list is shown in the top-right corner of the interface. . . . .	69
3.3	Shows the subtracted backgrounds for the whole elements. . . . .	78
3.4	The raw spectrum a) Before PCA was applied. b) After PCA was applied. . . . .	79
4.1	Atomic resolution images of similar antiphase boundaries in $\text{Bi}_{0.85}\text{Nd}_{0.15}\text{Fe}_{0.9}\text{Ti}_{0.1}\text{O}_3$ : a) HRTEM NCSI image, which shows all atom columns simultaneously, and b) HAADF/BF STEM overlay image, the red shows the HAADF contrast, which mainly shows the cations, whereas the the cyan shows the BF contrast, which principally shows the oxygen only columns. In both cases, atomic models of the boundary structure are overlaid to aid the reader, where purple is bismuth, red is iron, blue is titanium, and yellow is oxygen. . . . .	85

4.2	Quantitative comparisons of averaged cells for the charged antiphase boundaries (APBs) from HRTEM (negative $C_s$ imaging) and from HRSTEM (HAADF and BF combined). This figure shows the deviation of the oxygen atoms in the out-of-plane atomic position with respect to the references in both HRSTEM and HRTEM techniques. The error bars in the two cases were calculated from the standard deviation in the out-of-plane peak position measurement after averaging for the two cases. . . . .	87
4.3	Quantitative comparison of polarisation calculations in the z-direction as a function of distance from the APB boundary for both cases. The error bars in the two cases were calculated from the standard deviation in the out-of-plane peak position measurement after averaging for the two cases. . . . .	88
4.4	Atomic resolution images of antiphase boundaries in $\text{Bi}_{0.85}\text{Nd}_{0.15}\text{Fe}_{0.9}\text{Ti}_{0.1}\text{O}_3$ using HRTEM NCSI image, which shows all atom columns simultaneously. The yellow box shows the area that extracted for the simulation purposes. . . . .	89
4.5	Image simulation fitting in $\text{Bi}_{0.85}\text{Nd}_{0.15}\text{Fe}_{0.9}\text{Ti}_{0.1}\text{O}_3$ to an averaged image of perfect crystal close to the analysed region of the APB. The experimental and simulated images are on the same absolute intensity scale and agree in mean value, contrast, and have a pattern correlation of 0.98. The residual difference shown on the right has a contrast of 0.024 and contains predominantly image noise. . . . .	93

4.6	Shifting between apparent atom positions of BiFeO <sub>3</sub> structure in HRTEM images 300kV (NCSI) depending on object tilt. a) 3D visualisation where all atoms are labelled (Bi, FeO, O <sub>⊥</sub> and O <sub>∥</sub> columns). b) Image simulation from HRTEM (NCSI). c) and d) Represent apparent shifts of atom peak positions w.r.t their actual positions and the object tilts, where blue circles show fixed Bi atoms, triangles show apparent shifts of the peak positions, and where Red, green, brown and blue coloured lines represent O <sub>⊥</sub> , O <sub>∥</sub> , FeO, and Bi atoms, respectively. . . . .	95
4.7	Three parallel columns of point charges which represent the APB in xy-plane and referred as I <sub>1</sub> , I <sub>2</sub> , and I <sub>3</sub> , respectively. E and d represent the electric field the distance between columns. . . . .	98
4.8	3x3 parallel columns of point charges which represent the APB and referred as I <sub>1</sub> , I <sub>2</sub> , and I <sub>3</sub> , respectively. Each column, for simplicity, has three point charges with fixed distance (4Å) in x direction, while the separation between each columns of charges is 1nm in y direction. The white box refers to the specimen. The strength and the direction of the field are indicated by the color-wheel as well as by the length and the direction of the arrows. . . . .	99
4.9	A schematic diagram illustrating the method of images for calculating the electric fields close to a conductive surface. The correct field in the insulator (below the conductor) can be generated by adding a extra set of charges mirrored in the surface of the conductor (upper charges). These are mirrored in both position and sign of the charge.	101

4.10	Visualisation of the field distribution calculated by the method of images for 3x3 columns of point charges a) each column contains 3 point charges and the distance between the columns is 1nm, and b) each column contains 8 point charges and the distance between the columns is 2nm in order to see more clearly. The areas that indicated by white, black and red boxes are the specimen, conductor and the image charges, respectively. Obviously, in reality, only the field distribution in the specimen (i.e. inside the white box) exists. The field is represented using colours on a colour wheel and arrows, as in figure 4.8 where the arrows represent the direction of the field. .	102
4.11	Deviation between BiFeO <sub>3</sub> structure and HRSTEM image intensity peak positions depending on object tilt. a) 3D visualisation where all atoms are labelled(Bi, FeO, O <sub>⊥</sub> and O <sub>∥</sub> columns). b) and c) Image simulations from ADF and DF-HRSTEM 100kV, respectively. d) Represent apparent shifts of atom peak positions w.r.t their actual positions and the object thicknesses where Red, green, brown and blue coloured lines represent O <sub>⊥</sub> , O <sub>∥</sub> , FeO, and Bi atoms, respectively.	105
4.12	Apparent shifts of O columns in polarised BiFeO <sub>3</sub> structure as a function of sample thickness in HRSTEM. a) 3D visualisation of atoms in BiFeO <sub>3</sub> structure, red for Bi, brown for Fe, and blue for both O <sub>∥</sub> and O <sub>⊥</sub> columns. b) Deviation of O columns through the whole object thickness toward Bi columns. . . . .	107
4.13	Quantitative comparison of polarisation calculations before and after including the electron channelling effects in the z-direction as a function of distance from the APB boundary for both cases. The error bars in the two cases were calculated from the standard deviation in the out-of-plane peak position measurement after averaging for the two cases. . . . .	109

5.1	HAADF imaging of APB in BiFeO <sub>3</sub> . Images are represented on the false colour intensity scale shown below the images; the brighter atoms are the heavy A-site atoms (Bi/Nd), whereas the less bright atoms are the B-site atoms (Fe/Ti), oxygen atoms are not visible in this imaging mode. a) a field of view of $\sim 15\text{nm}$ at a pixel size of $\sim 0.15\text{\AA}$ to show the context of the APB cross within the ceramic; b) a higher magnification view of an area of $\sim 5\text{nm}$ at a pixel size of $\sim 0.5\text{\AA}$ showing the detailed structure of the APB cross. Two “L”-shaped structures are indicated. Steps and flat terraces are indicated by red and white boxes, respectively. . . . .	113
5.2	HAADF imaging of APB in BiFeO <sub>3</sub> using a) Simple align procedure b) Smart align procedure. Images are represented on the false colour intensity scale shown beside the images, the brighter atoms are the heavy A-site atoms (Bi/Nd), whereas the less bright atoms are the B-site atoms (Fe/Ti). The line profiles (shown in figure 5.2) of peak1 and peak2 are indicated by the red and yellow boxes, respectively. . .	114
5.3	Overlays of both Simple and Smart align procedures for a) A-site positions, and b) B-site positions. . . . .	115
5.4	A comparison of actual peak profiles with Gaussian fits for images processed using rigid registration and using ”Smart align”. (a) and (b) Peak profiles using both rigid registration (green), and Smart align (red) for a) Peak1, and b) Peak2. (c)-(f) The overlay of actual peak profiles (green for rigid registration and red for Smart align), and fits (blue), for c) Simple align procedure for peak1 d) Simple align procedure for peak2 e) Smart align procedure for peak1, and f) Smart align procedure for peak2. . . . .	116

5.5	The line profiles of peak1 with red boxed and peak2 with yellow boxed produced by using the Gaussian fit for a) Simple align, and b) Smart align. The Smart align (non-rigid registration) gives a slightly sharper image, although the difference is subtle. . . . .	117
5.6	A comparison of actual peak profiles with Gaussian fits for images processed using rigid registration and using (V1.9) "Smart align" after optimisation. (a) and (b) Peak profiles using both rigid registration (green), and Smart align (red) for a) Peak1, and b) Peak2. (c)-(f) The overlay of actual peak profiles (green for rigid registration and red for Smart align), and fits (blue), for c) Simple align procedure for peak1 d) Simple align procedure for peak2 e) Smart align procedure for peak1, and f) Smart align procedure for peak2. . . . .	118
5.7	Resulting images in which the fit images were subtracted from the experimental images for a) Simple align procedure b) Smart align (V1.9) procedure. White boxes show where the procedures are failed. While red boxes show the rest of the atom columns are same. . . . .	120
5.8	Elemental maps from EELS of the intercept of the boundaries (defects as a cross shape). (a)-(e) Chemical mapping of (APBs) showing the intercept of the boundaries: (a) Fe map, (b) simultaneously recorded HAADF image, which predominantly shows the Bi positions, (c) Ti map, (d) O map, (e) RGB mixed map with Red = Fe, Green = HAADF (Bi), and Blue = Ti. The "L" shaped arrangements of Fe atoms are marked in some maps. Square boxes indicate step regions. . . . .	123
5.9	The 3D structural model for the APB cross structure: a) the overall structure; b) magnified view of the core of the APB cross showing the two L-shaped arrangements of edge-sharing FeO <sub>6</sub> octahedra. Red circles indicate the off-center movement of atoms and directions shown by red arrows. . . . .	125

5.10	HAADF imaging of the APB cross structure shows the selected A, B, C, D regions for simulations. The purple colour indicates Bi (A-site) atoms, brown for Fe (B-site) atoms, and red for oxygen atoms. The integrated intensities that extracted from areas around the intensity peaks are indicated by yellow circles for Bi (A-site) columns and red circles for Fe-O columns. . . . .	129
5.11	Shows the changing intensity ratio of the selected regions with respect to the sample thicknesses. The thick horizontal gray lines show the range of values that estimated from the experimental image regions. Black, red, green, pink, and blue colored lines represent the B(Bi) parameters, 0.2, 0.4, 0.5, 0.7, and $1.0\text{\AA}^2$ , respectively. . . . .	130
5.12	Shows the comparison of the experiment vs. simulation images for the APB cross structure (the core) of HAADF imaging with respect to the four regions. In each box, the left image represents the experiment image and the right one represents the simulation image. The intensity increases from left i.e. in A and C regions) to the right (B and D regions). . . . .	131
5.13	Comparison for the core of the APB cross showing a good match to atom positions for all cation columns of a) Experimental image, and b) Simulation image. The colour scale runs from $0.06 I_0 - 0.36 I_0$ , where $I_0$ is the incident beam intensity. The two white boxes refer to, for example, a good agreement of contrast of atomic columns for both experimental and simulation images. . . . .	132
5.14	Two numerical solutions . . . . .	134
5.15	Two . . . . .	137

# List of Tables

2.1	Aberration coefficients and their corresponding conventional names [82]. . . . .	36
3.1	Steps for the STEM image simulation of a thick sample using the multiplies method [126]. . . . .	73
4.1	Shows the parameters that used in simulation for HRTEM imaging. .	92
4.2	Shows the parameters that used to visualise $2 \times 2$ BiFeO <sub>3</sub> unit cell. . .	93

# Acronyms

<b>AFM</b>	Antiferromagnetic.
<b>APBs</b>	Antiphase boundaries.
<b>A1</b>	Defocus 2-fold astigmatism.
<b>A-site</b>	Bismuth atoms.
<b>B-site</b>	Iron atoms.
<b>BFO</b>	Bismuth ferrite.
<b>B2</b>	Coma.
<b>C</b>	The Curie constant.
<b>CTF</b>	Contrast transfer function.
<b>CCD</b>	Charge Coupled Device.
<b>D</b>	the displacement effects.
<b>DFT</b>	Density function theory.
<b>DM</b>	Digital micrograph.
<b>EBSD</b>	Electron backscatter diffraction.
<b>E</b>	Electric field.
<b>ELNES</b>	Energy-loss near-edge structure.
<b>EXELFS</b>	extended energy-loss fine structure.
<b><math>E_C</math></b>	Coercive (electric) field.
<b><math>\epsilon</math></b>	The permittivity of the material.
<b><math>\epsilon_0</math></b>	The permittivity of vacuum.

<b>ED</b>	electron diffraction.
<b>EELS-SI</b>	Electron energy loss spectroscopy spectrum imaging.
<b>FM</b>	Ferromagnetic.
<b>FT</b>	Fourier transform.
<b>H</b>	External magnetic field.
<b>HAADF</b>	High angle annular dark field.
<b>H<sub>C</sub></b>	Coercive (magnetic) field.
<b>HRSTEM</b>	High resolution scanning transmission electron microscopy.
<b>HRTEM</b>	High resolution transmission electron microscopy.
<b>I</b>	Integrated intensity.
<b>k</b>	Coulomb constant.
<b>LCMO</b>	Lanthanum calcium manganite.
<b>LSMO</b>	Lanthanum strontium manganite.
<b>M</b>	Magnetisation.
<b>ME</b>	Magnetoelectric effect.
<b>MPB</b>	The morphotropic phase boundary.
<b>MRAMs</b>	Magnetic random access memories.
<b>MSA</b>	Multivariate Statistical Analysis.
<b>M<sub>S</sub></b>	Saturation magnetisation.
<b>MTF</b>	Modulation transfer function.
<b>NCSI</b>	Negative spherical aberration.
<b>O-site</b>	Oxygen atoms.
<b>OTF</b>	Optical transfer function.
<b>O<sub>2</sub>, O<sub>4</sub> etc..</b>	Octupoles.
<b>P</b>	Polarisation.
<b>PCA</b>	Principal component analysis.

<b>PE</b>	Paraelectric.
<b><math>P_S</math></b>	Saturation polarisation.
<b><math>q_i</math></b>	Born effective charge for the $i^{th}$ ion.
<b>Q1, Q3, etc..</b>	Quadrupoles.
<b><math>r_A</math></b>	The radii of A-site.
<b><math>r_B</math></b>	The radii of B-site.
<b>RE</b>	Rare-earth.
<b><math>r_O</math></b>	The radii of O-site.
<b>SDSD</b>	The Statistically Determined Spatial Drift.
<b>SI</b>	Spectrum imaging.
<b>STEM</b>	Scanning transmission electron microscopy.
<b>S3</b>	Star aberration.
<b>t</b>	The tolerance factor.
<b>TDS</b>	Thermal diffuse scattering.
<b><math>T_C</math></b>	Curie point or temperature.
<b>TEM</b>	Transmission electron microscopy.
<b><math>\vec{u}_i</math></b>	Ion displacement.
<b>V1.8</b>	Version 1.8.
<b>XRD</b>	X-ray powder diffraction.
<b>WPO</b>	Weak phase object.
<b>ZLP</b>	Zero-loss peak.
<b><math>Z_{Bi}</math></b>	Born effective charge for bismuth.
<b><math>Z_{Fe}</math></b>	Born effective charge for iron.
<b><math>Z_{O\parallel}</math></b>	Born effective charge for oxygen ions parallel respectively to the electric polarisation.

$Z_{O\perp}$	Born effective charge for oxygen ions perpendicular respectively to the electric polarisation.
$\chi$	The susceptibility behavior of a magnetic material.
<b>2D</b>	Two dimensional.
<b>3D</b>	Three dimensional.
$\sigma$	Charge density.
$\sigma$	Charge density.

# Abstract

Since bismuth ferrite-based perovskites display magnetic ordering as well as ferroelectric behaviour, they have been widely researched due to the possibility to fabricate multiferroic devices. This thesis is focused on investigating structures formed in bismuth ferrite (BFO) as a consequence of Ti doping using atomic resolution transmission electron microscopy (TEM). This is performed both using the negative spherical aberration (NCSI) imaging technique in TEM and scanning transmission electron microscopy (STEM) with simultaneous dark and bright field imaging.

A quantitative study was made of the difference between high resolution TEM (HRTEM) and high resolution STEM (HRSTEM) for quantitative polarisation mapping around antiphase boundaries (APBs) is observed and reported. Although similar trends in the structures are found in the two techniques, quantitative differences are noted. For HRTEM, using NCSI gives 60% lower polarisation values in comparison to HRSTEM in the case studied here. It is shown that the sample tilt has no influence on the polarisation measurements in this case as the direction of the sample tilt in our case is perpendicular to the direction of polarisation. It is shown that the ultra-thin sample used in HRTEM had a reduced polarisation due to the effects of surfaces, but that also the polarisation was underestimated from the images due to one oxygen column appearing in the images at a position slightly displaced from its real position due to the effects of electron channeling in the material. For

the case of HRSTEM, it was found that the polarisation was overestimated due to a similar effect, where an oxygen atom image is slightly displaced from the column position in the opposite direction at this specific sample thickness. Thus, it is clear that the use of simulations is essential to any atomic resolution quantification of polarisation by either technique.

In addition to this, , the structure and chemistry of the crosses and corners on APBs were determined using a combination of high angle annular dark field (HAADF) combined with electron energy loss spectroscopy spectrum imaging (EELS-SI) in STEM. The 3D structures of the APB cross structure were fully determined and these were verified by multislice frozen phonon image simulations. It was suggested on the basis of the structure of some of the edge-sharing octahedral structural units in this cross that they would support a permanent magnetic ordering, since their structure was similar to that of maghemite. In analysing this structure, the advantages of non-rigid registration (alignment of a sequence of short exposure images as well as removing local distortions in each image prior to summation) for removing line noise distortions from STEM images are investigated quantitatively. Two APB corners were also investigated using NCSI HRTEM and HRSTEM. Whilst some details of each structure were impossible to determine unambiguously, most parts of these APB corners have structural units similar to those in steps and in the APB cross. It should also be noted that the two APB corners show some detailed differences in structure suggesting that there is a range of possible structures on such antiphase boundaries, but all constructed from a limited number of structural units.

# Chapter 1

## Introduction

A material that displays a combination of, at least, two single ferroic properties simultaneously is described as a multiferroic substance (see section 1.1). Huge attention has been paid to these (multiferroics) materials, not only for their significant applications such as magnetoelectric devices, which can be displayed both electrically and magnetically [1]. Over the past two decades, the possibility of creating feasible room temperature multiferroic devices has generated considerable interest in bismuth ferrite [1, 2]. One of the fascinating aspects of bismuth ferrite (BFO) is the coexistence between ferroelectric and magnetization orders. This coupling is known as the magnetoelectric effect (ME), where the ferroelectric behaviour can be controlled by a magnetic field and vice versa. This could be used for the improvement of new devices in various aspects. BFO, therefore, is a potential candidate for creating non-volatile information storage devices including magnetic random access memories (MRAMs), ferroelectric random access memories [3, 4], and spintronic applications such as spin-valve structures wherein the spins can be manipulated by an electric field [5, 6]. But not all multiferroics display strong, efficient ME effects that could be a feasible candidate or fit for these applications. This is because, as some researchers [7, 8] have shown that most of them could be anti-ferromagnetic or weak

ferromagnetic materials, where they display enough high and low Néel temperatures that limit their uses in such applications. Concerning the weak ferromagnet materials, this could be originated from either anisotropic super exchange interactions (these materials roughly record high Néel temperature degrees) or from single spin anisotropy energy (these kinds of materials normally display low Néel temperature scales) [7]. Concerning the  $\text{BiFeO}_3$ -based perovskite structure, BFO has a Curie temperature (temperature at which material switches from ferroelectric to paraelectric) of  $830^\circ\text{C}$  and a Néel temperature (temperature at which material switches from paramagnetic to antiferromagnetic) of  $370^\circ\text{C}$  [1] in which both are within the range that device designers prefer. Since large numbers of ferroelectric materials have a structure similar to the mineral perovskite ( $\text{BaTiO}_3$ ), they have the general perovskite formula  $\text{ABO}_3$  and the prototype structure is cubic with space group  $R3c$ . The ideal perovskite structure with a cubic unit cell consists of a cation on cell corners (the A-site) and a different cation, commonly a transition metal, on body centres (the B-site cation), which is coordinated by six O atoms (on face centres) in an octahedron as shown in figure 1.1. The perovskite-structure also can be viewed as a three dimensional (3D) network of corner shared  $\text{BO}_6$  octahedra and the A-site coordinated by 12O atoms as shown in figure 1.2

Regarding the source of the ferroelectricity, it is not quite the same as that of the antiferromagnetism. The source of the ferroelectricity is due to a structural distortion caused by the lone pair of ( $6s$ ) of the A-site (Bi). The lone  $6s$  pair distorts the charge cloud and sits to one side. So, the nucleus is off centre with respect to the outer valence electrons, and thus the atomic core will prefer to sit off-centre in any atomic site. This off-centre ordering is easy to order via electrostatic effects giving spontaneous polarisation. From this perspective, we may have the possibility to control the ferroelectricity and magnetism behaviour independently by substituting A and/or B-site atoms. However, one big issue with this material

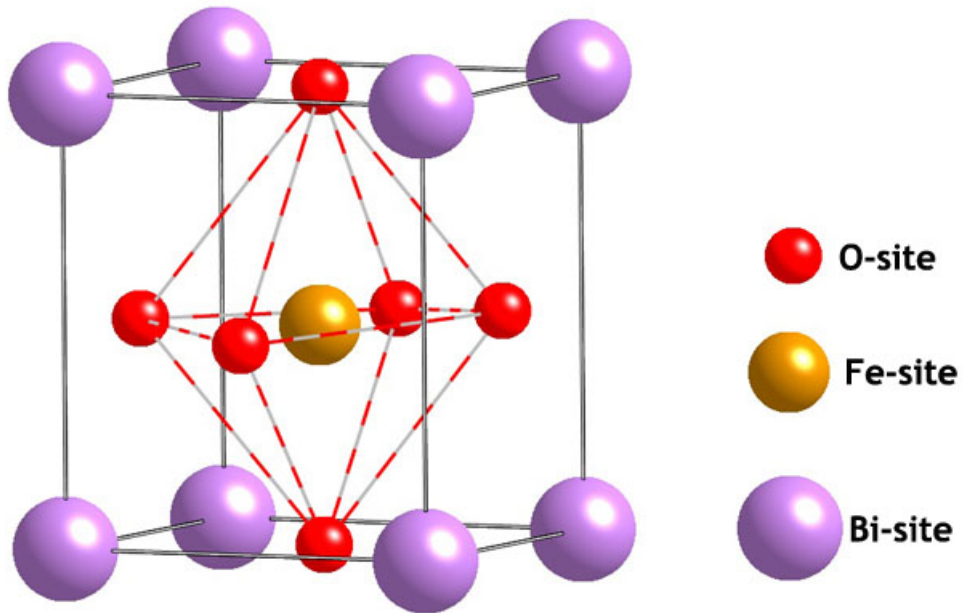


Figure 1.1: The unit cell of a simple cubic perovskite, with the composition  $ABO_3$ , where red is used for O atoms, magenta for A-sites, and orange-yellow for B-sites.

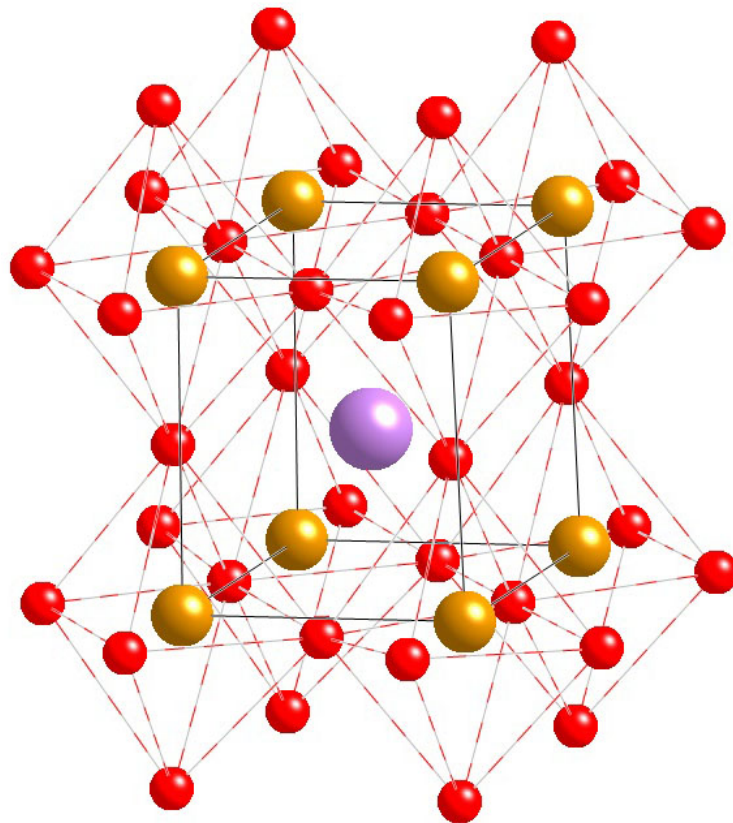


Figure 1.2: A 3D corner shared network of  $FeO_6$  octahedra, red is used for O atoms, magenta for A-sites, and orange-yellow for B-sites.

is its high electrical conductivity due to the O vacancy hopping, which limits their applications [9]. Recently, however, the aforementioned problem has been solved by a process of doping, where BFO is co-doped by a certain amount of Nd and Ti [10]. The main aim of this thesis is an intensified analysis of BFO-based ceramic co-doped with both Nd and Ti. The results will be discussed in more details in chapters 4, and 5. It is organized as follows: The first chapter contains the definition of multiferroics, ferroelectrics, ferromagnetism, as well as the basic physical knowledge of BFO-based ceramics and the current stage of BFO are discussed. In chapter 2, a general review both of transmission electron microscopy (TEM) and scanning transmission electron microscopy (STEM) are presented. In chapter 3, data analysis is described as used in chapters 4 and 5. Chapter 4 focuses mainly on the differences between high resolution transmission electron microscopy (HRTEM) and scanning transmission electron microscopy (HRSTEM) for the analysis of polar ordering in BFO samples with different thicknesses. Then, the expected causes behind the results are modeled and visualized in order to interpret them sensibly. In chapter 5, novel junction of antiphase boundaries in BFO are investigated at atomic resolution together with elemental maps. Final chapter (6) contains the summarized conclusions and future work is recommended.

In the following sections we will begin with the concept of multiferroics. As both ferroelectricity and ferromagnetism are physical properties of BFO, they will be discussed. The general properties of BFO are also discussed, as well as the motivation of the current research on BFO-based ceramic co-doped with Nd and Ti.

## 1.1 Multiferroics concept

Multiferroics, which is a term defined by H. Schmid [11], refers to materials in which there is a coupling between the different types of ferroic ordering

such as ferroelectricity, ferromagnetism, ferroelasticity and ferrotoroidicity. Since the two orders are simultaneously presented, by changing the direction or even the magnitude of an applied field, may affect more than one of the ferroic orders presentation. For example, switching the magnetization direction in multiferroic materials by applying enough magnetic field may change polarisation and vice versa, as shown in figure 1.3. These coupled effects, which only occur in simultaneously ferromagnetic and ferroelectric materials, are known as magnetoelectric (ME) effects. They are, therefore, those specific materials, which exhibit magnetism and ferroelectricity properties simultaneously within one phase, that are planned to be exploited to generate new multifunctional devices.

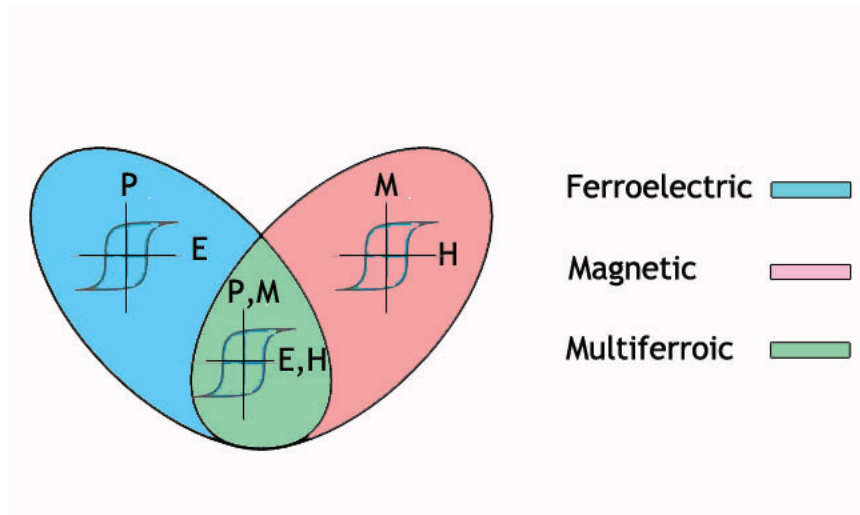


Figure 1.3: A schematic diagram showing Multiferroic materials that combine the ferroelectric and magnetism properties. Ideally, the magnetization of a ferromagnet in a magnetic field displays the usual hysteresis loop (pink), and ferroelectrics have a similar response to an electric field (blue). The multiferroics can be created that are simultaneously ferromagnetic and ferroelectric (green), which is a magnetic response to an electric field, or, vice versa.

[12]

## 1.2 Ferroelectric state

### 1.2.1 Curie-temperature and phase transitions dependent in ferroelectrics

Ferroelectric materials show a spontaneous electrical polarisation (the atomic dipole moments) in a particular direction even in the absence of an external field. This spontaneous direction can be switched by an external electric field. These materials experience a phase transition at specific temperature called the Curie point ( $T_C$ ) from a ferroelectric phase to a paraelectric phase, and vice versa. That is, the ferroelectric state exists when  $T < T_C$  while  $T > T_C$  the material is paraelectric. The behavior of the dielectric constant above the Curie point can be described by the Curie-Weiss relation as:

$$\epsilon = \epsilon_o + \frac{C}{T - T_C} \quad (1.1)$$

where  $\epsilon$ ,  $\epsilon_o$ ,  $C$ , and  $T_C$  are the permittivity of the material, the permittivity of vacuum, the Curie constant and the Curie temperature, respectively. One well known structure that undergoes several phase transitions is barium titanate ( $\text{BaTiO}_3$ ) as shown in figure 1.4, which has been adapted from [13]. For decades,  $\text{BaTiO}_3$ , which is a ferroelectric material, has been widely utilised in device applications [14, 15].  $\text{BaTiO}_3$  like  $\text{PbTiO}_3$  is well known for having strong strain effects reported in tetragonal ferroelectrics [5, 16]. Zhan *et al.* [17] have reported that the polarization for  $\text{BaTiO}_3$  is about  $15\mu\text{C}/\text{cm}^2$ . It is noteworthy that this value is much lower than the one for single-crystal  $\text{BaTiO}_3$  of about  $26\mu\text{C}/\text{cm}^2$  [18]. This polarisation manifests without an applied field and is hence known as spontaneous polarisation. In the ideal case, the system is ideal perovskite structure with a cubic unit cell. However, when the system is further cooled down and undergone phase change leads

to ferroelectric behaviour, the resulting tetragonal structure with an accompanying movement of the Ti atoms inside the  $O_6$  that elongated in  $c$ -axis with  $a \neq c$ . Upon further cooling, a further phase transition occurs to a ferroelectric orthorhombic structure with  $a \neq b \neq c$ . Upon cooling the system further, the result is a ferroelectric structure with  $\alpha \neq \beta \neq \gamma$ .

Polarisation in perovskites is usually calculated with the aid of Born-effective charges (which differ from formal ionic charges that would apply to isolated ions), where the movement of each atom is considered in terms of its effects on the whole lattice [19]. Therefore, the polarisation can be calculated from the movements of the atoms with respect to the ideal atomic position, given as [20]:

$$\vec{P} = \sum q_i \vec{u}_i \quad (1.2)$$

where  $q_i$  refers to the Born effective charge for the  $i$ -th ion and  $\vec{u}_i$  is its displacement with respect to the ideal atomic position in an unpolarised structure.

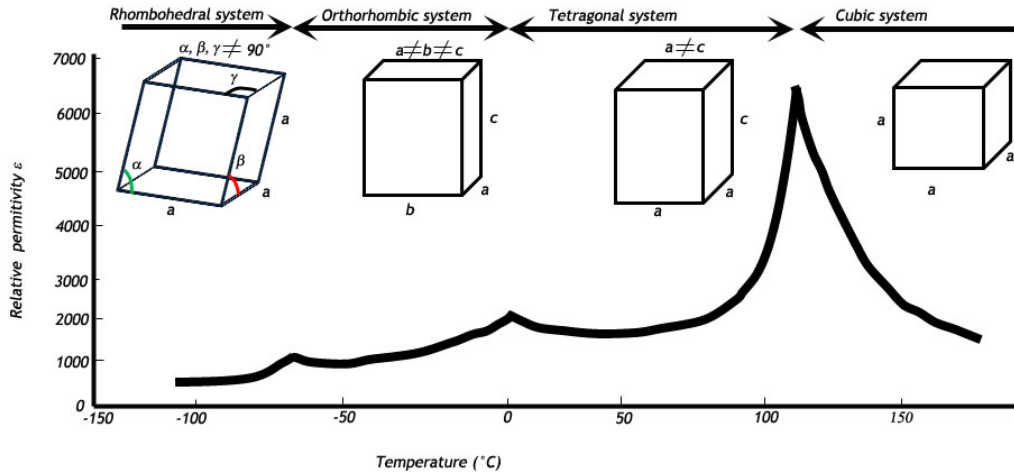


Figure 1.4: A schematic diagram of relative permittivity of  $BaTiO_3$  changes with the temperature displaying various phase transitions. When the ideal cubic system is cooled, the resulting structures are tetragonal, orthorhombic, and rhombohedral systems, respectively.

## 1.2.2 Domain formation in Ferroelectric structures

Spontaneous polarisation in ferroelectrics results in to a state where all electric dipoles are uniformly aligned in a certain region even without an applied field. The alignment direction will be a specific crystal direction (for instance [001] in a tetragonal ferroelectric). These electric polarisations are oriented uniformly in regions called domains. However, to minimise both stray electric fields at the sample edges, and anisotropic strain of the sample from the shape change of the cell on changing from a paraelectric to a ferroelectric state, domains are formed with different orientations of the polarisation axis [21]. For example,  $90^\circ$  domains are commonly formed in tetragonal ferroelectrics as shown in figure 1.5. The microscopic electric dipoles in neighboring domains are aligned in different directions. The interface between two domains is known as a domain wall. If an external field is applied, the favorably oriented domains grow while others shrink and thus the domain walls move, allowing polarisation to be reoriented in response to field. This process also converts some electrical energy into heat. Co-operative domain movement is needed to align the polarisation of the sample to the applied field until it reaches saturation when all domains are as favourably aligned to the field as possible. By reversing the applied field, the domain wall can be moved reversibly, but the polarisation cannot be removed entirely. The field that is needed to diminish the total polarisation of the entire material to zero is known as the coercive field. With continual decrease in the external field in the negative direction, the electric dipoles in the material will again become saturated but in the opposite direction. This interesting characteristic of the ferroelectric materials is known as domain switching, whereby the polarisation state can be switched by applying enough external field.

As mentioned above, ferroelectrics possess a spontaneous alignment of atomic dipole moments even with no applied electric field ( $\mathbf{E}=0$ ). The direction of

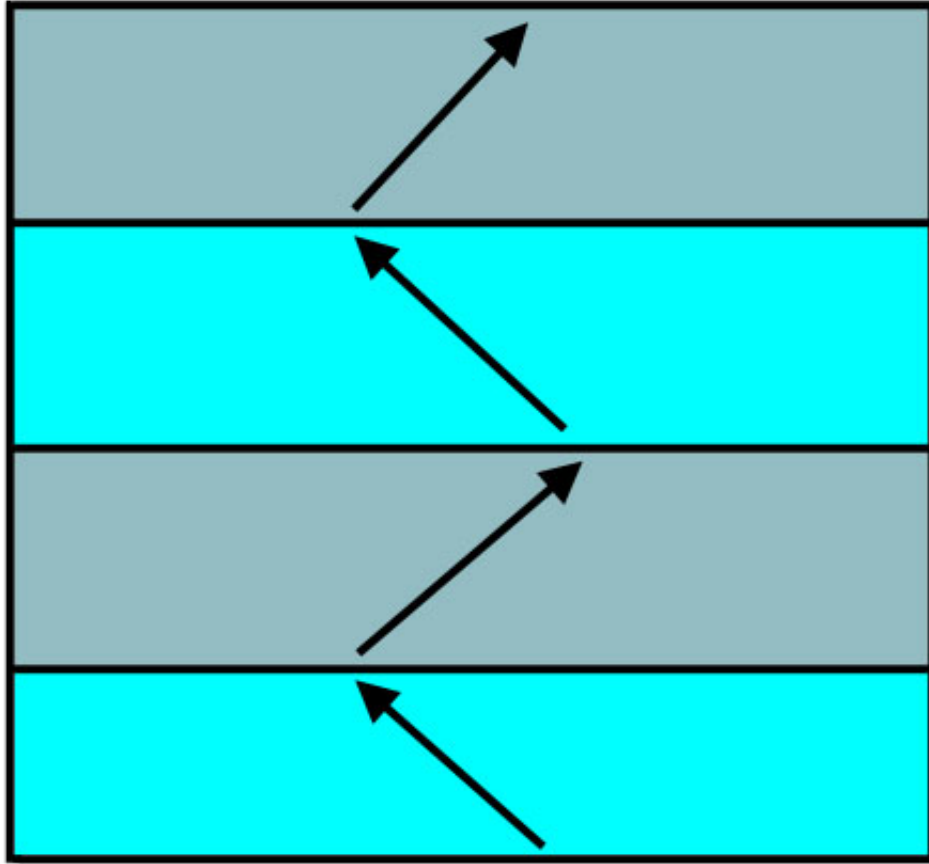


Figure 1.5: A schematic diagram of  $90^\circ$  domain structures, as seen in simple tetragonal ferroelectrics like  $\text{BaTiO}_3$  and Ti-rich  $\text{Pb}(\text{Zr},\text{Ti})\text{O}_3$ . Spontaneous polarisation directions of the domains are shown by arrows.

the permanent atomic dipole moments can be reversed by an applied electric field (figure 1.5) but the polarisation shows a hysteretic behaviour as shown in figure 1.6. At first, the polarisation increases linearly when the amount of the electric field is small, where (+) means the positive direction of the polarisation axis. As the applied field is increased, the dipoles orient towards the same direction of the applied field. When dipoles align completely to the same direction of the applied field, they show no further change. This state is referred to as saturated state ( $P_S$ ). By decreasing the applied field, the polarisation does not hit zero value. However,

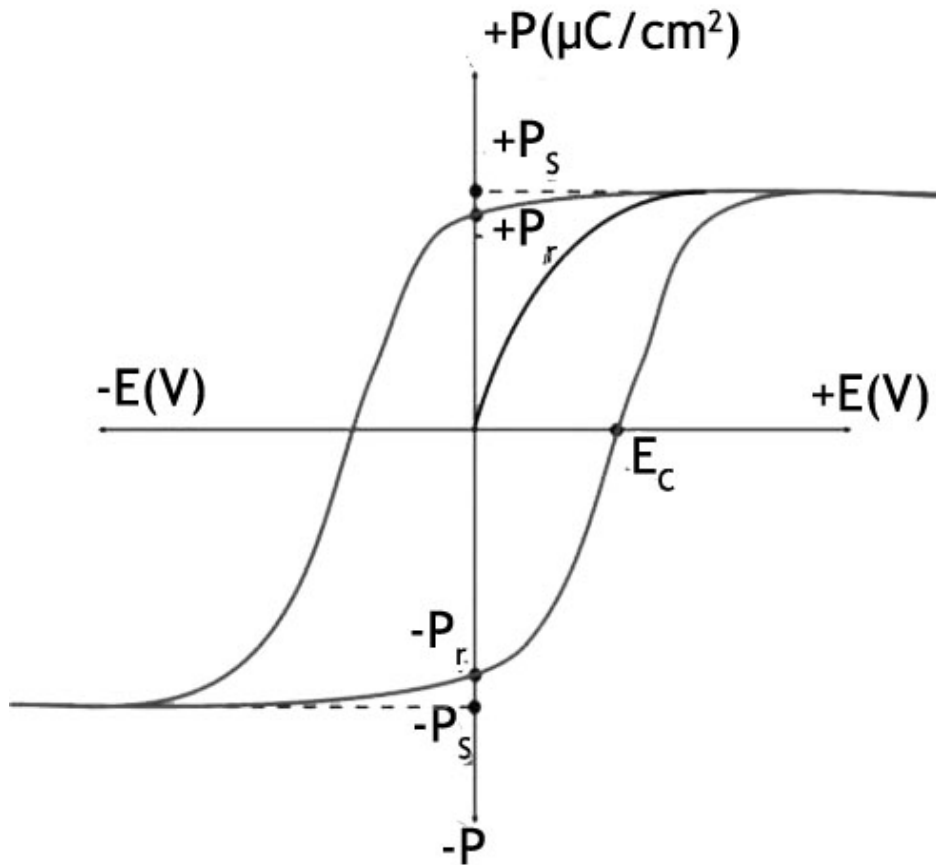


Figure 1.6: A schematic diagram of ferroelectric hysteresis loop (Polarisation (P) *vs.* Electric field (E)).[22]

if the applied field records zero value, a noticeable amount of the dipoles keep their positive direction and display a remnant polarisation. The appropriate field needed to degrade the polarisation to attain its minimum value ( $P=0$ ) is called the coercive field ( $E_C$ ). If the applied field is decreased more, the direction of the polarisation will be flipped to the opposite direction and hence the same behaviour can be observed.

### 1.2.3 Ferroelectricity in perovskite structures

The ferroelectric material system considered in this work is bismuth ferrite (BFO), which has a perovskite crystal structure. The perovskite structure and physical properties of BFO will be described in the following section.

#### 1.2.3.1 BiFeO<sub>3</sub> basic structure (Perovskite)

It has mentioned in the introduction, at high temperature BFO-based structure is cubic paraelectric while at low temperature is rhombohedral ferroelectric structure with  $R3c$  symmetry. It is the A site, atomic movement relative to the ideal position, in BiFeO<sub>3</sub> system, which brings about all the structural variations mentioned above [23], as shown in figure 1.7. The polarisation again can be calculated from equation 1.2 considering A-site atomic positions fixed and hence calculating any significant shifts of the rest of the atom columns with respect to the fixed A site columns. This is done by utilising the Born effective charges as mentioned in section 1.2.1. The Born effective charges covered for  $Z_{Bi}$ ,  $Z_{Fe}$ ,  $Z_{O\parallel}$ , and  $Z_{O\perp}$ .  $Z_{O\parallel}$  and  $Z_{O\perp}$  refer to the O ions (see section 4.2.2), which are parallel and perpendicular, respectively to the electric polarisation as shown in figure 4.15 [24].

One of the features of the perovskite structures is to that its precise symmetry can be tuned depending on the atoms on the A and B sites. The distortion from cubic depends on the size of the A and B site atoms in the perovskite through the Goldschmidt tolerance factor:

$$t = \frac{r_A + r_O}{\sqrt{2}(r_B + r_O)} \quad (1.3)$$

where  $r_A$ ,  $r_B$ ,  $r_O$  are the radii of A-site, B-site and O-site, respectively [26]. The ideal cubic perovskite should have  $t=1$  (which is just a result from simple geometry).

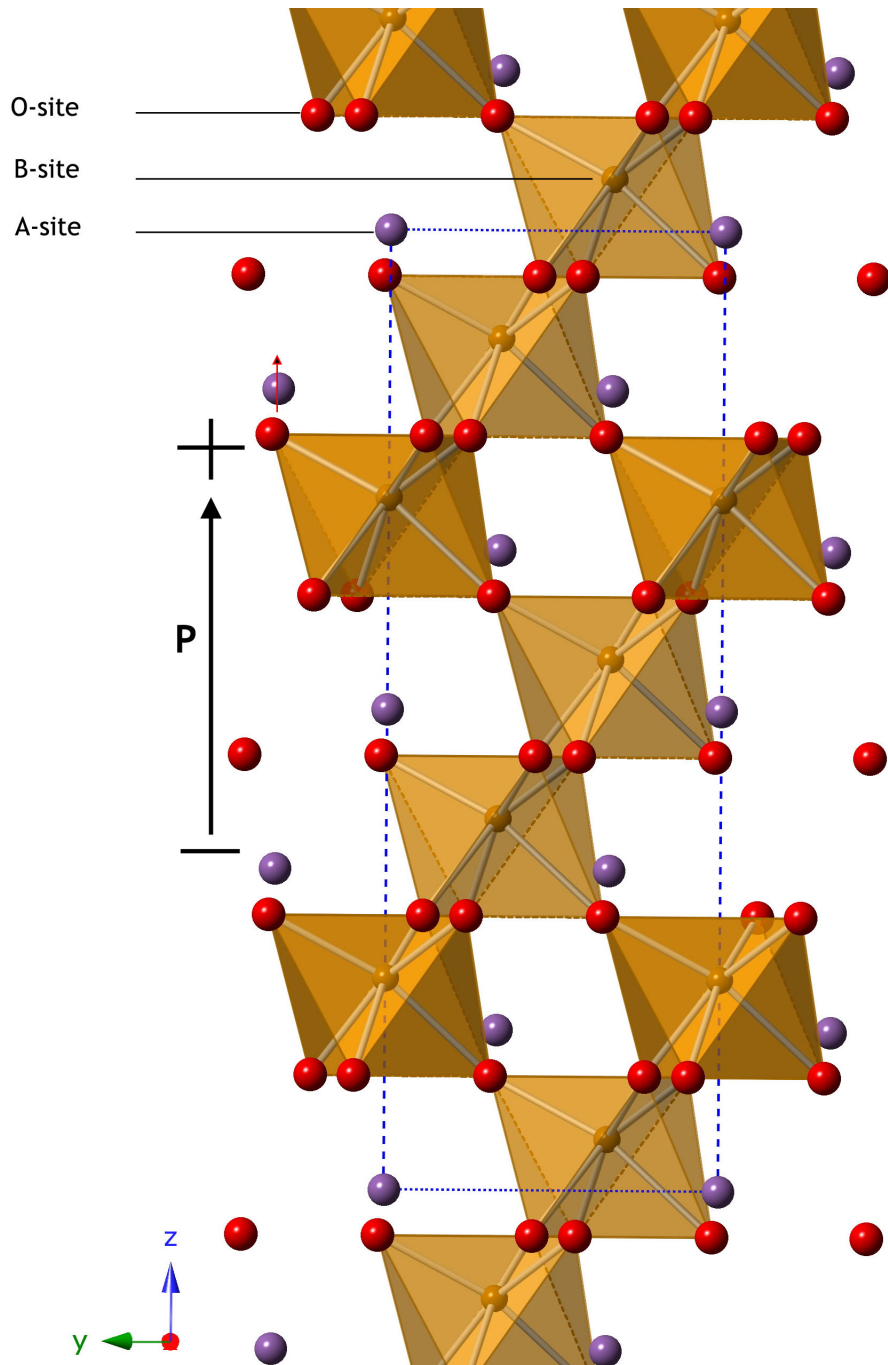


Figure 1.7: A schematic drawing of the  $\text{BiFeO}_3$  crystal structure where the direction of the ferroelectric polarisation by an arrow is shown in the figure [25]. The motion of the A-site is shown by red arrow. Red is used for O atoms, magenta for A-sites, and orange-yellow for B-sites.

The stability of different variants of the perovskite structure is directly related to the tolerance factor which lies between  $t=0.75$  and  $t=1.05$  for most perovskites. For very small tolerance factors the A-site atom is too small or the B-site atom is too large to allow the perovskite structure to form. Moreover, the perovskite

structure stability is affected by the ratios between ionic radii  $r_A/r_B$ , and  $r_B/r_0$  too [26]. In this case, when the  $t(\text{BiFeO}_3)=0.96$ , the transition has modified from polar to antipolar behaviour resulting in the stabilisation of a rhombohedral ferroelectric structure [27]. Substituting something else smaller than Bi onto the A site reduces the average A-site radius and thus reduces  $t$ . This is shown in the following section.

### 1.2.3.2 Antiferroelectricity and antiferroelectric structures.

In contrast to the description above, not all off-centre atomic displacements lead to ferroelectricity in the perovskite structures. For example, the lead zirconate structure ( $\text{PbZrO}_3$  commonly denoted as PZ) distorts from a centrosymmetric cubic structure at high temperature to an orthorhombic structure at room temperature, which is antiferroelectric when PZ is cooled below the Curie temperature this is shown in figure 1.8. As stated above, similar transition happens for  $\text{BiFeO}_3$  when the A-site lattice is substituted with various rare-earth ( $\text{RE}^{3+}$ ) elements [27, 28, 20]. These  $\text{RE}^{3+}$  dopants are smaller than  $\text{Bi}^{3+}$  but isovalent, which reduces the tolerance factor,  $t$ , and promotes the AFE transition. The transition to an AFE phase occurs in the range at  $15\% \leq \text{RE} \leq 25\%$  for Nd [27, 10], and for Sm at  $x = 14\%$  [29]. The resulting AFE phase is similar in structure to  $\text{PbZrO}_3$ , but the  $c$ -axis is  $4 a_p$  for RE doped  $\text{BiFeO}_3$  rather than  $2 a_p$  in  $\text{PbZrO}_3$ . The reason for this extra large  $c$ -axis is hitherto unclear.

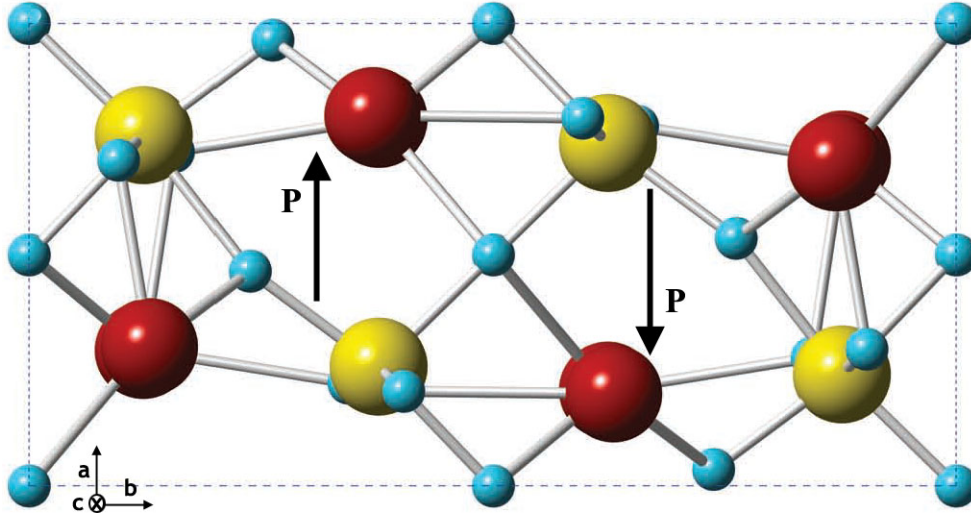


Figure 1.8: A schematic diagram of the perovskite unit cell of  $\text{PbZrO}_3$  which displays the behaviour of the crystal distortion due to the shifting Pb ions, Pb ions are marked in red, Zr ions in yellow, and O ions in cyan. The unit cell splits into two halves with Pb ions shifted in opposite directions resulted in formation of the polarisation trends that denoted by arrows up and down in each half of the cell [30].

### 1.3 Ferromagnetism

Ferromagnets (ferromagnetic materials) display a well oriented magnetic-dipole moment even when no external magnetic field ( $\mathbf{H}$ ) is presented. In contrast antiferromagnets have zero magnetic moment due to an anti-parallel alignment of their magnetic dipole moments. A ferromagnetic undergoes a phase transition at temperature called Curie temperature  $T_C$ . Above the Curie Temperature the paramagnetic phase has no net magnetic moment and as temperature goes below the former the ferromagnetic phase is incurred with spontaneous magnetic polarisation. The susceptibility behavior,  $\chi$ , of a magnetic material is governed by the Curie-Weiss law:

$$\chi = \frac{C}{T - T_C} \quad (1.4)$$

Magnetic materials can display several types of magnetic ordering such as

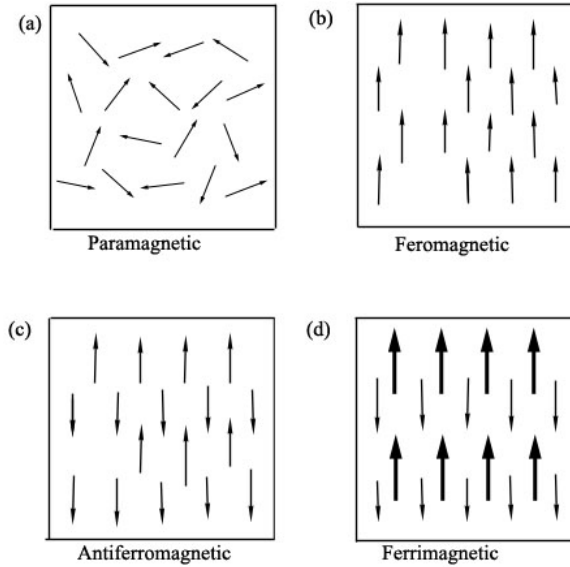


Figure 1.9: Ordering possibility of the magnetic dipoles in the magnetic materials:(a) Paramagnetic; (b) Ferromagnetic; (c) Antiferromagnetic; (d) Ferrimagnetic.[8]

paramagnetic, (anti) ferromagnetic, and ferromagnetic ordering as shown in figure 1.9. Ferromagnetism prevails when all the magnetic dipoles line up in the same direction, while antiferromagnetic appears when the dipoles align anti-parallel. Paramagnetism corresponds to the fact when there is no net dipole moments due to random alignment. Ferrimagnetics show the similar tendency as in antiferromagnetics but with some dipoles moments in one direction being smaller than the others in opposite direction.

### 1.3.1 Hysteresis in magnets

Similar to the ferroelectric hysteresis-loop in figure 1.6, ferromagnetic material has the spontaneous magnetization without applied magnetic field ( $\mathbf{H}=0$ ). When the magnetic field is applied, the majority of dipole moments align to the direction of the applied field, resulting in a net magnetization ( $\mathbf{M}$ ). Keep increasing the applied field, the magnetization will reach the saturation ( $\mathbf{M}_s$ ) stage where the saturation value remains unchanged. If the field is then reduced to zero there exists some dipoles which keep their alignment and therefore material possesses magne-

tization known as remnant magnetization. The magnetic applied field required to reduce the magnetization to its minimum value ( $\mathbf{M}=0$ ) is called the coercive field ( $\mathbf{H}_C$ ). Keep reducing the applied field, which is increasing in the negative direction, the magnetization direction will be reversed and hence the reversible magnetization occurs as shown previously in ferroelectric hysteresis loop in section 1.2.2.

### 1.3.2 Magnetic ordering in perovskites

The fundamental thought that crystal structures could simultaneously be ferromagnetic and ferroelectric was first proposed by Pierre Curie in the nineteenth century [31]. Curie considered that Ni could be exploited to discover the magnetoelectric properties, but this did not work and has now shown to be impossible. Later, chromium(III) oxide ( $\text{Cr}_2\text{O}_3$ ) attracted great interest and was found to have paraelectric (PE) and antiferromagnetic (AFM) behaviour, a combination that makes microelectronics applications impractical [1]. Boracites had also been studied for quite a number of years but only show magnetoelectricity at low temperatures [32]. The manganese oxides of general formula  $\text{RE}_{1-x}\text{M}_x\text{MnO}_3$  (RE, and  $\text{M} = \text{Ca}, \text{Sr}, \text{and Ba}$ ), similar to the cubic perovskite structures, have astounding structural, magnetic and transport properties impelled by the interfere valence  $\text{Mn}^{3+}$  and  $\text{Mn}^{4+}$ . Lanthanum calcium manganite  $(\text{La}, \text{Ca})\text{MnO}_3$  (LCMO) and lanthanum strontium manganite  $(\text{La}, \text{Sr})\text{MnO}_3$  (LSMO) are some of the most studied ferromagnetic perovskites [33, 34, 35, 36, 37, 38]. LCMO is an antiferromagnetic (AF) insulator at low and high  $x$  values while with  $x \approx \frac{1}{3}$  it is a metallic ferromagnetic (FM) [36, 37]. On the other hand, lanthanum strontium manganite  $(\text{La}, \text{Sr})\text{MnO}_3$  displays a ferromagnetic (FM) behaviour with a range of different structures such as monoclinic or orthorhombic/rhombohedral [38].

It was BFO which provided a break through and was considered an auspicious candidate for device applications. The magnetic spin configuration in BFO

was confirmed to be a G-type antiferromagnetic in which each the  $\text{Fe}^{3+}$  ions situated in the  $[111]_{\text{pc}}$  direction is surrounded by anti-parallel magnetic moments of  $\text{Fe}^{3+}$  ions with the  $(001)_{\text{hex}}$  plane as shown in figure 1.10. Nevertheless, this magnetic structure was modified to cover the long-range cycloidal spiral in the  $[110]_{\text{hex}}$  with a long wavelength period of 62nm within a  $(110)$  spin rotation plane in the hexagonal setting of the system [39, 40]. Doping to A- and B-site as a solution to the problem could not become a success but yet BFO is still considered a structure that is suitable for magnetoelectric devices. This is because pure BFO displays ferroelectric [41] and antiferromagnetic [42]) behaviour simultaneously at room temperature. Chemical modifications of BFO structure have continuously been exploited to get fruitful results and this will be discussed in section 1.4.

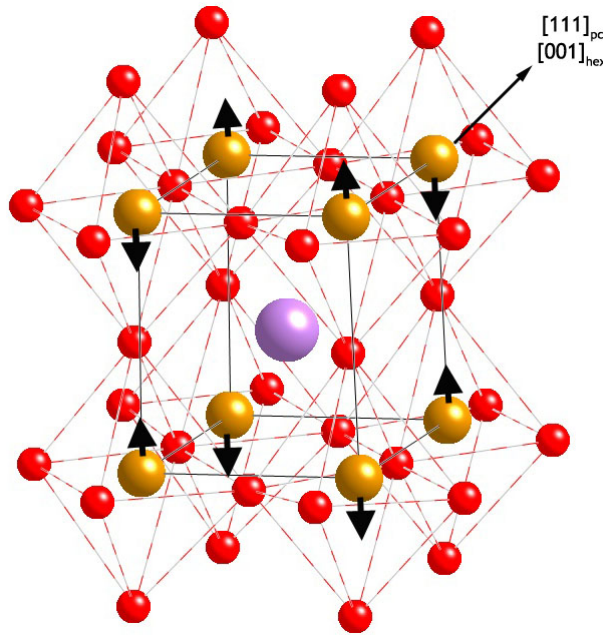


Figure 1.10: A schematic diagram of G-type AFM structure where the direction of the magnetic orderings is shown by arrows. The polarisation axis of Fe (B-site) cations is along  $[111]_{\text{pc}}$  and  $[110]_{\text{hex}}$  directions. Red is used for O atoms, magenta for A-sites, and orange-yellow for B-sites.

### 1.3.3 Magnetoelectric coupling

Coupling between the two phases (ferroelectricity and ferromagnetism) however may not always lead to exhibit ME effects [43]. Sometimes the ME coupling is too weak to be exploited for applications [8]. Unluckily, there are few magnetoelectric multiferroics that exhibit strong ME effects at room temperature. This happens because ferroelectricity requires unfilled  $d$ -shell to permit hopping of electrons from the oxygen  $2p$ -shell, which is supposed to be filled [44]. In contrast, ferromagnetism requires a partially filled  $d$ -shell in order to display the magnetic ordering [44]. As a result, the coupling between two the phases ends up being completely incompatible [45, 46]. Unlike the ferroelectricity source in BFO structure as mentioned in the introduction [47], the weak-ferromagnetism arises from the asymmetric super-exchange including spin-orbital coupling between two adjacent (B-site) cations through the non-magnetic anions such as oxygen (Fe —O —Fe) [7]. Therefore, much effort has been done in order to enhance the coupling between those orderings by modifying the (A-site) Bi or (B-site) Fe atoms of BFO. This includes substitution of A and B- sites with various transition metals [44, 48, 49, 7, 50].

Mathematically, it has been demonstrated that ME effects can be evaluated through expansion of free energy, in a given direction  $i$ , in terms of polarisation ( $P_i^S$ ) [51].

$$P_i(\vec{E}, \vec{H}) = \frac{\partial F}{\partial E_i} = P_i^S + \varepsilon_o \varepsilon_{ij} E_j + \alpha_{ij} H_j + \frac{1}{2} \beta_{ijk} H_j H_k + \gamma_{ijk} H_i E_j - \dots \quad (1.5)$$

and the spontaneous magnetization ( $M_i^S$ ) in the direction (i) can be as:

$$M_i(\vec{E}, \vec{H}) = \frac{\partial F}{\partial H_i} = M_i^S + \mu_o \mu_{ij} H_j + \alpha_{ij} E_i + \beta_{ijk} E_i H_j + \frac{1}{2} \gamma_{ijk} E_j E_k - \dots \quad (1.6)$$

where  $\vec{E}$ , and  $\vec{H}$ ,  $\epsilon$ ,  $\mu$  are the electric field, magnetic field, the electric and magnetic susceptibilities, respectively. The polarisation induction by a magnetic field or the magnetization by an electric field for the linear ME effect identified by tensor  $\hat{\alpha}$ , while  $\hat{\beta}$  and  $\hat{\gamma}$  correspond to the high order ME effects.

## 1.4 A review of structural studies of BiFeO<sub>3</sub> and its derivatives

BFO has been investigated both for use in ferroelectric compositions as well as for multiferroic applications. Good reviews of this material are presented by [1]. One of the unique features of BiFeO<sub>3</sub> is the way its structure is so sensitive to strain and doping. For example, Wang *et al.* [52] have shown for the first time that epitaxial thin films can display a large amount of polarisation at room temperature, approximately 10 times more than the bulk structure. At first, it was thought that this anomalous polarisation occurs only in the thin films and it results from a secondary phase but Lebeugle *et al.* [53] have reported that such a large polarisation can also be observed in a single crystal of BFO and is an intrinsic characteristic of BFO. Compressive strain can also produce such a large polarisation that arises from transformation of cubic-based perovskite to tetragonal-distorted perovskite with  $c/a$  in the range 1.24 to 1.26 [54]. This is the so-called T-phase, which has been found in epitaxial thin films grown on LaAlO<sub>3</sub> [54, 55]. Rossell *et al.* [56] found a T-phase with  $c/a= 1.27$  for a 60nm BFO thin film. For BFO epitaxial thin film grown on SrRuO<sub>3</sub>/SrTiO<sub>3</sub>, H. J. Lee *et al.* [57] observed changes in the lattice parameters as well as the displacement Fe atoms associated with the polarization  $\sim 15$ nm. In terms of theoretical calculations, this epitaxial-strain effect has been demonstrated using density function theory (DFT), where compressive strain initially causes slight tetragonal distortions before an abrupt change to the supertetragonal T-phase at

strains more than -4% as shown in figure 1.11 [58].

One interesting feature of BFO, strain gradient field can be used to provides photostriction and photovoltaic effects, and in BFO thin films these can be significantly enhanced via ultrafast optical excitation by a significant magnitude in comparison to static strain gradients [59] . It has also been demonstrated experimentally using scanning probe microscopy that specific polarisation switching in (001) BFO may enable the realisation of magnetoelectric memories [60]. The localized electric field in BFO resulting from photoinduced charge separation has shown the anisotropic elastic deformation of the unit cell, which may lead to the ultrafast control of magnetism through the magnetoelectric coupling which may hence open a new gate to manipulate mechanic/magnetic characteristics with light [61]. It has also been shown that tuning the depolarizing field can control the BFO domain walls precisely and this could open interesting pathways for room temperature multiferroic systems [62].

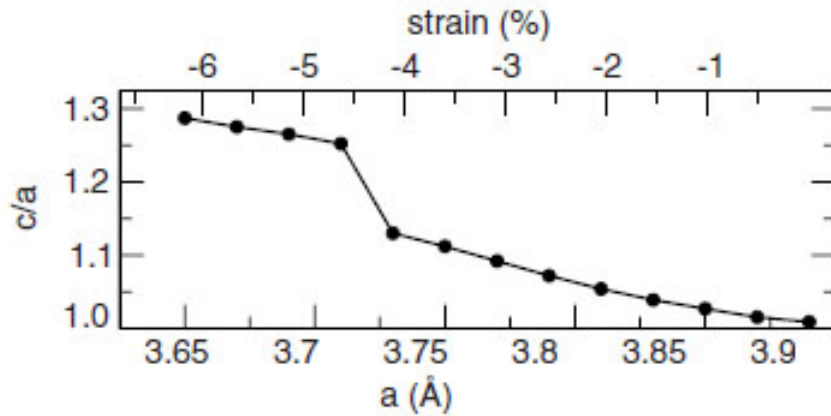


Figure 1.11: The corresponding evolution of  $c/a$  of the pseudocubic cell as a function of biaxial strain or substrate lattice parameter. [58]

Since ferroelectricity is an intrinsic property of BFO and related to its structure, huge investigations have been done through the chemical modifications such as using different RE elements. To do this, RE elements such as Sm, Gd and Dy have been exploited as dopants on to A site lattice on BFO thin films [20]. Be-

sides, RE elements such as La, Nd, Sm and Gd have also been used as dopants on to A site lattice on BFO thin films [27, 28]. As a result of these investigations, a cubic perovskite-based structure is distorted to either (FE) rhombohedral or antiferroelectric (AFE) orthorhombic depending on composition with considerably improved electro-mechanical and magnetic characteristics. In the AFE phase formed by doping with Nd or Sm, a  $\text{PbZrO}_3$ -like structure is observed [27, 63]. However, Karimi *et al.* [27] observed that the  $\text{PbZrO}_3$ -like phase in BFO-based ceramics showed additional diffraction spots in electron-diffraction (ED). This cell is elongated “oddly” along the  $c$  axis to twice the parameter of the  $\text{PbZrO}_3$  structure and hence resulted in displaying the cells-parameter to be  $\approx \sqrt{2}a_p \times 2a_p \sqrt{2} a_p \times 4a_p$ , where  $a_p$  is the primitive perovskite-like unit cell parameter. Figure 1.12 shows a phase diagram for  $\text{Nd}^{3+}$  substitution to (A-site)  $\text{Bi}^{3+}$  and sharing the stable region for the  $\text{PbZrO}_3$ -type structure at the morphotropic phase boundary (MPB) based on x-ray powder diffraction (XRD), and electron diffraction (ED) [27]. The term “morphotropic” refers to a phase transitions which results in a change of symmetry, but no significant change in atomic arrangement, due to changes in composition [64]. Firstly, these antiphase boundaries are imaged with both scanning transmission electron microscopy and transmission electron microscopy to investigate how quantitative it is possible to be about determining polarisation with atomic resolution microscopy. Secondly, the structure and chemistry of crosses formed by the intersection of two APBs is determined. Kalantari *et al.* [9] showed that using  $\text{Ti}^{4+}$  as a donor dopant on the B-site (Fe) with 15% Nd doped BFO-based ceramic successfully decreased the leakage current, and eventually resulted in decreasing the conductivity. By increasing the Ti-doping concentration roughly to  $\text{Ti} = 10\%$ , during their works, they observed that the behavior of the Curie point displays a non-linear dependence on doping whereas the Néel point varies linearly with doping.

The structures presented in a sample of doped  $\text{BiFeO}_3$ -based perovskite

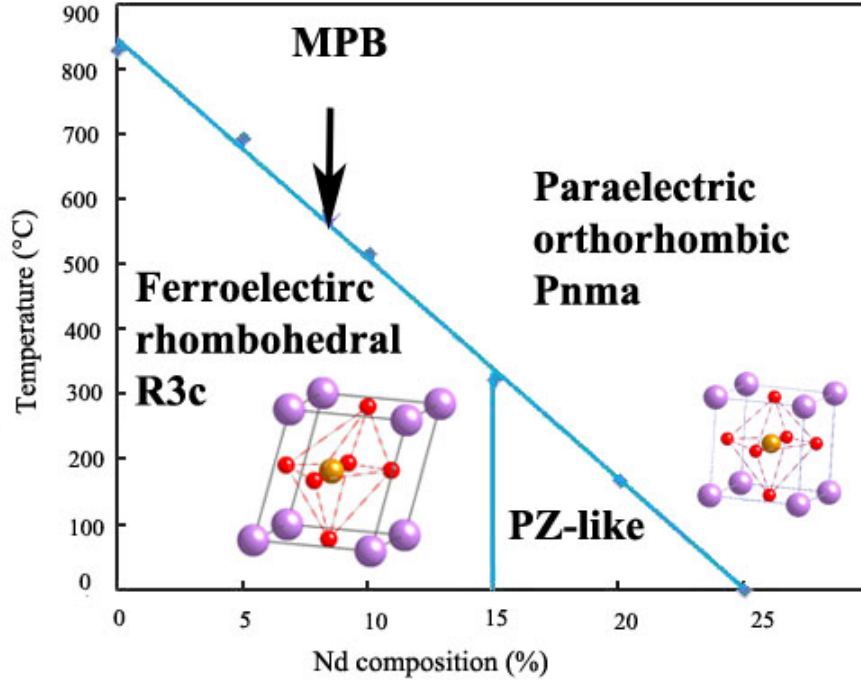


Figure 1.12: Phase diagram for  $\text{Bi}_{1-x}\text{Nd}_x\text{FeO}_3$  presented using XRD, DSC, Raman, and TEM data together [27].

of a composition  $\text{Bi}_{0.85}\text{Nd}_{0.15}\text{Fe}_{0.9}\text{Ti}_{0.1}\text{O}_3$  has been studied in detail in several publications by MacLaren, Reaney and others. Reaney *et al.* [9, 65] and MacLaren *et al.* [66] have showed that co-doping with Nd and Ti can create novel defects: Nd-rich nanorods. The Nd-rich nanorods are occurred due to the excess of Ti doping to the B-site lattice resulting in the creation of Nd vacancies. If the Ti doping level is very high (Ti-doping > 3%), the Ti-cored APBs are created. Additionally, Ti-rich antiphase boundaries (APBs) are observed in this material. These APBs are comprised of two main structural units: Flat terraces and steps [67, 68]. This thesis examines in further detail structures found on such antiphase boundaries in this  $\text{Bi}_{0.85}\text{Nd}_{0.15}\text{Fe}_{0.9}\text{Ti}_{0.1}\text{O}_3$  composition. Firstly, these antiphase boundaries are imaged with both scanning transmission electron microscopy and transmission electron microscopy to investigate how quantitative it is possible to be about determining polarisation with atomic resolution microscopy. Secondly, the structure and chemistry of crosses formed by the intersection of two APBs is determined.

# Chapter 2

## Instruments and sample preparation

### 2.1 Introduction

This thesis is centred on the atomic resolution (scanning) transmission electron microscopy of doped  $\text{BiFeO}_3$  multiferroics. It therefore follows that resolution is a highly significant factor in this study. Since the invention of electron microscopy in the 1930s, resolution has been one of the most important areas of development. For several decades the resolution was limited to  $\approx 100\lambda$ , where  $\lambda$  stands for the wavelength of the electrons, due to spherical and chromatic aberrations. Much effort has been expended by the scientific community in reducing these aberrations to enhance the the resolution. Specifically, the development of hardware aberration correctors has enabled major steps forward in atomic resolution electron microscopy [69], including the ability to image oxygen in oxides [70, 71]. Modifying the aberration corrected scanning TEM/STEM instruments equipped with electron-energy loss (EELS) spectrometers are now capable of mapping the elemental composition and chemical bonding with atomic resolution. But of equal

importance is the use of negative spherical aberration (NCSI) in conventional TEM to improve the contrast of atomic columns of light elements such as O, at high resolution [70, 71]. This chapter describes the apparatus and specimen preparation procedures that have been used in this project.

In order for the research presented in chapters 4 and 5 to be put into context, it is first necessary to explain the working principles of the microscopes used in this research. It is also necessary to explain the principles behind the preparation of the specimens required for this work. This chapter will begin with the background theory of TEM and STEM instruments as well as a summary of electron sources. Following this, background information on electromagnetic lenses and their impact on principal aberrations are addressed. After that, specimens, specimen holders, and electron detectors are discussed. Various imaging modes for both TEM and STEM will be covered. Finally, Electron Energy Loss Spectroscopy (EELS) and spectra discussed.

## **2.2 The basic principles of transmission electron microscopy**

In order to illustrate the principal components of a conventional transmission electron microscopy (CTEM), a schematic diagram in figure 2.1 is provided, which shows the optical layout of the FEI Tecnai T20 used during the current work at the University of Glasgow. A TEM is comprised by the following: an illumination system (the electron source, C1, C2 aperture), a magnification system (objective lens, diffraction lens, intermediate and projector lenses, objective, and selected area apertures) and finally an image recording system. These will be described in detail in turn in sections 2.3. Regarding the electron sources, all electron microscopes require a source of electrons, which is often located at the top of the microscopy.

Important properties of electron sources are beam brightness, current, energy spread and high-voltage stability and these are dependent on the electron gun type. In this section, only the two main types of electron sources are considered: thermionic and field-emission sources. These will be discussed in Section 2.2.2 below.

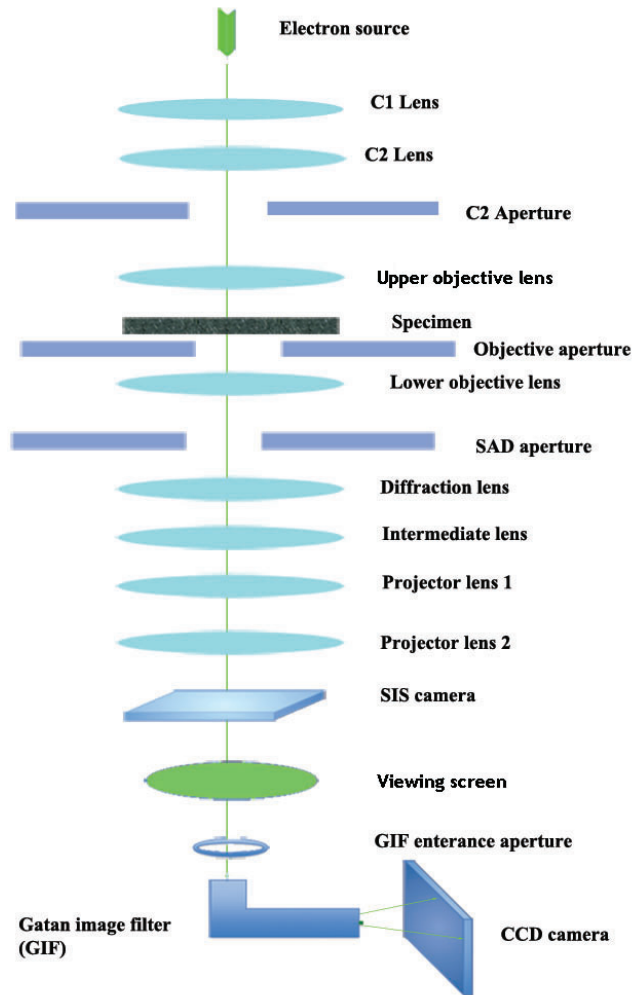


Figure 2.1: Schematic diagram of the FEI Tecnai T20 TEM illustrating the illumination and magnification system, SIS camera and Gatan Image Filter (GIF), which are utilised to generate energy filtered images and EELS spectra.

The illumination system is comprised by two condenser lenses (C1 and C2) and a set of condenser apertures underneath the C2 lens. The purpose of the C1 lens is to obtain a demagnified image of the electron source and hence the lens controls the spot size. The C2 lens controls the illumination mode of the beam and thus the intensity on viewing screen. Another parameter that affects the intensity is the type of C2 aperture. A small aperture, yields an electron beam with higher spatial coherence, however it substantially decreases current density.

The magnification system, which is formed by the objective (imaging), intermediate and projector lenses (magnifying), of the TEM is also illustrated in figure 2.1. The objective lens (upper and lower) determines the overall achievable resolution of the microscopy and is used to control how images are formed by selecting a parallel beam or a very fine probe. Objectives with large pole spacings allow a greater angle of sample tilt, but compromise the achievable resolution. In order to control the image contrast, an objective aperture is set in front of the lower objective lens as shown in figure 2.1. Finally, the formed image or diffraction pattern is magnified by the projector lenses and projected onto the viewing screen or camera.

The main characteristic of CTEM is using a wide beam in which the whole area of interest is illuminated by a parallel beam and an image is formed by the objective lens. When the sample is exposed to the electron beam, electrons are often elastically scattered by the sample, and this can be imaged in a diffraction pattern. Specific diffraction spots can be selected by an objective aperture to form an image. The imaging system is set so that the scattered electrons are subsequently focused to form an image or the diffraction pattern on the viewing screen. In CTEM there are two common imaging techniques, bright field (BF) and dark field (DF) imaging and this will be discussed later in section 2.3.

## 2.2.1 The Basic Principles of Scanning Transmission Electron Microscopy

The scanning transmission electron microscopy (STEM) has a similar layout to the CTEM, with some additional features. A schematic diagram for the STEM is shown in figure 2.2. The basic STEM is comprised by an electron source, condenser lenses, and can include an aberration corrector (see section 2.2.3.3), a system of projector lens, some detectors, and other potential features such as a camera system (see section 2.4) spectrometer or an EDX spectrometer. The electron source that is used is often a field emission gun in order to reduce both the source size and more importantly to reduce the energy spread. Depending on the manufacturer, either two or three condenser lenses are used in order to control both the illumination angle and the beam current at the sample. Details on the detectors and imaging, and spectrometers and spectroscopy in the STEM will be discussed later in this chapter, in sections 2.3.3 and 2.4.

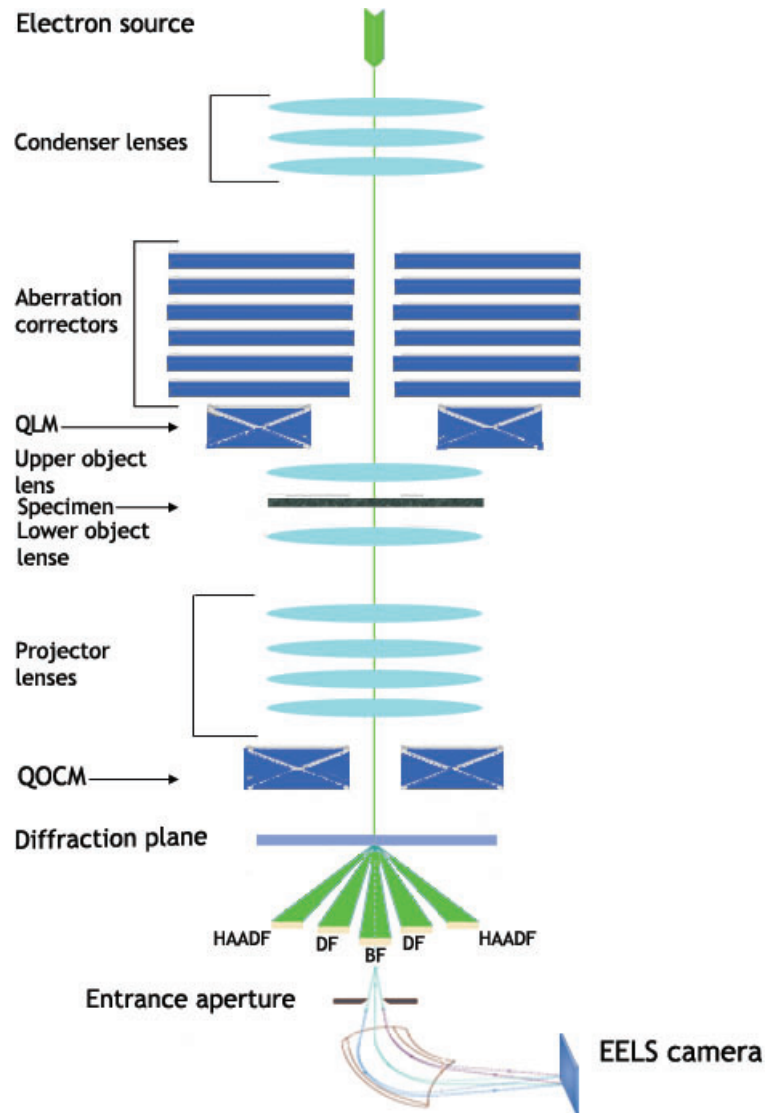


Figure 2.2: A schematic diagram of the main components of an aberration-corrected STEM. Starting with an electron gun at the top that ultimately forms a nanoprobe that is focused on the specimen after a series of aberration correctors. A quadrupole lens module (QLM) is used for coupling the corrector electron-optically to the objective lenses. A quadrupole-octupole coupling module (QOCM) is used for optimised coupling of inelastically scattered electrons into the spectrometer.

## 2.2.2 Electron sources

The most common electron sources that are used in electron microscopes are summarised as follows:

- Thermionic sources most commonly consist of a tungsten or a Lanthanum

hexaboride ( $\text{LaB}_6$ ) filament and provide electrons when heated. An example of this is shown in figure 2.3. After the electrons leave the source due to the high applied voltage between the cathode and the anode plates, the trajectory of the electrons can be controlled and hence modified by the “Wehnelt” system. The “Wehnelt” converges the electrons into a crossover before they enter the illumination system, as shown in figure 2.3. However,  $\text{LaB}_6$  has typically been chosen as an electron source instead of a tungsten source because of its lower work function, but the brightness, which is the current density per unit solid angle of the electron source, is much higher than in the latter. In fact, work functions,  $\Phi_{\text{LaB}_6}$ , ranging from  $\Phi_{\text{LaB}_6}=2.4\text{eV}$  to  $\Phi_{\text{tungsten}}=4.5\text{eV}$  will provide a brightness in the range  $5 \times 10^{11} \text{A/m}^2\text{sr}$  to  $10^{11} \text{A/m}^2\text{sr}$  at 100kV [72, 73], respectively. Thus, a smaller source size gives a better spatial coherency. It is worth pointing out that the better coherency as well as longer life are other advantages that a  $\text{LaB}_6$  electron source has over a tungsten source [72]. A  $\text{LaB}_6$  filament can be heated to an operating temperature of 1700K which is enough to generate electrons from the surface of the specimen.

- A field-emission source is crucial for the best performance of STEMs in terms of analysing structures as the result of an increased brightness by a factor of  $10^3$  over a  $\text{LaB}_6$  electron source. For STEMs, the very small emitting area of the tungsten tip also makes it possible to focus a super-fine electron probe onto the surface of the specimen [72]. This high brightness and small focused probe size ultimately enhances the signal-to-noise ratio, image resolution and improves or enables more detailed data analysis [74].

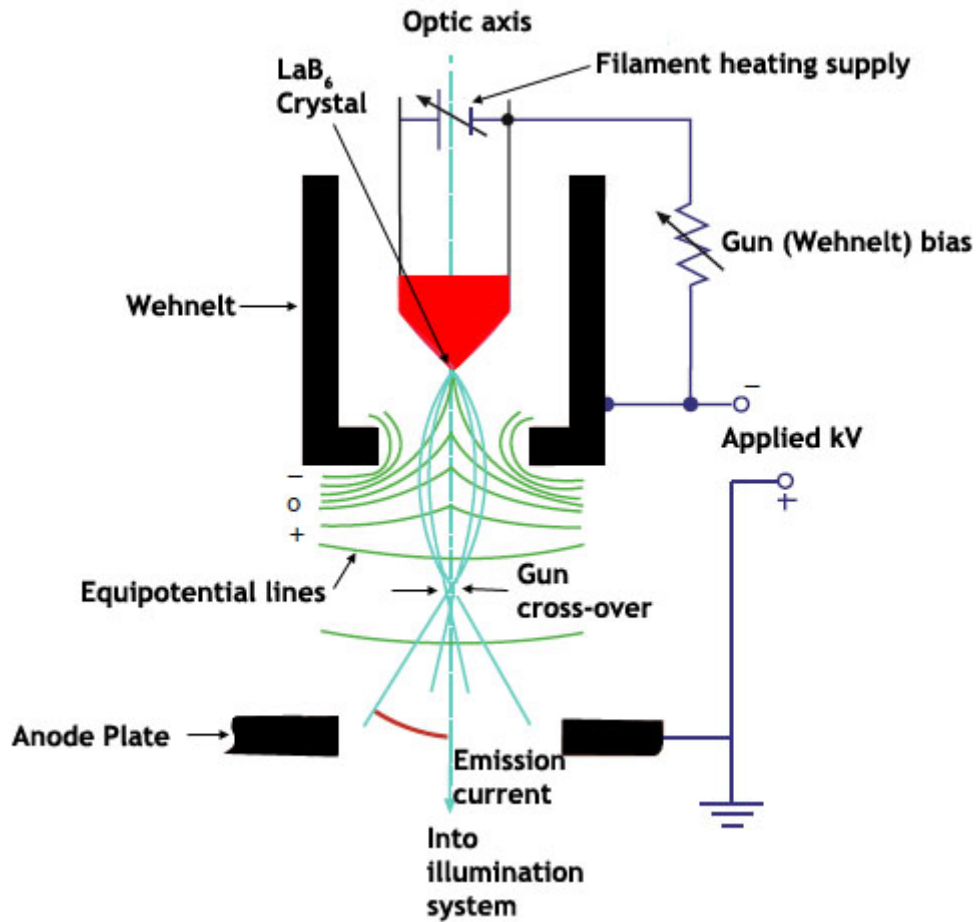


Figure 2.3: A schematic diagram of thermionic ( $\text{LaB}_6$ ) gun. Once a high voltage is applied between the cathode and the anode plates, the Wehnelt converges the electrons into a crossover. The electrons are then controlled and passed into the TEM illumination system [72].

## 2.2.3 Electron lenses aberrations and corrections

In this section, the geometry of the lenses utilised in microscopes will be discussed along with their aberrations and methods used to correct them.

### 2.2.3.1 Electron lens geometry

As has been mentioned in the above sections, both TEM/STEM microscopes utilize many electron lenses in order to shape the trajectory of the electrons. Then, the electrons are accelerated down the illumination system using an anode.

In 1927, electrons were successfully deflected and focused using either electrostatic or electromagnetic lenses [72]. In modern microscopes, electromagnetic lenses are chosen and are found to be better for electrons, which can be deflected by an applied magnetic field. This is due to their low-voltage insulation and also that they have lower aberrations and better stability than electrostatic lenses [75]. For these reasons, the electromagnetic lenses will be discussed in more detail.

A magnetic electron lens is usually formed by two major parts: the pole-pieces and a series of copper coils, which surround the pole-pieces as shown in the schematic diagram in figure 2.4. Starting with the pole piece, which is a a cylindrically symmetrical material designed from a soft magnetic substance, commonly iron, that has a gap formed through it called the bore. Since the bore has a hole, it allows the electron beam to pass smoothly through it. Most electron lenses are composed of two pole-pieces (the upper and lower sections) isolated by a gap. The strength of the magnetic field is varied in the pole-pieces which in turn controls the trajectory of the electrons [72]. The heat produced by the current passing through the coils is often significant, and therefore a water cooling system is a very important part of most lenses. When an electron with a charge (-e) passes through a magnetic field ( $\mathbf{B}$ ) it will experience the Lorentz force ( $\mathbf{F}$ ), which can be formulated as below:

$$\mathbf{F} = -e(\mathbf{v} \times \mathbf{B}) \quad (2.1)$$

and its magnitude is:

$$F = evB\sin(\alpha) \quad (2.2)$$

where  $\mathbf{v}$ ,  $\mathbf{B}$  and  $\alpha$  represent the electron velocity, the magnetic field strength, and the angle between  $\mathbf{v}$  and  $\mathbf{B}$ . The direction of  $\mathbf{F}$  can be determined from the above equation (2.1), which is perpendicular to  $\mathbf{B}$  and  $\mathbf{v}$ . If  $\alpha=0^\circ$ , the  $\mathbf{v}$  component is

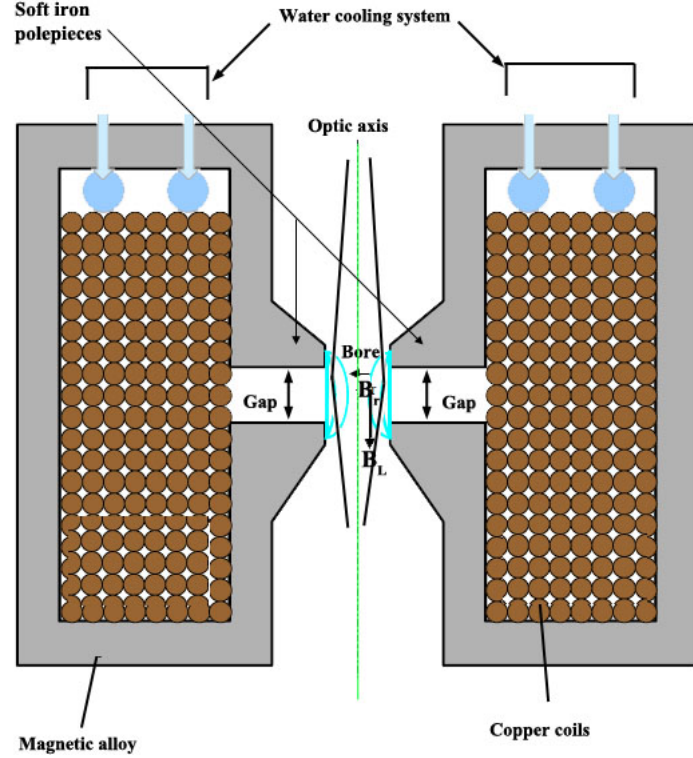


Figure 2.4: A schematic diagram of a pole-piece structure as well as the change in the direction of rays passing through the lens due to the radial component ( $B_R$ ) of the magnetic field.

parallel to  $\mathbf{B}$  component and therefore no force is experienced by on the electron. Any perpendicular field components will produce a force on the electrons, which will produce a circular motion about the magnetic field. The subsequent electron trajectory will depict a helix. The rotational motion interacting with the magnetic field will then cause a force towards the axis which will be the cause of focusing the spiraling beam towards the optic axis. So, the electrons on the optic axis will pass through the centre and experience no force but electrons off the optic axis will spiral towards the centre. The reason behind the helical path of the electrons is determined by both the longitudinal and radial components  $B_L$  and  $B_R$ , respectively [72]. The major effect on the spatial resolution of microscopes is determined by the spherical aberration of the lenses, which is caused by  $B_R$  and this will be discussed later in more detail. Since the strength of the magnetic field is essential for controlling the trajectory of the electrons and the focal length of the lens, it is crucial to assign a short focal length in order to diminish the spherical aberration. That is, for

high resolution, it is important to keep the focal length short by means of a very strong lens current. The reasons for this will be discussed further in the following sections. Moreover, using an aberration-corrected CTEM with a 3<sup>rd</sup> generation using multipole lenses such as hexapole or quadrupole-octupole as the C<sub>s</sub>-corrector, the spherical aberrations can also be minimised.

Since the lens is round, as mentioned above, spherical aberration is therefore inevitable [76, 77]. Aberrations due to the nature of the lenses are considered to be pivotal for high spatial resolution of the microscopy and ultimately for high-resolution images to be interpretable. These aberrations can be classified into two main categories: geometric, or monochromatic and chromatic aberrations. However, the STEM data presented in this thesis is unaffected by chromatic aberration effects.

### 2.2.3.2 Geometric aberrations

Simple types of geometric aberration include spherical aberration “C<sub>s</sub>”, axial astigmatism and coma. These can be described as follows:

- Spherical aberration: These occur when all paraxial rays (smaller angle  $\alpha$ ) and off-axis rays (larger angle  $\alpha$ ) are not focused at the same point along the optic axis such as F in the Gaussian image plane after passing through the lens, and this is shown in figure 2.5. Since the off-axis rays are distributed radially at the Gaussian image plane, a blurred disk will be imaged instead of a point focus and this is shown in figure 2.5. The influence of spherical aberration on the radius of the disk in the Gaussian image plane is described by:

$$r_s \approx C_s \alpha^3 \tag{2.3}$$

where C<sub>s</sub> is the coefficient of the lens spherical aberration. Scherzer (1936) showed that positive spherical aberration was inevitable in all cylindrically symmetric electron lenses [76]. Until recently, this could not be avoided, just

minimised by careful lens design, and compensated for in some imaging techniques (Scherzer 1947) [78].

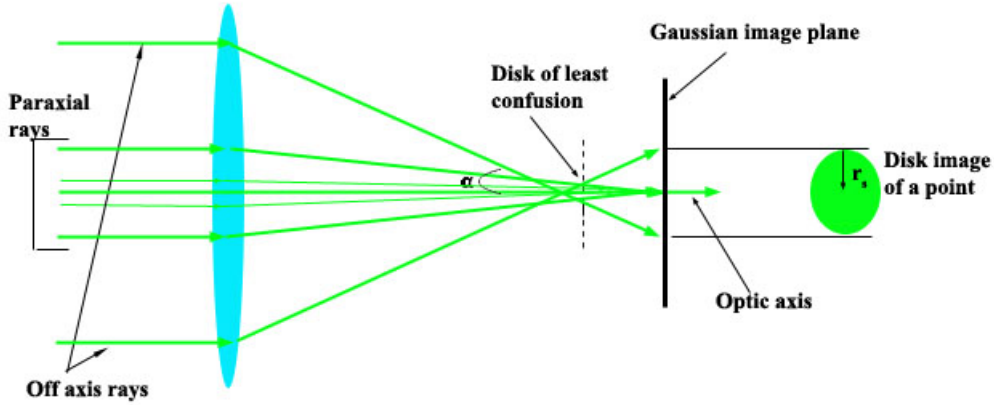


Figure 2.5: A schematic illustration of spherical aberration, where the off-axis rays are not focused at the same point in the Gaussian plane.

- Axial astigmatism: The effect of this type of aberration appears for the following reasons: 1) inhomogeneities in the soft magnetic materials that are used for the polepieces of the lens. 2) imperfections in the manufacture of the bore of the lens, which must be cylindrically symmetric. 3) contamination situated on the bore of the pole-piece and on apertures in the column. These effects can make the strength of the magnetic field  $B_z$  non-uniform in the bore, with the result that the focal points for those rays travelling in the  $x$ - $z$  and  $y$ - $z$  planes are no longer the same ( $F_x \neq F_y$ ). Thus, at the Gaussian focal plane the spot appears elliptical rather than round as shown in figure 2.6. The best that can be achieved is known as the disk of least confusion, where the smallest image of an object is formed. However, it is possible to correct the axial astigmatism using a quadrupole lens or a stigmator.
- Coma aberrations: these occur when all paraxial (rays that travel near the optic axis) rays and off-axis rays are focused at different points such as  $F_x$  and  $F_y$  and give a comet-shaped beam in the Gaussian image plane after passing through the lens as a result of those rays arising from an object slightly off

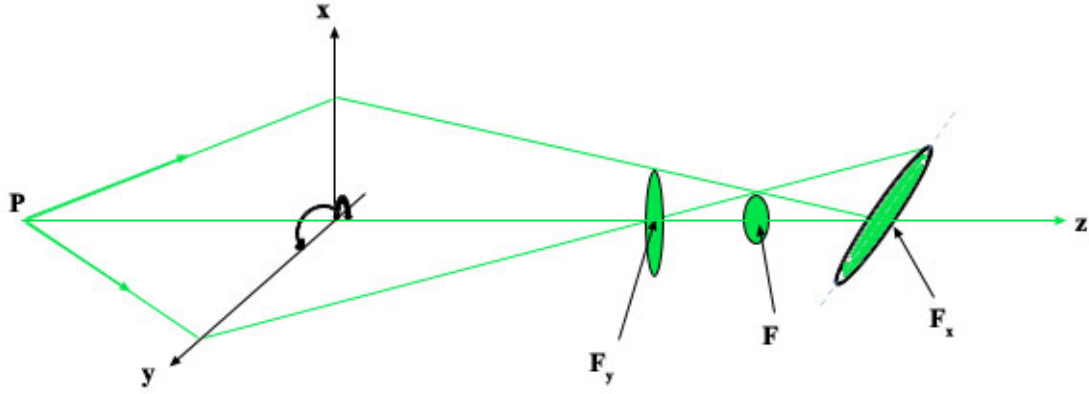


Figure 2.6: A schematic ray diagram illustrating axial astigmatism. Since the effect of the magnetic field is not the same in the x and y directions, rays may travel in the x-z plane with the long axis normal to the y-z plane resulting in an ellipse centered around the  $F_x$  point or vice versa around  $F_y$ , or into a circle of smallest radius (the disc of least confusion) [75].

the optic axis. These aberrations can be corrected (coma-free alignment) by correct alignment in which the electron beam in the microscopy is aligned along the optic axis of the objective lens, as shown in figure 2.7.

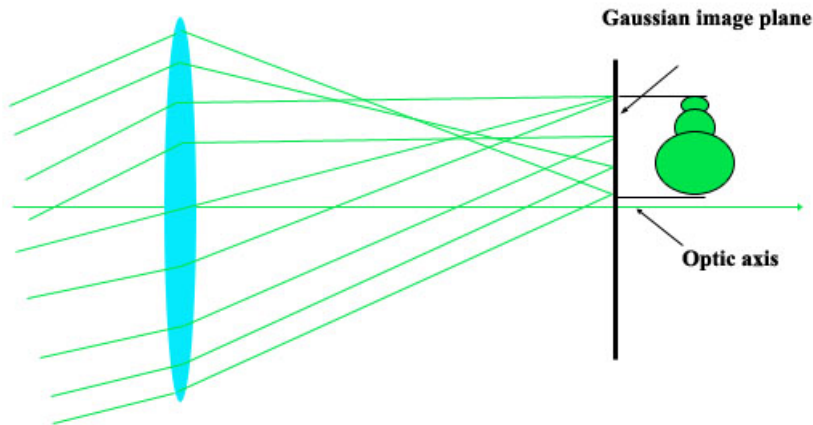


Figure 2.7: A schematic diagram of a comet-shaped aberration due to rays that travel near the optic axis, which results in off-axis rays being focused at different points.

The geometric aberrations of a lens can be defined in terms of the wave aberration function  $\chi(\theta_x, \theta_y)$ , which is defined as the difference between the ideal spherical wavefunction and the real wavefront for a given lens. This includes the simple aberrations described above (spherical aberration, astig-

matism and coma), as well as many higher order aberrations). Although geometrical aberrations can be presented in several equivalent systems of nomenclature such as Hawkes and Kasper in 1989 [79], Saxton in 1995 [80], and Uhlemann and Haider in 1998 [81], here they will be expressed in notations used by Krivanek *et al.* [82]:

$$\begin{aligned}
\chi(\theta_x, \theta_y) = & (2\pi/\lambda)[C_1(\theta_x^2 + \theta_y^2)/2 + C_{1,2a}(\theta_x^2 - \theta_y^2)/2 \\
& + C_{1,2b}\theta_x\theta_y + C_{2,1a}\theta_x(\theta_x^2 + \theta_y^2)/3 \\
& + C_{2,1b}\theta_y(\theta_x^2 + \theta_y^2)/3 + C_{2,3a}\theta_x(\theta_x^2 - 3\theta_y^2)/3 \\
& + C_{2,3b}\theta_y(3\theta_x^2 - \theta_y^2)/3 + C_3(\theta_x^2 + \theta_y^2)^2/4 \\
& + C_{3,2a}(\theta_x^4 - \theta_y^4)/4 + C_{3,2b}\theta_x\theta_y(\theta_x^2 + \theta_y^2)/2 \\
& + C_{3,4a}(\theta_x^4 - 6\theta_x^2\theta_y^2 + \theta_y^4)/4 \\
& + C_{3,4b}(\theta_x^3\theta_y - \theta_x\theta_y^3)]
\end{aligned} \tag{2.4}$$

Where where C denotes an axial aberration,  $\theta_x = \theta \cos(\phi)$  and  $\theta_y = \theta \sin(\phi)$ .

Aberration coef- ficient	Conventional name	Azimuthal Sym- metry
$C_{0,1}$	Image shift	1-fold
$C_{1,0}$ or $C_1$	Defocus	Infinite
$C_{1,2}$	Regular astigmatism	2-fold
$C_{2,1}$	Axial coma	1-fold
$C_{2,3}$	3-fold Astigmatism	3-fold
$C_{3,0}$ or $C_3$	Spherical Aberration ( $3^{rd}$ order)	(0) Round
$C_{3,2}$	2-fold Astigmatism of $C_s$ (or $3^{rd}$ order 2-fold Astigmatism)	2-fold
$C_{3,4}$	4-fold Astigmatism (a and b)	4-fold

Table 2.1: Aberration coefficients and their corresponding conventional names [82].

### 2.2.3.3 Aberration correction

Spherical aberration limits the probe angle in STEM, and the objective lens aperture size in TEM, so limits the resolution in both cases. Therefore, a negative spherical aberration is needed to cancel out the positive spherical aberration in the lens. This can only be created by the use of a diverging lens. For this purpose, the diverging lens can only be created with multipole lenses (e.g. quadrupoles, sextupoles, octupoles, etc.). By combining several elements such as three octupoles (O2, O4 and O6) and four quadrupoles (Q1, Q3, Q5 and Q7), a diverging effect in all azimuthal directions can be created (at least up to a certain angle). This kind of corrector was successfully achieved by Zach and Haider [83], and at atomic resolution in STEM by Krivanek *et al.* [82], which is shown in figure 2.8. Additionally, another type of corrector such as a hexapole corrector, was successfully implemented by Haider *et al.* [84]. Interestingly, this has become the most widely utilised corrector in TEM/STEM instruments. At higher angles, higher order aberrations become dominant and aberration correction fails. Correctors allow probes to be created with higher angles of incidence in STEM, whilst still remaining in phase. This appropriates smaller probe sizes by the Abbe criterion. Ultimately, this allows larger angles to be used for the objective aperture in TEM, whilst still keeping all beams in a good phase relationship and the image resolution can be increased.

The corrector consists of three octupoles (O2, O4 and O6) and four quadrupoles (Q1, Q3, Q5 and Q7). The radial elongation of the beam through the corrector is indicated along two orthogonal axes  $x$  and  $y$  (the line traces overlap when the beam is round). Schematic and ray path diagram of the quadrupole-octupole corrector are shown in figure 2.8.

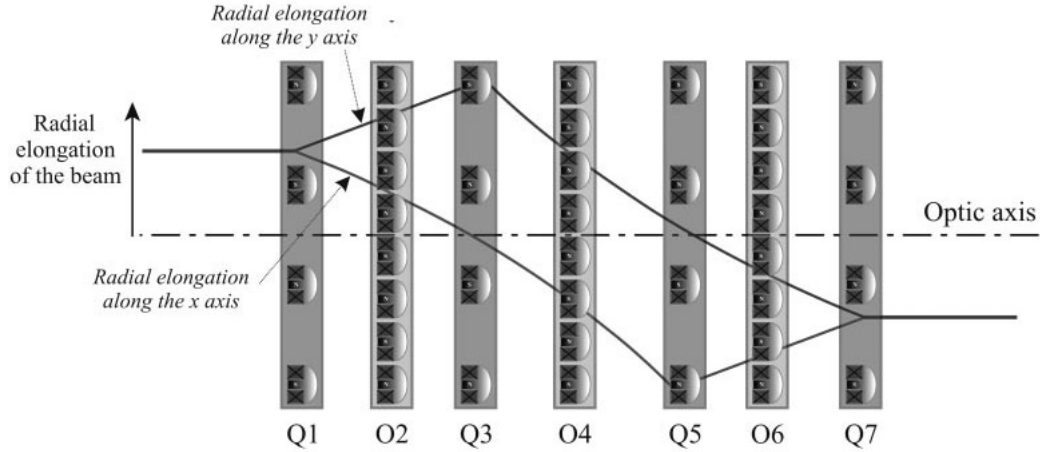


Figure 2.8: A schematic ray diagram of the quadrupole-octupole corrector. The radial elongation of the beam through the corrector is indicated along two orthogonal x and y axes [85].

#### 2.2.3.4 Specimen and specimen holder

Electron microscopy instruments make use of transmitted electrons, so for all TEM and STEM analysis, sample thickness is critical. Samples need to be prepared from a bulk material and need to be thin enough to be observed by the transmission of electrons with minimal plural scattering, without compromising the structure. TEM holders for the sample need to be manufactured for the microscopy that enable enough movement in the x, y and z directions for multiple reasons. These include allowing the area of interest to easily be found, allowing sufficient tilting for a crystal to be oriented along a low symmetry direction. By allowing also enough stability to allow atomic resolution imaging and spectroscopy. This section describes the basics of specimen preparation and specimen holders.

For the current work, two specimens were processed since both TEM and STEM have been exploited. This will be discussed as below.

The specimens were prepared for STEM by a conventional procedure, which includes the processes of cutting, dimpling and ion beam milling. Once the samples are thin enough, they are coated with a few nanometers of carbon to pre-

vent them from charging when exposed to the electron beam [67]. For some samples, a focused ion beam (FIB) instrument was used. This procedure is summarized as below:

- Cutting and thinning: Firstly, several disks of 3mm diameter were cut from a 10mm sintered ceramic pellet utilizing a specific ultrasonic disk cutter. Secondly, all the disks were thinned to about 80-100 $\mu\text{m}$  by hand-grinding.
- Dimpling: The thin disks from the previous stage were then put into a Gatan dimple grinder in order to thin the disk's center to  $\approx 20\mu\text{m}$ . The dimpler instrument uses a rotating brass wheel, which is coated by diamond paste to gently polish the centre whilst only removing a specified thickness. For final polishing, a very fine diamond paste was used with a soft felt wheel to remove debris left behind from the grinding process. Manual rinsing in water is also essential.
- Ion milling: In order to get the thickness of sample ready for investigation in the TEM and STEM, the thin disks from the previous step were put into a Gatan Precision Ion Polishing System (PIPS); the specific model used here, number 691, has been adapted to include a low voltage supply. There are two argon ion guns that are used to direct the ions with a desired angle upon the sample surface. The incident angles on the sample surface are chosen to be small for two main reasons: Firstly, ion implantation is noticeably minimised at a glancing angle [72]. Hence if the ion guns are operated at  $\pm 4^\circ$  incident angle, this would allow both sides of the sample to be milled simultaneously. Secondly, because of the flat surface and minimal preferential milling of softer areas of the sample. During the work presented here, specimens were milled with an acceleration voltage of 4kV while being rotated at 2rpm for about  $\approx 4$  hours. Then, the acceleration was decreased to 1kV for  $\approx 2 - 3$  hours and 0.5kV for  $\approx 30$  minutes up to the point where light is visible through a small

hole that forms at or near the center of the specimen. The reason behind gradually decreasing the acceleration voltage is to remove any damage from the surface caused by the ion bombardment at higher voltage.

- Carbon coating: After the ion polishing stage, the specimens were carbon coated on either side in thermal evaporation system in order to prevent them from charging when exposed to the electron, which might lead to some unwanted effects during investigation with TEM and STEM instruments such as stage drift or even sample damage. However, this charging effect cannot be eliminated entirely and its effect has been roused specially for the thin sample over the thick one. This will be discussed in more detail in chapter 4.

For the special case of the high resolution transmission electron microscopy (HRTEM), a suitable sample for investigation was made by a different procedure, since HRTEM analysis requires the specimen to be very thin so that no contrast inversion takes place. Firstly, electron backscatter diffraction (EBSD) was utilised to show the crystallographic orientations of grains in the specimen (with a light carbon coating utilised to minimise charging, as described previously) [86, 87]. This was achieved using a FEI-Quanta 200F equipped with an EDAX-TSL EBSD system. A grain was then taken with  $\langle 100 \rangle$  direction perpendicular to the surface. After choosing a suitable orientation for the extraction of a thin section, the sample was placed in a FEI Nova 200 DualBeam FIB and a thin specimen was lifted out from an adequate location with the correct orientation. The specimen was then attached to an Omniprobe and final thinning was then completed to a thickness of around 100nm using the FIB. It was then confirmed using CTEM that the chosen grain was perfectly located in the section in the correct orientation. Final thinning and removal of surface damage was then performed with a Fischione Nanomill with argon particles at 500eV accelerating voltage, from both sides, until the thickness of the area of interest was sufficiently small to be suitable for HRTEM.

Once a specimen is ready for microscopy, different types of holders are then available to load the specimen depending on the application. Two categories of sample holders are top-entry and side-entry holders. The top-entry holder is a cartridge containing the sample which is mounted inside the microscope. The top-entry holders should be small enough to fit through the bore of the objective lens pole-piece, and since they are detached from outside of the microscopy, drift problem is relatively low. Also, they are easy to manipulate in terms of tilting or rotating, which is beneficial. As a result, the top-entry holders are regarded to be more stable than the others, and has been used in the current work at SuperSTEM (see sections 4.2 and 5.2). On the other hand, the side-entry holder makes use of a motor to tilt or rotate the sample. Although these holders are regarded to be standard, they connect the sample directly to the outside of the microscopy via a long lever arm, which is undesirable due to their relative instability. These holders are commonly used in FEI and JEOL microscopes due to their flexibility for large tilt ranges.

#### **2.2.3.5 Electron detectors**

In order to image whole sample in TEM with good resolution, large pixel count detectors are used. One common detector type is a CCD (Charge Coupled Device) camera with 2kx2k pixels, which has become almost universally available. Figure 2.9 shows a schematic diagram of a CCD camera widely utilised in TEMs, which uses a thin scintillator coupled by an optical fiber plate to a thermoelectrically cooled diode array (Peltier-cooled system). Different (P+ and U+ phosphor) scintillators can be utilised in order to achieve different performance characteristics. Some scintillator materials are optimised for speed, whereas others are optimised for high sensitivity, and the precise choice depends on the application. CCDs consist of regular arrays of metal oxide semiconductor capacitors that store charge after conversion with the scintillator. Each capacitor is initially charged to the same

potential and this charge is then depleted by electrons and holes produced by the incident light. Thus, the charge carriers become trapped in potential wells they can accumulate charge in proportion to the incident light intensity.

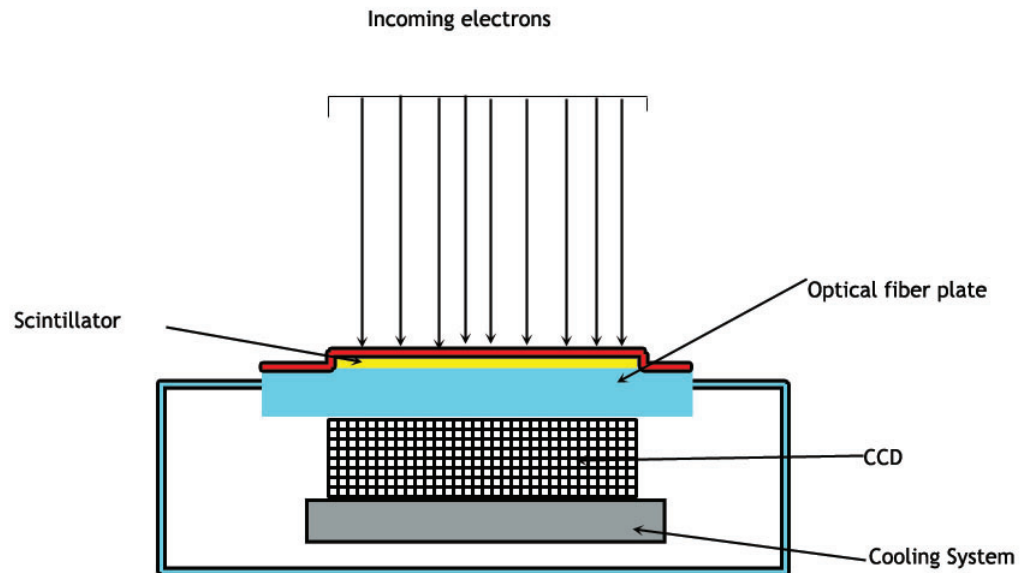


Figure 2.9: A schematic diagram of a common CCD camera that is used in TEM [72].

In STEM, the detector typically comprises of several large single or segmented semiconductor sensors or more commonly, scintillator-photomultipliers. Two sorts of detectors are utilised to record STEM images such as BF detector and high angle annular dark-field (HAADF) detector as shown in figure 2.16. For BF detector, only the direct beam is incident on the detector. In contrast, the HAADF detector only collects electrons scattered to large angles. A schematic diagram of these detectors is shown in figure 2.16.

For the HRTEM work in this thesis (see section 2.2), a Gatan UltraScan 1000xp-HS Camera within a new Model 994 was used. This US1000xp CCD is a 2kx2k CCD camera and can read out over 4 ports. For this kind of camera, the standard 4Mpixel/s read-out mode reliably produces the very highest image quality possible.

## 2.3 Imaging mode

Since the imaging system is the essential tool in microscopy to visualise the structure of the specimen, understanding the imaging techniques is critical to correct image interpretation and the main techniques used in this thesis are discussed as discussed in the following sections.

### 2.3.1 Diffraction contrast TEM

In conventional TEM, images are commonly formed using diffraction contrast in BF and DF modes in order to check samples and selecting areas for use for the atomic resolution characterisation. When the electron beam is incident on a specimen, some electrons will be elastically scattered. In a crystal, electrons will be scattered in certain directions corresponding to Bragg reflection. A diffraction pattern of the specimen is then formed in the back focal plane of the objective lens as shown in figure 2.10, and there will be a transmitted spot and one or more diffracted spots. Most of these electrons can then be stopped utilizing the movable objective aperture to select just one diffracted beam, with which to form the image. If the selected beam is the transmitted beam, then the image will be a bright field image (i.e. dark features on a bright background). However, by selecting the electrons from a Bragg diffraction spot, a dark field image is formed (i.e. bright diffracting features on a dark background).

As introduced earlier, in order to get the BF image, a small aperture is selected in the back focal plane of the imaging lens to allow only the direct beam or undiffracted electron beams that pass through the aperture to form the image. A DF image can be formed from a diffracted beam in two different ways. Firstly, the objective aperture can be shifted in order to select the diffraction spot. Secondly,

tilting the incident beam can be used so that the diffracted beam will be on the optic axis to form the image which in turn off-axis aberrations are avoided. All these methods for BF and DF image formation are shown in figure 2.10.

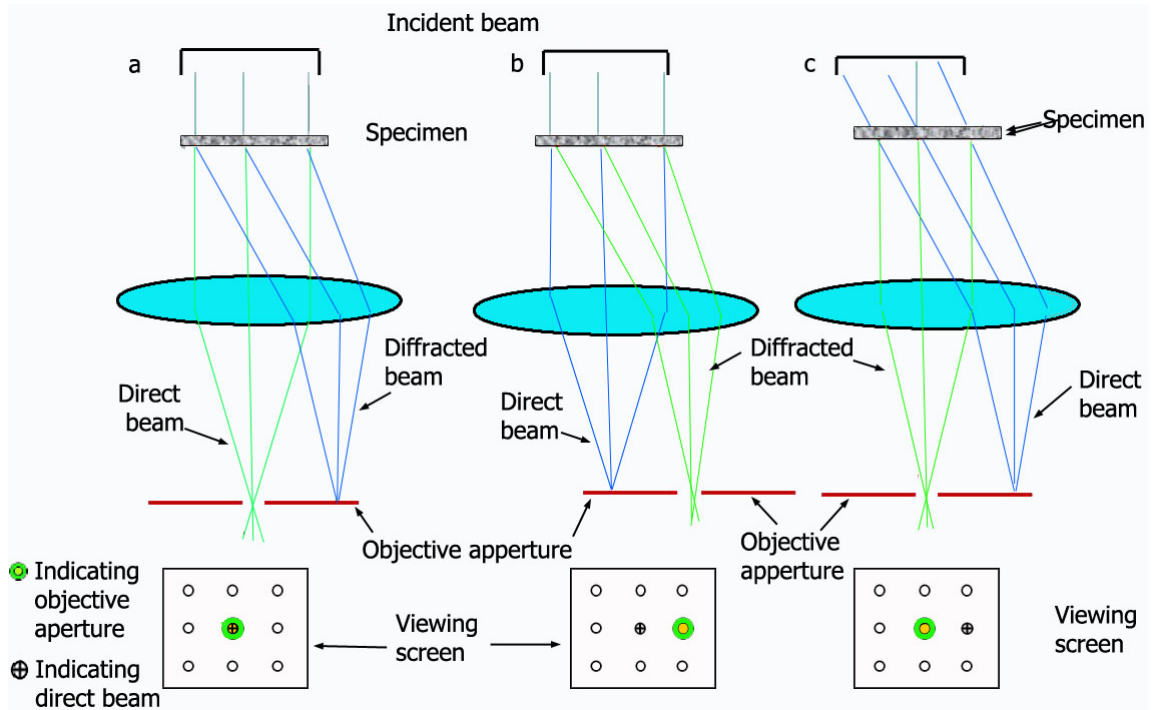


Figure 2.10: A schematic ray diagram showing the formation of BF and DF images after the direct beam interacts with a specimen. a) A BF imaging mode formation from the direct beam. b) A DF imaging mode formed from a specific diffracted beam selected by setting the objective aperture. c) A DF imaging mode formed by tilting the incident electron beam which in turn displays the scattered beam on axis. On the viewing screen under each ray diagram, the area of interest of a specimen is selected and displayed by the objective aperture in microscopy.

### 2.3.2 Phase contrast HRTEM

Phase contrast arises when more than one scattered electron beam (through a thin specimen) passes through an objective aperture and then interfere to form the image. Essentially, the phase-contrast results from interference causing fringe formation. The diffracted beam has an additional phase shift of  $\pi/2$ . Therefore, a small diffracted amplitude only results in a slight rotation of the phase angle of the resultant wave in the image and brings almost no change in amplitude. So, there is no contrast where diffracted beams are weak (i.e. for a thin specimen where it is regarded as a weak phase object (WPO)).

As mentioned in section 2.1.3, aberrations also shift phases of electrons which depends on the angle at which the electrons pass through the objective lens. This angle is equivalent to a spatial frequency in the specimen resulting in a diffraction spot. This phase shift can be plotted against spatial frequencies ( $\alpha$ ) for a lens with a specific defocus value. This is called the contrast transfer function (CTF). The CTF is defined as  $\sin\pi\chi(\alpha)$  with the range of  $\pm 1$ , where ( $\alpha$ ) is the collection angle. The contrast records its maximal value when the  $\sin\pi\chi(\alpha)$  displays the maximum values ( $\pm 1$ ), whilst zero contrast when the  $\sin\pi\chi(\alpha)$  hits zero value.

Following Rayleigh, the resolution of an optical system can be defined as follows: if the central maximum of the Airy function of one object coincides with the first subsidiary maximum of the Airy distribution of the other object then the two objects are well-resolved. Accordingly, the resolution ( $d$ ) between two adjacent point-like objects can be determined as below:

$$d_d = 1.22 \frac{\lambda}{\alpha} \quad (2.5)$$

where ( $\lambda$ ) is the wave length and ( $\alpha$ ) represents the collection semi angle. Equation (2.6) defines the diffraction limited resolution. According to the above equation,

the image resolution can be enhanced by increasing the acceleration voltage or by decreasing the aperture size. However, as discussed above in Section 2.2.3.2, the objective lens will inevitably possess some spherical (and other) aberrations, which also limit the resolution. Until the advent of aberration correction, the best resolution of HRTEM was achieved by finding a balance between spherical aberration and defocus. In 1949, Scherzer [77] suggested that the CTF can be optimised by balancing out the spherical aberration against defocusing the lens. This occurs at a particular value of defocus known as the ‘‘Scherzer defocus’’  $\Delta f_{Sch}$ :

$$\Delta f_{Sch} = -1.2(C_s\lambda)^{1/2} \quad (2.6)$$

Within this  $\Delta f_{Sch}$  defocus, all diffracted beams will have a phase shift of constant sign out to the point of the first cross-over on the spatial frequency axis. This crossover point is characterised as the point resolution limit. Because of the variation of the CTF with the spatial frequency, the transfer of information from the sample to the image will not vary with defocus and hence the image understanding is not intuitive. So, an aperture is set to select on a specified range of the spatial frequency to ease the image interpretation, namely to set the aperture at the first crossover of the CTF at Scherzer defocus. Thus, the maximal value of spatial frequency is introduced by the CTF in order to present a reliable image interpretation. This shows that the negative curve increases as the value of the  $\Delta f_{Sch}$  increases and decreases as the value of the  $\Delta f_{Sch}$  decreases as shown in figure 2.11.

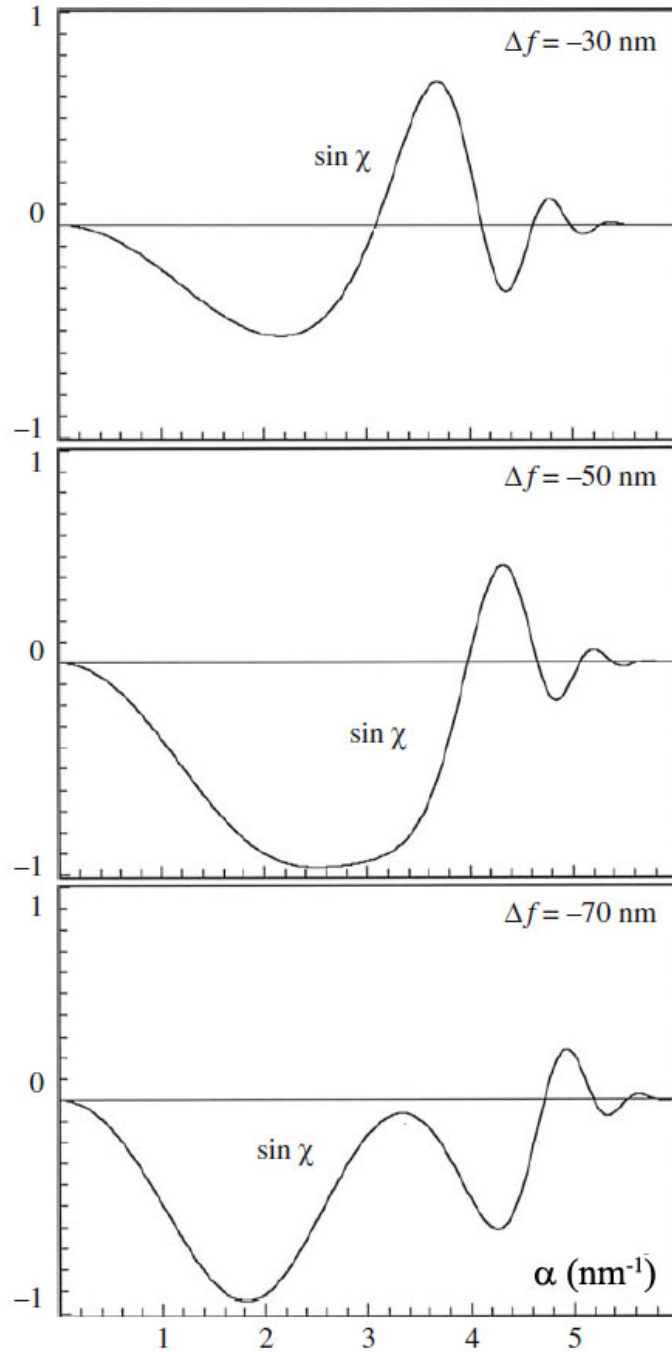


Figure 2.11: A schematic diagram of  $\sin \chi$  curves calculated for different values of  $\Delta f_{Sch}$ , at values of -30, -50 and -70, respectively.

A schematic plot of the CTF, which is proportional to  $\sin \pi \chi(\alpha)$ , versus the collection angle ( $\alpha$ ) is shown in figure 2.12. In reality, the fluctuations of  $\sin \pi \chi(\alpha)$  in the CTF function are suppressed by the lack of spatial coherence of the source  $E_s$  and by chromatic aberration  $E_t$  of the lens acting on the energy spread of the source, which in turn can be expressed by envelope functions. The result of this envelope

function is to establish a virtual aperture in the back focal plane of the objective lens in a microscopy resulting in damping of higher spatial frequencies. Ultimately, this limitation degrades the microscopy resolution and sets an information limit beyond which no significant information is transferred (with either a positive or negative phase shift).

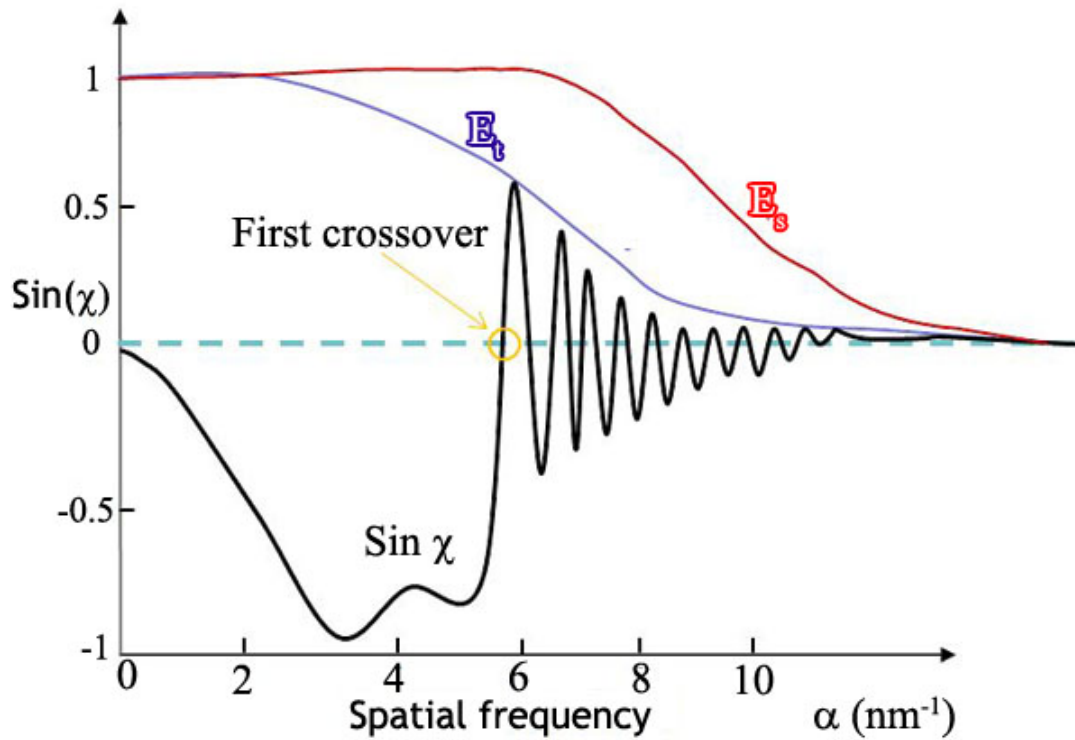


Figure 2.12: A schematic diagram of  $\sin(\chi)$  vs  $\alpha$  displaying the CTF as a function of  $\sin(\chi)$  within an uncorrected TEM. This has been calculated for the CM300 at NCEM (Berkeley, CA, USA),  $C_s = 0.6\text{mm}$  and an accelerating voltage of  $300\text{keV}$  ( $\lambda = 1.97\text{pm}$ ) result in Scherzer defocus =  $-41.25\text{nm}$ . The maximum allowable spatial frequency, which gives intuitive image understanding, is determined by the first crossover.  $E_t$  and  $E_s$  represent the chromatic aberration and the spatial coherence envelopes, respectively. In fact, the parameters for the CM300 are exactly the same as those for an uncorrected TITAN 80-300, so this graph illustrates well the performance available on one microscope used in this research prior to aberration correction.

### 2.3.2.1 The use of negative spherical aberration (NCSI)

Since spherical aberration  $C_s$  limits the resolution in both STEM and TEM instruments as mentioned in section 2.2.3.2, it is therefore NCSI that is required to

compensate the  $C_s$  of a lens. In the case where  $C_s$  is corrected to be “0” and hence  $\sin\pi\chi(\alpha)=0$ , no phase contrast is observed for the WPO. Thus, some residual  $C_s$  is needed to give phase shifts and therefore to display contrast. This could be chosen where  $C_s$  is small and positive, but there are advantages in setting  $C_s$  small and negative. Setting  $C_s$  small and negative allows a particularly simple way of producing easy to interpret images using a single image at a single defocus. This section explains how this works.

The amplitude and phase conditions of NCSI can be explained in the Gaussian complex-number plane as shown in figure 2.13. The incident wave  $V_{inc}$  is depicted by a vector parallel to the real axis while the diffracted wave,  $V_{diff}$  undergoes a  $\pi/2$  phase change and, lies along the imaginary axis. Thus, the vector sum  $V_{res}$  will be a rotated vector at a slight angle to the positive real axis, but with little difference in the amplitude resulting in almost no contrast. If a  $+\pi/2$  phase shift is added to the diffracted wave, the this now lies in the negative direction on the real axis and  $V_{res}$  is reduced significantly. Therefore, the scattering positions in the image yields a negative contrast on a bright background. This would be the contrast seen using negative defocus and positive spherical aberration, as shown in figure 2.11 above. But, when a  $-\pi/2$  phase shift is added to the diffracted wave, the resultant vector,  $V_{res}$ , is increased in length and this gives a bright contrast on a darker background for strong scatters. This can be achieved using a negative spherical aberration and a positive defocus (Jia *et. al* [71]), see figure 2.14. Figure 2.14a shows the contrast transfer function of an uncorrected microscopy where the phase CTF (PCTF) is close to 1 for a range of  $\alpha$  up to  $\alpha_s$  (the Scherzer point limit). In contrast to this, figure 2.14b shows the contrast transfer function after optimisation in the corrected microscopy to give ideal NCSI conditions where the range of the spatial frequency is taken after the limiting point  $\alpha_1$ . For an aberration-corrected conventional TEM the  $3^{rd}$  order spherical aberration is adaptable and can

include a range of values about  $\pm 20\mu\text{m}$  at 200kV. For the work performed in this thesis,  $C_s$  was tuned to  $-10\mu\text{m}$  and a defocus of about 7.2nm was used (see table 4.1 in section 4.2.3). The NCSI HRTEM images that require a  $C_s$  corrector or the objective lens were taken with 300keV along an  $[001]$  direction) at Jülich on the TITAN 80-300 performed by Dr Lei Jin (Ernst-Ruska Centre, Forschungszentrum Jülich).

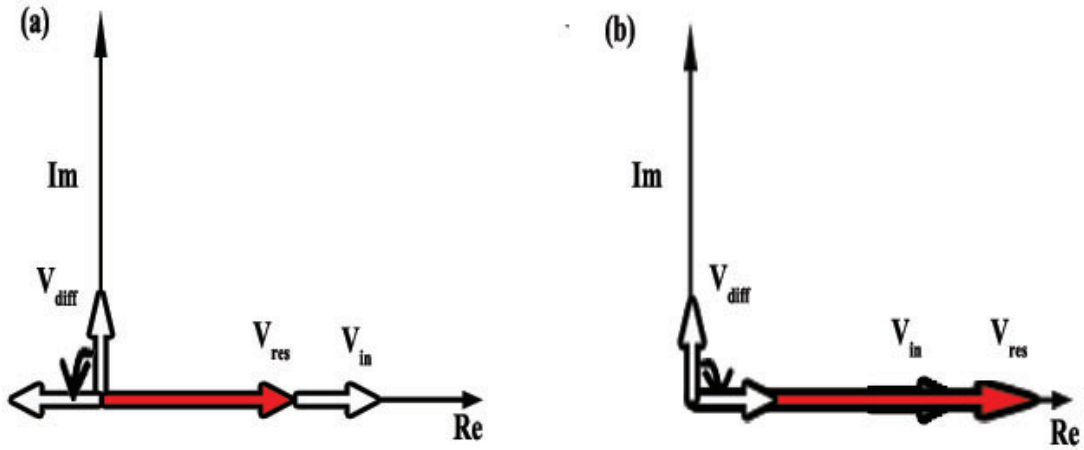


Figure 2.13: Amplitudes and phases in the Gaussian image plane illustrating phase contrast in a (WPO).  $V_{in}$  is pointing along the real axis and that of the scattered wave  $V_{diff}$  along the imaginary axis. The basic phase shift of the diffracted wave is  $+\pi/2$ . (a) For positive phase contrast, an additional  $+\pi/2$  phase shift is added to the diffracted wave, where the atom positions appear dark on a bright background. (b) For negative phase contrast, the corresponding additional phase shift is  $-\pi/2$ , where the atom positions appear bright on dark (negative) background.

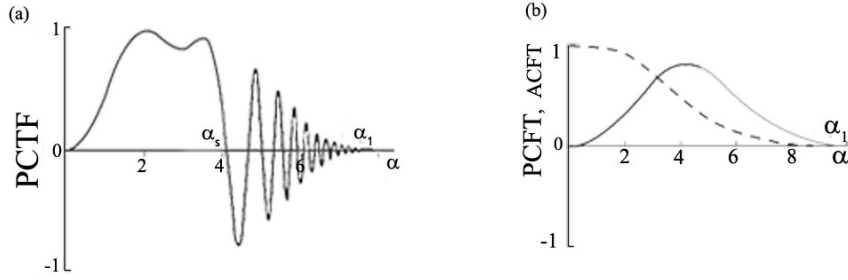


Figure 2.14: Plot of PCTF, which is the phase contrast transfer function and ACTF, which is the amplitude contrast transfer function vs spatial frequency ( $\alpha$ ). (a) A schematic plot of PCTF for an uncorrected microscopy, which is proportional to  $-\sin 2\pi\chi(\alpha)$ . (b) Plot of PCTF for NCSI conditions in the aberration corrected microscopy, which is represented by a solid line. The dashed line shows the amplitude transfer function (ACTF vs  $\cos 2\pi\chi(\alpha)$ ).

### 2.3.3 STEM Imaging mode

In a STEM instrument, a series of lenses are used to form an atomic-scale probe incident upon a thin specimen see section 2.2.1. Using such an instrument, it is possible to sample different signals and plot them as a function of probe position to form a magnified image. For example, it is possible to use a BF or an annular dark field (ADF) imaging detector, as shown in figure 2.16.

The contrast in STEM from HAADF is dominated by incoherent nuclear Rutherford-like scattering. That is, the HAADF image is referred to as a Z-contrast image because of strong dependence on atomic number  $\approx Z^n$ , where  $n < 2$  for isolated atoms, since the angle is low compared with the ideal conditions for Rutherford scattering. For atomic resolution images, HAADF provides positive contrast of bright atoms on a dark background and can be intuitively interpreted in most cases. Therefore, the contrast is more strongly mass-thickness dependent than that from BF or low to mid angle DF imaging. Examples of this are given in sections 4.2 and 5.2.

### 2.3.3.1 BF and HAADF imaging

In principle, if the scattering of a beam is elastic, the imaging operations of TEM and STEM are interchangeable. This is known as the theorem of reciprocity [88]. Accordingly, if the source of a TEM and detector of a STEM are interchanged, identical images are acquired. Thus, STEM BF images are similar to those acquired in CTEM. The contrast of the BF in STEM depends on the collection angle of the detector. For a very small collection angle, the contrast is approximately similar to HRTEM by the reciprocity principle as mentioned above. This principle can be observed in figure 2.15. This means there exists a complex relationship between contrast, sample thickness and defocus. This allows light elements to be imaged. However, image interpretation is not always easy and may require simulations.

STEM imaging can offer a unique dark field imaging called high angle annular dark field (HAADF) imaging, in which images are formed by gathering those electrons scattered to high angles approximately following Rutherford scattering [89]. The schematic diagram for detectors in STEM that are used for different imaging modes can be seen in figure 2.16. The relative positions of the detectors allow them to collect electrons scattered through different angular ranges. Inelastic scattering electrons where the concept of the thermal diffuse scattering (TDS) is introduced. This TDS results from the thermal lattice vibration, which is again approximately equivalent to the result of Rutherford scattering electrons. These effects contribute to the background of the images used in this work (see sections 4.2 and 5.5). Therefore, the background intensity of the images were subtracted (see section 3.5). These high angle scattering electrons are the result of the incoherent scattering, as proposed by Hall (1965) [90].

Over the last decade, the development of aberration-corrected STEM instruments has brought significant improvements in materials characterisation. In

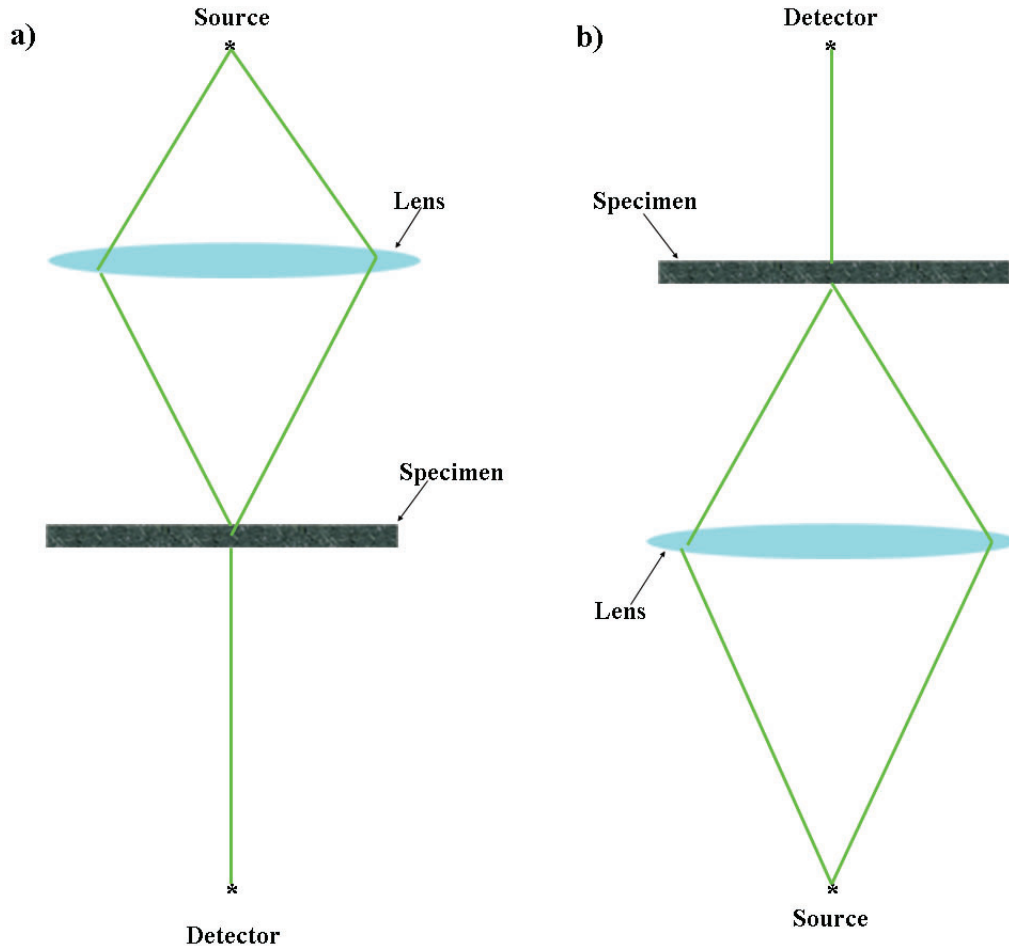


Figure 2.15: A schematic diagram of the essential elements of the electron-optical system for a) TEM and b) STEM are shown.

particular, the HAADF imaging mode has become one of the most common imaging method in STEM. This is because the HAADF imaging mode is more direct for interpreting image features than HRTEM due to the involvement of incoherent imaging, which excludes contrast reversals. In HRTEM images, the contrast can reverse due to the sample thickness or the objective-lens defocus as discussed in section 2.3.1 [91]. Image resolution has already achieved sub-angstrom levels in HAADF STEM [92, 93]. Although the HAADF technique is a very powerful one, it is only for some well-known cases that HAADF can be utilised to resolve and identify atom columns [94, 95].

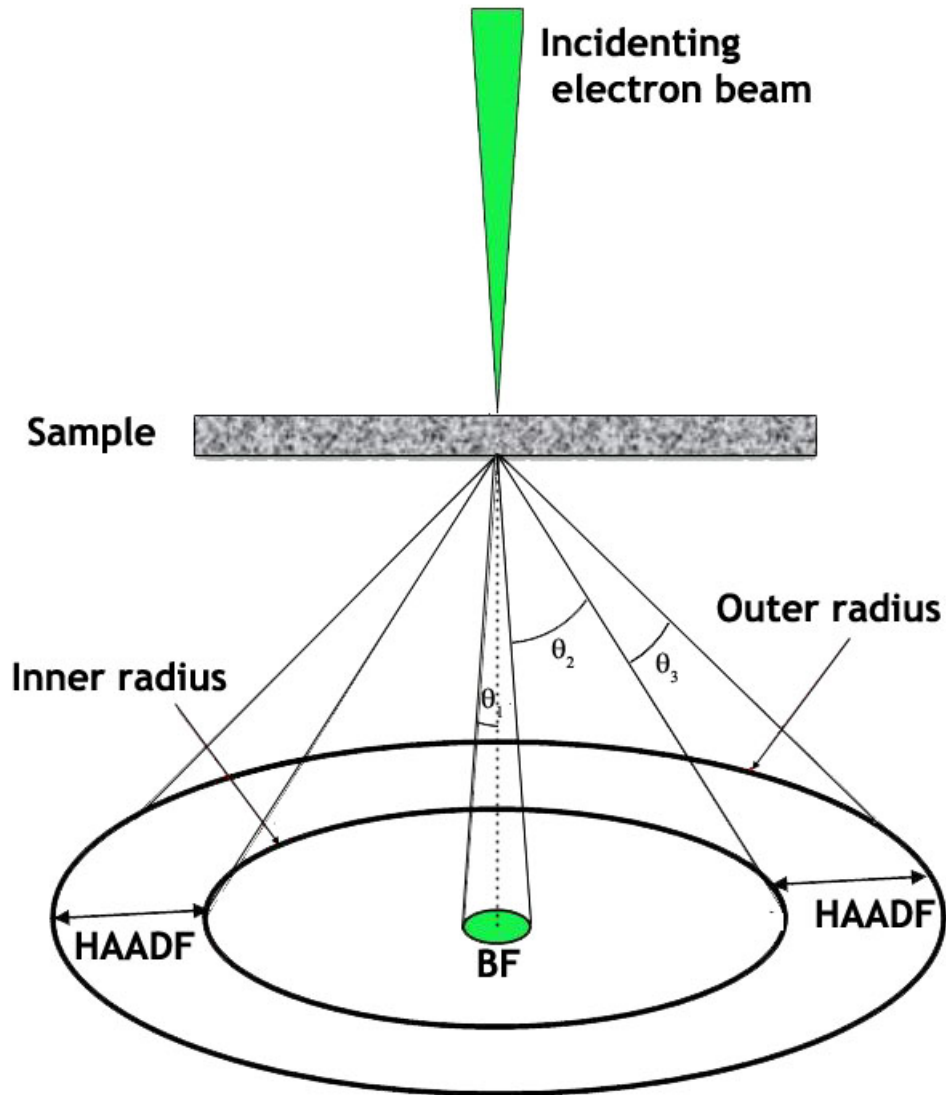


Figure 2.16: A schematic diagram showing the relative positions of multi-detectors. For BF imaging, semi-angle  $\theta_1$  is estimated to be  $< 10\text{mrad}$ , MAADF imaging  $\theta_2$  is estimated to be  $10\text{ mrad} < \theta_2 < 50\text{mrad}$ .

### 2.3.3.2 Image resolution and spherical aberration

The image resolution in STEM is limited by the probe size which is formed using the pre-specimen lenses. Generally, there are three factors that contribute to the probe formation. These are the effect of source size or the gun, the spherical aberration ( $C_s$  or  $C_{n0}$ ) and the diffraction limit. These contributions can be combined in quadrature to give:

$$d = (d_s^2 + d_d^2 + d_{sph}^2)^{1/2} = \left[ \left( \frac{4I_{probe}}{\pi^2 B \alpha^2} \right)^2 + \left( 0.61 \frac{\lambda}{\alpha} \right)^2 + (A_n C_{n0} \alpha^n)^2 \right]^{1/2} \quad (2.7)$$

where B represents the source brightness,  $\alpha$  represents the convergence of the angle, and  $\lambda$  represents the electron wave-length. The  $A_n$  coefficient is a numerical constant, namely for the 3<sup>rd</sup> ( $A_3=1/4$ ). The spherical aberration ( $C_n$ ) coefficient therefore has the form of  $C_{n0}$ . The size of the source ( $d_s$ ) for a given current  $I_{probe}$  is required to be set at a proper value where a super-fine probe size can be obtained with an optimum probe angle, namely  $\alpha_{opt}$ . So, the super-fine size of the probe is crucially determined by a given value of  $\alpha_{opt}$ . The value of  $\alpha_{opt}$  is roughly restricted to the order of 10mrad for an uncorrected microscopy due to unavoidable aberrations of the round lenses that results in a resolution  $\approx 100$  times the electron wavelength (see section 2.2.3). While for the corrected microscopy,  $\alpha_{opt}$  is increased to tens of mrad.

The optical transfer function (OTF) is defined as the Fourier transform (FT) of the STEM probe function  $FT[I(\vec{r})]$  [96]. The OTF is monotonically decaying with spatial frequencies but with doubled spatial frequency range in comparison to the CTF for the same lens parameters [97]. Accordingly, the radius of the spatial resolution of OTF for incoherent imaging is twice the radius of the CTF (see section 2.3.2) case and therefore STEM BF images are easier to interpret the images. A schematic diagram illustrating a comparison of the incoherent object transfer function and the coherent phase-contrast transfer function for the identical imaging conditions (accelerating voltage= 300kV,  $C_s= 1\text{mm}$ , and the specimen thickness= -40nm) can be seen in figure 2.17.

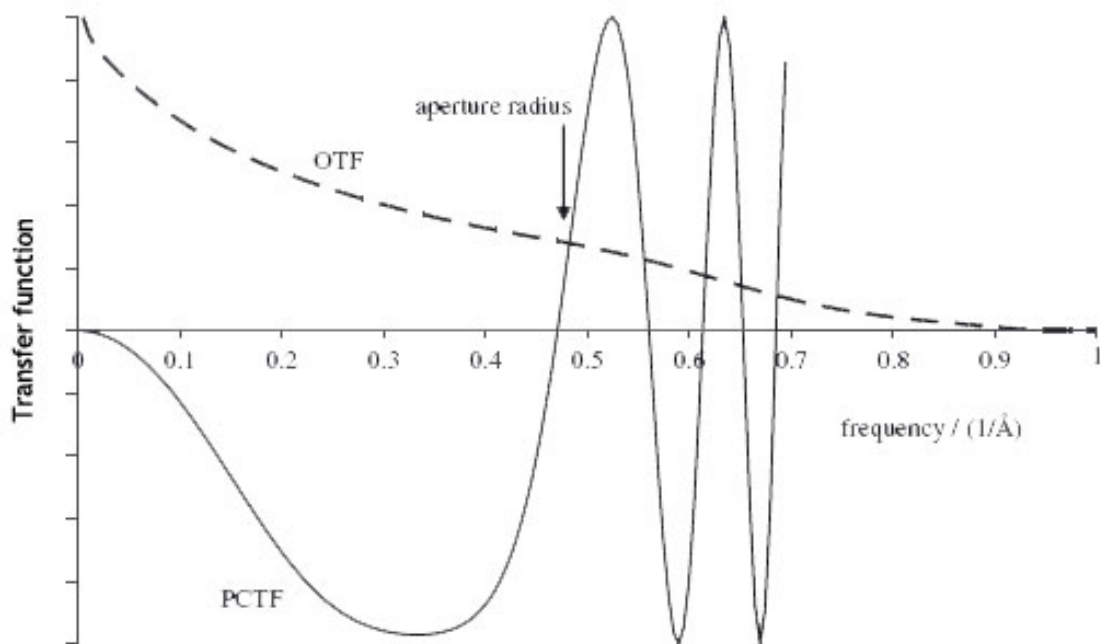


Figure 2.17: Plot showing the difference between the OTF and the PCTF for identical imaging conditions ( $V = 300\text{kV}$ ,  $C_S = 1\text{mm}$ , and  $z = -40\text{nm}$ ). The OTF can be seen to extend to twice the spatial frequency ( $1/\text{\AA}$ ) of that corresponding to the aperture radius in CTEM.

## 2.4 Electron Energy Loss Spectroscopy (EELS)

When a sample is mounted into a TEM/STEM instrument and exposed to a beam of high energy electrons, various signals are produced. The electron interactions with the sample can be described as either elastic or inelastic scattering. The elastic electron passes through the specimen almost without losing a detectable amount of energy. Whilst the inelastically scattered electrons lose energy in interactions with the sample and is hence called incoherent scattering. Some of the fundamental interactions can be seen in figure 2.18. Additionally, the two most essential processes for this work are summarised in the following sections.

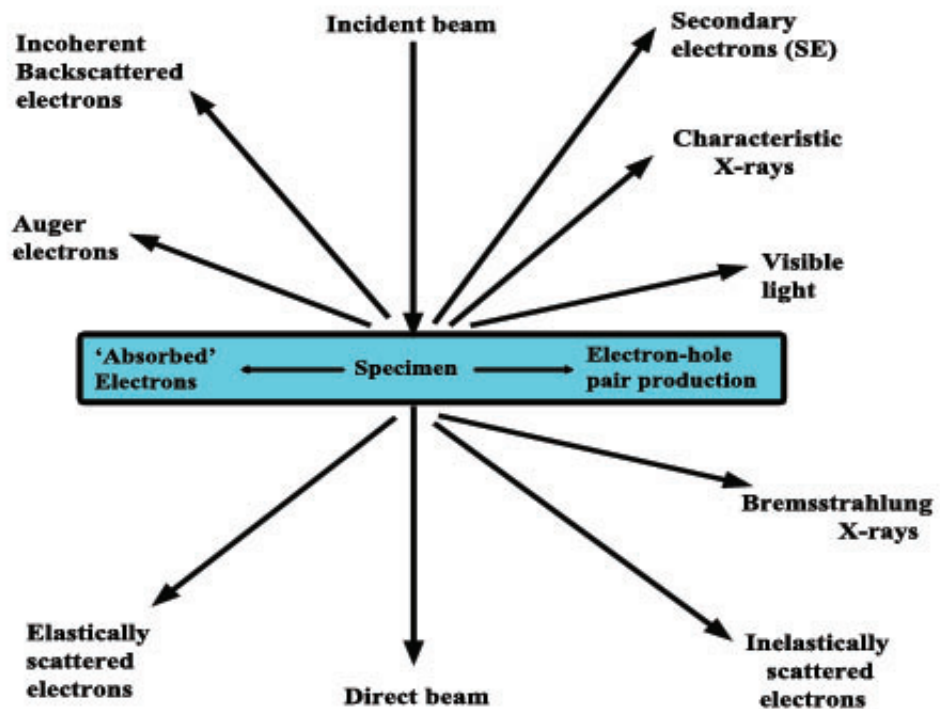


Figure 2.18: A schematic diagram showing the signals produced when a direct beam of electrons interacts with a specimen.

### 2.4.1 Elastic scattering

This kind of scattering refers to those electrons that do not loss energy after they pass through the specimen (i.e. no exchange of energy with the sample except for a small amount associated with the momentum change of the electron). This could occur in two ways: first, when electrons pass through the specimen and scatter with low angle scattering ( $1 \sim 2^\circ$ ) leading to coherent diffraction. Second, whilst electrons are passing through the specimen, they might be attracted to the positive nucleus and scattered by high angle Rutherford-like interactions leading to incoherent scattering

## 2.4.2 Inelastic scattering

In contrast to elastic scattering, electrons may lose energy after they pass through the specimen, which is referred to as inelastic scattering. Energy-loss of incident electrons may occur through various mechanisms. Some of these mechanisms are defined below:

- Emission of X-rays or Auger electrons by means of ionisation of inner-shell electrons.
- Generation of secondary electrons from the conduction or valence bands of the atoms in the specimen.
- Excitation of phonons, which are generated via electron beam interaction with lattice, and plasmons, which are produced by incident beam interaction with the outer valence electrons.
- Beam damage via exposure to the high incident electron energy may transfer some energy to the specimen through the displacing of atoms.

It is possible to collect various signals from inelastic interactions, such as X-rays or the transmitted electrons, and analyse them. These signals are termed as EDX and electron energy-loss spectroscopy (EELS). In analytical microscopy, an EEL spectrum can be generated and a variety of specimen information can be extracted such as the elemental composition, chemical bonding, and the electronic structure. The details of an EEL spectrum will be discussed in the following section.

## 2.4.3 Electron energy-loss spectroscopy (EELS)

Electron energy-loss spectroscopy (EELS) includes investigating the energy distribution of electrons after they have interacted with a specimen. Super-STEM2, which has been used in the current study, is fitted with a Gatan En-

final electron spectrometer to record the entire energy-loss spectrum in parallel at each pixel using a suitable detector. This spectrometer is attached after the post-specimen lenses (see section 2.2.1). A simple schematic diagram can be seen in figure 2.19. The main part of the spectrometer is a sector magnet or sometimes called a magnetic-sector system. This magnetic-prism presents a uniform magnetic field ( $\mathbf{B}$ ) perpendicular to the incident electron beam, which travels through a drift tube connected to the microscopy vacuum system, and are deflected by an angle of approximately  $< 90^\circ$  due to the Lorentz force (see section 2.2.3). The precise angle depends on the electron energy and thus a spectrum is formed. These electrons that enter the spectrometer can be chosen via an adjustable entrance aperture. Because the spectrometer contains a sequence of lenses, their focusing is very important to produce a sharp spectrum on the detector at the end. The lenses within can be used to vary the magnification on the camera and to correct for aberrations. The resolution of the recorded EELS spectrum is limited by various factors such as the energy width of the probe, the point spread function of the CCD, and the optics of spectrometer. The energy resolution of the spectrometer can be determined from the full width at half maximum (FWHM) of the zero loss peak in the spectrum. Finally, the resulting EELS spectrum is displayed in the image (dispersion) plane. The dispersion can be regarded as the vertical distance in a few micrometers in the spectrum between electrons of different in energy (eV). The collection angle of the spectrometer should be at least the same as the probe angle for the low loss spectrum and larger for the high loss spectrum. This is to detect electrons that have been scattered to reasonable angle.

#### **2.4.4 EELS spectra**

After exposing a specimen to electrons, the scattered electrons are detected. The way that the electrons scatter depends on the type of atoms present

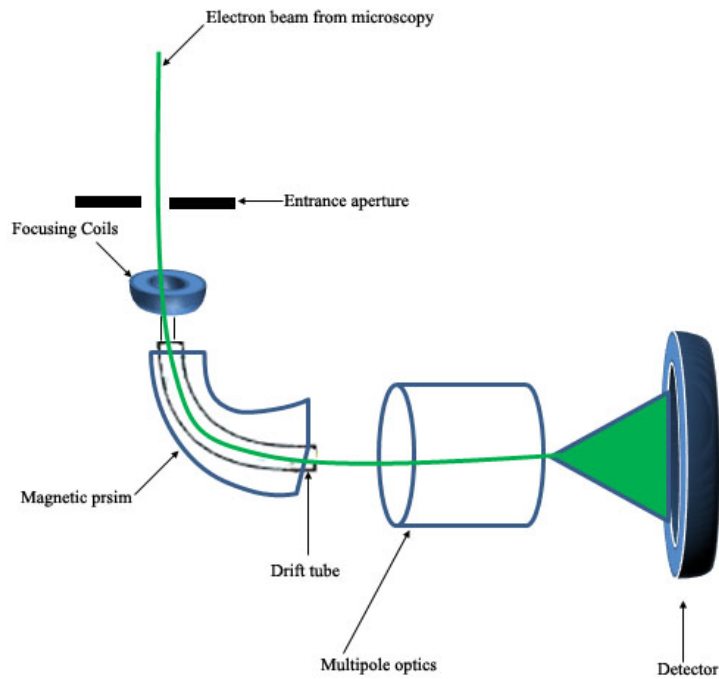


Figure 2.19: A schematic diagram of a spectrometer that is attached after the viewing screen in the microscopy.

in the sample. A typical energy-loss spectrum will be recorded via a spectrometer displaying peaks referring to electrons with and without energy-loss. The recorded spectrum can be split into three regions: the zero-loss, low-loss, and high-loss regions. These energy-loss regions are shown in figure 2.20.

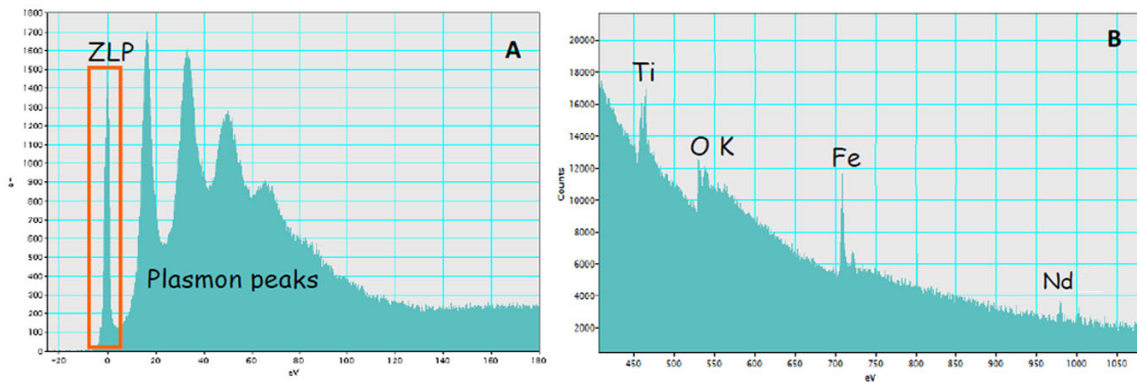


Figure 2.20: EELS showing different energy loss regions of the spectrum. A) a spectrum showing ZLP marked by an orange rectangle. The rest of the peaks are plasmons caused by multiple excitations; the plasmon peaks are rather high because the sample is very thick. B) a spectrum showing the core-loss region with the characteristic ionization edges labelled.

- Zero-loss energy region: The zero-loss peak (ZLP) involves electrons that are elastically scattered as well as the electrons that lost a negligible amount of energy. This peak has an intensity distribution determined by a combination of the spectrometer performance and the source energy width.
- Low-loss region: This low-energy region spans the range up to  $\sim 50\text{eV}$  and involves inelastic interactions with weakly bonded “outer-shell” electrons, and inter-band transitions in the specimen, among other effects. Thus, scatterings from outer electrons in the atoms of the specimen dominate this region. The log of the ratio of the intensity of the whole spectrum to the intensity of the ZLP peak is proportional to the specimen thickness [98].
- High-loss region: The high- or core-loss region is estimated to be in the range from  $> 40$  or  $50\text{eV}$  to a few thousand eV, and this region contains edges due to the inelastic excitation of inner shell electrons to empty states over the Fermi level. A particular ionisation edge energy is characteristic of a particular chemical element and is well-known for each electron shell. Therefore, ionisation-edge intensities can identify which elements exist within the sample [72].

After the edge onset, within about  $30\text{-}40\text{eV}$ , is characterized as energy-loss near-edge structure “ELNES”. ELNES depends on the vacant states above the Fermi level present for electronic transitions from this shell. The density of states depends on the bonding of the element and ELNES is therefore very useful for studying local bonding. Beyond the ELNES region, there are weaker oscillations which are known as an extended energy-loss fine structure (EXELFS), although this is rarely used in experimental studies, and is not used in this work.

In order to map the chemistry within a specimen, spectrum imaging (SI) is used. By rastering the STEM probe across the specimen, an energy loss spectrum is acquired for each pixel within the spectrum image. This method results in the

creation a four-dimensional data set of electron intensity within a 3D ( $x$ ,  $y$ ,  $E$ ) data cube [99]. However, in order to gain data with a sufficient signal to noise ratio, each pixel has to be recorded for a suitable length of time. This results in image distortion which is caused by the instabilities of the instrument which can include specimen drift, slow acquisition and electrical instabilities. These issues are considered to be inevitable but can be improved upon by considering a very short exposure, however, this is not always ideal when attempting to collect weak core loss edges. EELS is advantageous as it can provide information at atomic resolution in an aberration-corrected STEM, however spatial resolution will always be affected due to delocalisation of the Coulomb interaction between the fast electron and the initial electronic state of the atom. Additionally, as an electron beam travels through a sample, it may not follow a single atom column all the way through and may be scattered by other processes and then produce EELS interactions with other atoms in the sample (called de-channeling). This will result in the collection of an atomic resolution signal, which will also have a diffuse background due to these de-channeling effects. Atomic resolution SI is effective in identifying patterns of atomic chemical ordering in a qualitative way. It is however, difficult to make fully quantitative. This thesis concentrates on qualitative mapping at atomic resolution, and does not attempt to make the atomic resolution mapping fully quantitative.

# Chapter 3

## Computational software and data preparation methods

### 3.1 Introduction

The aim of this chapter is to introduce the different computational methods that have been utilised for quantitative analyses of atomic resolution data such as sample/stage drift correction and quantitative atomic column peak measurements. It is important to maximise the signal-to-noise (S/N) ratio of TEM and STEM images for quantitative calculations, which is achieved in STEM by correcting for stage drift. Image analysis in this context will refer to the extraction of data from an image for quantitative evaluation. Images analysed here were acquired using simultaneous bright and high angle annular dark field (BF and HAADF) imaging for STEM and a CCD camera for high-resolution transmission electron microscopy (HRTEM) using the negative  $C_s$  imaging (NCSI) technique. The material used in this study is doped Bismuth ferrite  $(\text{Bi}_{0.85}\text{Nd}_{0.15})(\text{Fe}_{0.9}\text{Ti}_{0.1})\text{O}_3$ , hereafter referred to as BFO. Two procedures have been used for stage drift correction; earlier work at Glasgow on SuperSTEM data used a simple rigid shift with summation using the

Statistically Determined Spatial Drift (SDSD) plug-in for Digital Micrograph [100], but a newly developed Smart align procedure [101] was also tested. The intensity peak positions relating to the atomic columns in the individual images were determined using a Gaussian fitting approach provided by iMtools software [102]. Beside the aforementioned drift corrections, the imported data was further processed using excel sheet to correct any remaining distortions from miscalibrations in STEM or non-orthogonality of the CCD pixel array for HRTEM. This could be due to the detector may not be mounted quite flat in the retract mount in the microscope or the optical coupling between the scintillator and the CCD may not be sliced quite normal to the fibre-optic axes. The corrected data was then used to construct the two- or three- dimensional atomic structure of the APBs. The Dr. Probe package [103] was subsequently used in collaboration with Dr Juri Barthel (Ernst-Ruska Centre, Forschungszentrum Jülich) to calculate simulated images for a variety of purposes, including determination of imaging parameters, validation of models, and investigation of effects that may affect the quantitative interpretation of images. In the present chapter, brief introductions will be given of the computational procedures that have been used to interpret the data.

## **3.2 Alignment of multiple STEM images**

As mentioned in section 3.1, in this thesis two computational codes have been used to extract information from STEM images as well as a comparison between them in terms of data enhancement. In principle, recording of images in TEM is a parallel acquisition, where the whole region of interest at once is recorded, while for STEM the recording is a series of acquisitions, where the probe is scanned over the sample point by point. Distortions can happen during the image recording process for STEM due to sample/stage drift due to a deflection of the probe beam

by external (electromagnetic) field, and due to hysteresis in the scan coils during “flyback” (this is the intentional return of the beam to the start of the next line of pixels, but if the time allowed for this is insufficient, there may be distortion at the left edge of the frame, and if there is hysteresis in the scanning coils, the flyback may not return the beam to the correct place, causing distortion of the image), [104] as well as distortions due to differences in the calibration of scan coils in the two orthogonal scan directions. Sample drift can be overcome by scanning fast and subsequently cross correlating all images and then aligning them and summing them [100]. Recently, it has been shown that the local distortions in the image can also be corrected in a stack of rapidly acquired images using non-rigid registration methods [101]. The background and theory behind using both rigid and non-rigid registration for aligning stacks of sequentially acquired STEM images. will be discussed briefly in the next section.

### **3.2.1 Simple rigid registration**

As mentioned in the section 3.2, several STEM images are recorded pixel by pixel over the region of interest. In order to do the quantitative evaluation of these HRSTEM images stacks, images are combined in order to extract accurate information and increase the S/N. The images can be combined manually if the number of STEM images is  $\leq 3$  otherwise it is time consuming and not feasible. When a number of images are combined containing the same region of interest to extract the necessary information, artifacts are inevitably introduced due to the sample drift between the consecutive exposures. STEM images were taken repeatedly and rapidly of the same area of interest, and then cross correlated, shifted, and all the images were then summed via this procedure [105, 30, 106, 66, 67, 107, 68, 108]. Figure 3.1 shows the difference between one slice of a cross-structure image and one that resulted from the summation of the image stack.

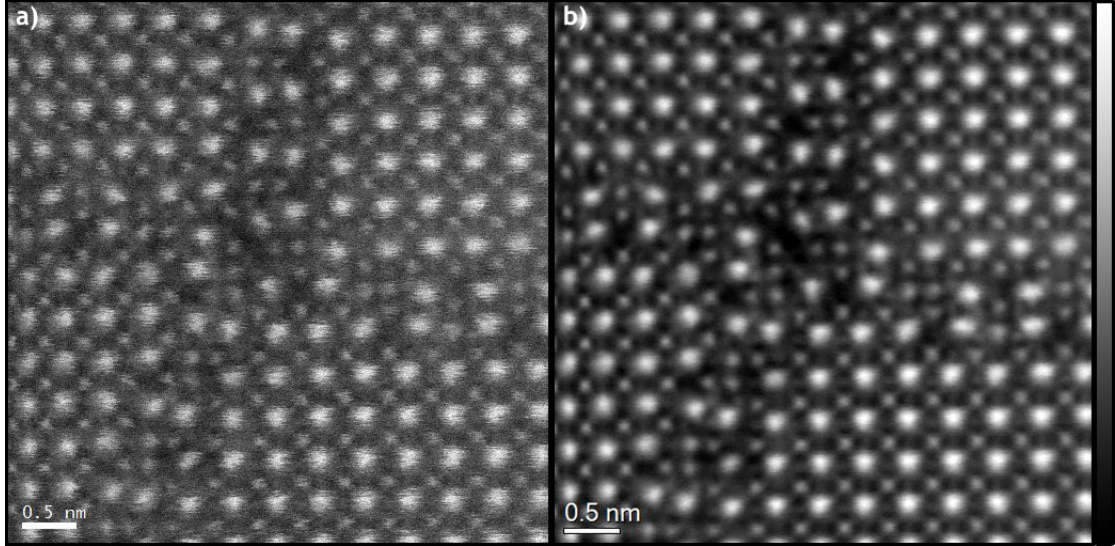


Figure 3.1: HAADF of the APB Cross structure in  $\text{BiFeO}_3$ . a) One slice of cross structure image stack b) Combined multi-images after applying spatial drift correction.

As specimen/stage drift is inevitable, the SDS code [100] in DM software was used to apply the corrections and ultimately minimize these artifacts. The SDS routine uses the cross-correlation method. In this work, we found the most robust results were achieved using the phase correlation method [109, 110]. The image registration by cross-correlation involves calculating the cross-correlation of two images including a fast-Fourier transform operation and then finding its maximum peak position. For simplicity, in the case of a “pair” of images which are shifted by an unknown amount with respect to one another, cross-correlation can be used to identify the necessary shift to correct this mismatch. Given there is a stack of images in this study, after cross-correlating each pair and statistically calculating the resulting shift vectors, the effectiveness of the algorithm for drift correction is increased. In this sense, the redundant data is excluded and this can ultimately deliver sub-pixel precision [100]. Therefore, the S/N is improved considerably as shown in figure 3.1.

### 3.2.2 Non-rigid image registration

The non-rigid image registration "Smart align" procedure has been used for this work on high angle annular dark field (HAADF) images of doped Bismuth ferrite  $(\text{Bi}_{0.85}\text{Nd}_{0.15})(\text{Fe}_{0.9}\text{Ti}_{0.1})\text{O}_3$ , (BFO), which were taken on SuperSTEM. At acquisition time, STEM images suffer not only sample/stage drift issues but also low-frequency scan distortion or line noise in scans [111]. Low-frequency sources below 100 Hz could be airflow, hollow ceiling, and even moving vehicles outside the building, while high frequency instabilities around 2 kHz could be HT tank/electron gun instabilities, electrical interference from digital systems such as building control systems and the microscope UPS, and PC fans that excite a mechanical resonance [105, 111, 112].

The sample/stage slow drifts cause uniform distortions that simply register sequentially recorded images and these distortions require corrections by so-called rigid registration (see section 3.2) [111, 113, 114]. However, faster instabilities within a frame perturb the images locally in which cause shifts of pixel information locally [111, 112, 115]. These local distortions occur on a single STEM image and it is, therefore, special image processing techniques have been developed to overcome these issues on sequences of images [112, 113, 115, 116]. In this thesis, a new package has been used for the non-rigid registration of serial microscopy dataset named "Smart align" (see section 5.2) [112, 117, 118, 119].

## 3.3 Atom column position measurements

IMtools is a package for the manipulation and quantitative processing of transmission electron microscopy images written by Dr Lothar Houben [120]. The package is based on the IDL programming language and is distributed online as

a binary code collection and graphical interface [121]. The interface of iMtools is shown in figure 3.2. Although this code has many feasible features, the code was only used to accurately determine the atom positions from atomic resolution electron microscopy images. For this purpose, the code fits two-dimensional (2D) Gaussian profiles to the peaks in the phase images. Images with minimal drift distortion were then created by alignment and summation using the SDSO plug-in for Digital Micrograph. After the phase peak positions were determined with sub-pixel accuracy [122], the corresponding data was exported to a spreadsheet for further analysis. Without applying the rigid registration procedure, further distortion incurred by imperfections in the scanning system may not be corrected. This procedure was used for comparison between HRTEM and HRSTEM (See section 4.2.2).

By contrast, the HRTEM and HRSTEM images in section 5.4 were quantitatively processed using 2D dimensional Gaussian peak fitting routine, which is part of the Image Analysis plug-in for DM provided by Dr Bernhard Schaffer (Gatan GmbH, München, Germany). This method was used because further analysis required that the fit images were subtracted from the experimental images (See section 5.2.1). Further analysis of the list of peak positions was performed using techniques similar to those in previous work [66, 67, 68] making use of Matlab for enhancing the calculation efficiency.

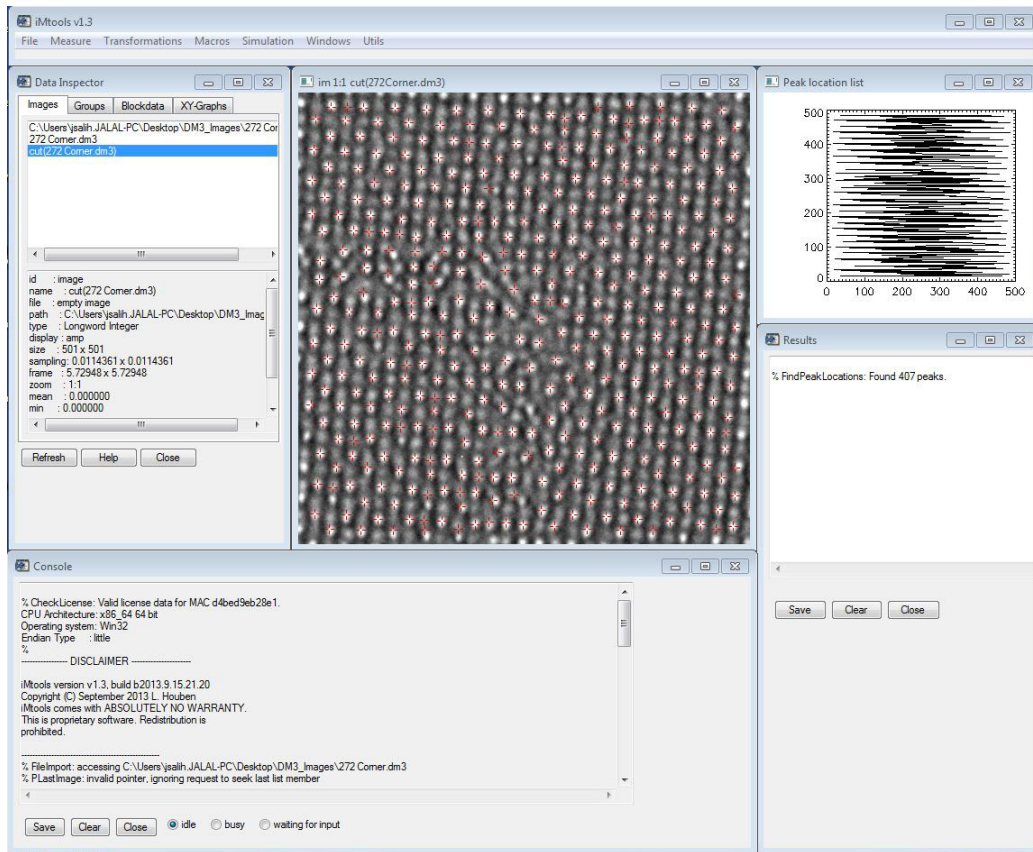


Figure 3.2: The interface of the iMtools program. The “red” crosses indicate which peaks have been identified. The peak location list is shown in the top-right corner of the interface.

### 3.4 Image simulation

Utilising high-performance atomic-resolution microscopy for the characterisation of complex materials is a difficult and multifaceted task. However, of equal importance is the ability to interpret the images. This can be achieved by comparing the experimental images with ones simulated from calculated or assumed structures. Comparison of this sort are particularly important when analysing samples where dynamic impacts have arisen [123]. The loss of resolution in an image is due to aberrations of the hardware as a sub-optimal the sample thickness and its tilt. It is, therefore, believed that image simulation is very important tool to uncover and understand the common features of an electron micrograph. The exported data from a material structure simulation forms an image, which can hence be utilised

as an input for microscopy image simulations. In this work, the data analysis was done on unique features formed in BFO and the results compared with image simulations using suggested models with experimental HRSTEM and HRSTEM images. For this purpose, a brief background of the image simulation software used will be discussed such as Multislice procedure depending on the frozen phonon method for HRTEM and HRSTEM images.

### 3.4.1 Multislice method

The multislice technique essentially depends on the electron wave, the propagation of the electron wave in free space, and the specimen. This is known as the reciprocal-space formulation. This approach divides the thick specimen into multi-thin slices with two dimensions which are oriented perpendicular to the electron propagation direction. With sufficiently thin slices, the effect of dynamical scattering can be ignored, i.e. where the electrons are scattered more than once. Accordingly, the thickness of the sliced pieces should be under the range where the change in the beam wavelength is minor, which is defined as a weak phase object (WPO) (see section 2.3.2), at the time they pass through the sample. The exit wave for each slice within a distance  $\Delta z$  is considered to be a spherical wave rather than a plane wave, which is determined as Fresnel diffraction. The incident probe wave function  $\Psi_p(\vec{x})$  in STEM at a specific position  $(\vec{x}_p)$  is determined by integrating the aberration wave function  $exp[-i\chi(\vec{k})]$  over the objective aperture

$$\psi_p(\vec{x}, \vec{x}_p) = A \int_a^{K_{max}} exp[-i\chi(\vec{k}) - 2\pi i\vec{k} \cdot (\vec{x} - \vec{x}_p)] d^2\vec{k} \quad (3.1)$$

Where  $\lambda K_{max} = \alpha_{max}$  represents the maximum angle of the objective aperture and A represents the normalization constant that equal to:

$$\int |\psi_p(\vec{x}, \vec{x}_p)|^2 d^2\vec{x} = 1 \quad (3.2)$$

As mentioned above, because the specimen is considered to be thin enough that is classed as (WPO), the incident beam faces a small deflection when it passes through the sample and thus the transmitted wave function is a simple transmission function  $t(\vec{x})$  along the optic axis. The resulting electron wave function in free space after passing through the sample is

$$\psi_t(\vec{x}, \vec{x}_p) = t(\vec{x})\psi_p(\vec{x}, \vec{x}_p) = \exp[-i\sigma\nu_z(\vec{x})]\psi_p(\vec{x}, \vec{x}_p) \quad (3.3)$$

where  $\nu_z$  represents the summation of the projected atomic potential over all the slices, which could be computed from the electron scattering amplitudes in the first Born approximation [124], and  $\sigma = 2\pi me\lambda/h^2$  is defined as the interaction parameter.

The transmitted wave function that passed through the vacuum to the next slice has a Fourier transform of the form:

$$FT[P(x, y, \Delta z)] = P(k, \Delta z) = \exp[-i\pi\lambda k^2 \Delta z] \quad (3.4)$$

Therefore, defining the transmitted wave function in real space is achieved by taking the inverse FT of the above equation:

$$P(x, y, \Delta z) = FT^{-1}[P(k, \Delta z)] = \frac{1}{i\lambda\Delta z} \exp\left[\frac{i\pi}{\lambda\Delta z}(x^2 + y^2)\right] \quad (3.5)$$

So far, for each slice in the Multislice procedure, the wave function can be regarded as two operations. Firstly, the wave function is transmitted through

a specific slice. Secondly, the wave function is propagated through free space (after transmission). Practically, the specimen is sectioned into many slices such as  $n=0,1,2,3\dots$  with a depth of  $zn$ . Thus, this procedure, essentially comprises three components: the probe wave function  $\psi_n(x, y)$ , which is considered to be at the top of each slice, the propagated wave function in the vacuum  $P_n(x, y, \Delta z_n)$ , and the transmitted wave function  $t_n(x, y)$ . This can be formulated as below:

$$\psi_{n+1}(x, y) = t_n(x, y)[P_n(x, y, \Delta z_n)] \otimes \psi_n(x, y) \quad (3.6)$$

where  $\otimes$  represents a convolution, and  $\psi_{n+1}(x, y)$  represents the wave function for  $(n+1)$  slice. Moreover, at  $n=0$  identifies the initial probe wave function in STEM  $\psi_0(x, y)$  that was introduced by Eq. (1.3).

In order to eradicate artifacts and exclude aberrations from the calculations, the spatial frequencies in the wave functions (propagation and transmission) should be limited. It is, therefore, the maximum spatial frequencies of the wave functions, which are propagation and transmission functions, that are limited to  $K_{max}=3/2$  as well as to be rotationally (cylindrically) symmetric [123, 125]. In order to show how this procedure has been computationally performed, the steps have been tabulated in table 3.1.

### 3.4.2 Frozen phonon image simulation

Since image simulation is an intrinsic tool to interpret the high resolution electron microscopy images, the frozen phonon (FPh) [127, 126] method is used widely in conventional transmission electron microscopy. This procedure is a modification of the multilice method for the inclusion of thermal diffuse scattering (TDS) effects and hence can be used to simulate and thus to interpret HAADF images [126]. This method is dubbed frozen phonon because of the interaction time of the

Step one	Segment the sample into multiple-thin slices which can be considered as WPO.
Step two	Determine the total sample potential through summing the projected atomic potential for each slice under the condition that its bandwidth is symmetrically limited.
Step three	Compute the transmission function $t_n(\vec{x}) = \exp[-i\sigma\nu_{zn}(\vec{x})]$ for each slice while limiting the bandwidth to three-quarters of its maxima to prevent aliasing.
Step four	Calculate the probe wave function using Eq. 3.1 at a given position $x_p$ .
Step five	Recursively transmit and propagate the wave function through each slice $\psi_{n+1}(x, y) = P_n(x, y, \Delta z_n) \otimes [t_n(x, y)\psi_n(x, y)]$ using FFT formalism. Repeat until the wave function is all the way through the specimen.
Step six	Fourier transform the transmitted wave function to get the wave function in the far field (diffraction plane).
Step seven	Integrate the intensity (square modulus) of the wave function in the diffraction plane including only those portions that fall on the detector. This is the signal for one point or pixel in the image.
Step eight	Repeat step 4 through step 7 for each position of the incident probe $x_p$ .

Table 3.1: Steps for the STEM image simulation of a thick sample using the multiplies method [126].

electron/atom, which is much less than the atomic vibration time in which the atom may be regarded as steady. Since there are many atoms, most of them will be displaced randomly around an equilibrium position. As a result, each electron will see different phonon configurations and then the Multislice procedure is performed to calculate images for a number ( $\sim 30$ ) of these configurations, and the resulting intensity distribution that is displayed on the detector is summed over these different configurations [128]. Finally, for all the probe positions in the addressed image, this process is repeated to build up a complete simulation of the image [128].

This method was the preferred option due to its inclusion of the effect of re-scattering effects. These effects are proportional to the thickness of the specimen and are hence quite significant when the thickness increases. Importantly, by excluding these effects one cannot expect produce an accurate result.

In reality, the specimens used are always thick enough to consider the dynamical scattering effects due to multiple electron scattering. Thus, image simulation for HAADF STEM images such as frozen phonon image simulation has to consider these effects as well as the contributions of TDS of the atoms. For the current study, one of the packages that efficiently include these two effects is considered in the next section.

### **3.4.3 Dr. Probe - High-resolution (S)TEM image simulation package**

Dr. Probe is a computer code that used in the present work, which is encoded by J. Barthel and L. Houben [103], and is available for free at “<http://www.erc.org/barthel/drprobe/>”. This (Dr. Probe) software is a package for multi-slice image simulations, which was mentioned in section 3.4.1, in transmission electron microscopy (TEM) and/or scanning transmission electron microscopy (STEM). Since

considering the elastic scattering of the primary electrons is essential for image calculations, Dr. Probe is adapted with thermal diffuse scattering (TDS) using the frozen phonon concept. The following important and significant features have been included with Dr. Probe software:

1) Projected potential slicing works not only for consistent samples (perfect crystals in zone axis) but for arbitrary samples such as periodic and non-periodic samples. This is due to an inclusion of the multislice algorithm into the code. In order to calculate the potential, the projected potential of the whole (super-cell) proposed model structure is computed on a fine grid, and hence the 3D potential is sliced and integrated within each slice.

2) Dr. Probe offers the flexibility of tilting the proposed model by only setting a desirable tilting angle or shifting the slices. This was done according to the parameters tabulated in table 4.1 (see section 4.2.3).

3) A range of atomic scattering factors is used [129] that should remain accurate even if the STEM simulation angle is high.

In the present work, the conditions for setting up the Dr. Probe program to provide a feasible compatibility with the experiment conditions were as follows:

1) The accelerating voltage set at 100kV and 300kV for CTEM and STEM, respectively.

2) The convergence angle of the probe was 30mrad.

3) The spherical aberration was considered to be  $-1\mu\text{m}$  with zero focus.

4) The detectors were set to be the same as used in the SuperSTEM experiment, which are (0-5 mrad) and (100-185 mrad) for the bright field and the high angle annular dark field detectors, respectively.

5) The specimen was sliced to multiple-thin slices in which each slice was half a

primitive unit cell with a thickness of  $1.98\text{\AA}$ , with the atoms centered in each slice.

6) The frozen phonon algorithm was utilised to provide an average of 30 phonon configurations.

7) The effect of a finite source size was simulated by convolution of the simulated images with a  $0.7\text{\AA}$  Gaussian function.

## 3.5 EELS analysis

In order to acquire artifact-free and noiseless data, and hence to quantify the results, all datasets were processed using Gatan Digital Micrograph (DM) V2.3. This will be detailed in the next section.

### 3.5.1 Quantification

Electron energy loss spectroscopy (EELS) spectrum imaging in the scanning transmission electron microscopy (STEM) was utilised to attain high-resolution information on the composition of the structure. All EELS data processing were carried out via Digital Micrograph (version 2.3) as below:

In order to get artifact-free and noiseless data from an image, a standard built-in routine in DM was used to remove the high-energy x-ray or x-ray spikes that might be induced by external radiation [130]. This was done for the whole dataset of low and high-loss spectra to achieve low-noise spectra for further processing such as such as mapping and quantification calculations.

To reduce the scale of the dataset without losing significant information, a Multivariate Statistical Analysis (MSA) [131] plug-in to DM was used to perform Principal Component Analysis and hence enhance the resulting spectra.

In order to study the concentration of an element, the following procedure is used:

- A background window is defined before the edge, a background is extrapolated, and this is subtracted from the spectrum. Moreover, the background intensity subtracted was done using a power law method in the range between 357.8 and 1109.0 eV [75] as shown in figure3.3.
- The counts within a window after the edge are row integrated.
- This integrated intensity is proportional to the elemental areal density  $N$ . The area sampled by the beam via the equation  $I = I_0 N \sigma$ , where  $I$  is the integrated intensity,  $I_0$  is the intensity in the zero loss peak, and  $\sigma$  is the interaction cross section, which is the possibility of a specific electron experiencing an energy loss due to the specific interaction which results in this absorption edge.
- Ratios of elemental concentration between two or more elements can be determined without needing to know  $I_0$  as long as the  $\sigma$  values for each element are known. Such cross sections are typically calculated using the Hartree-Slater method. In order to perform the quantitative mapping for high loss data, a spectrum fitting approach was performed in a similar manner to previous work [67, 68]. This process was carried out using a new plug-in Digital Micrograph (Elemental Quantification) routine, which was developed by Dr Paul Thomas from “Gatan Inc.”. This quantification was done by a calculation of the relative concentrations of Ti, Fe, Nd and O throughout the whole specimen.

### 3.5.2 Principal Component Analysis (PCA)

The basic aim of this method is to improve the SNR of a dataset by dimensionally reduction. This is done by discarding those components of a orthogonal factorisation which contain a low portion of variance of the entire dataset. In a sta-

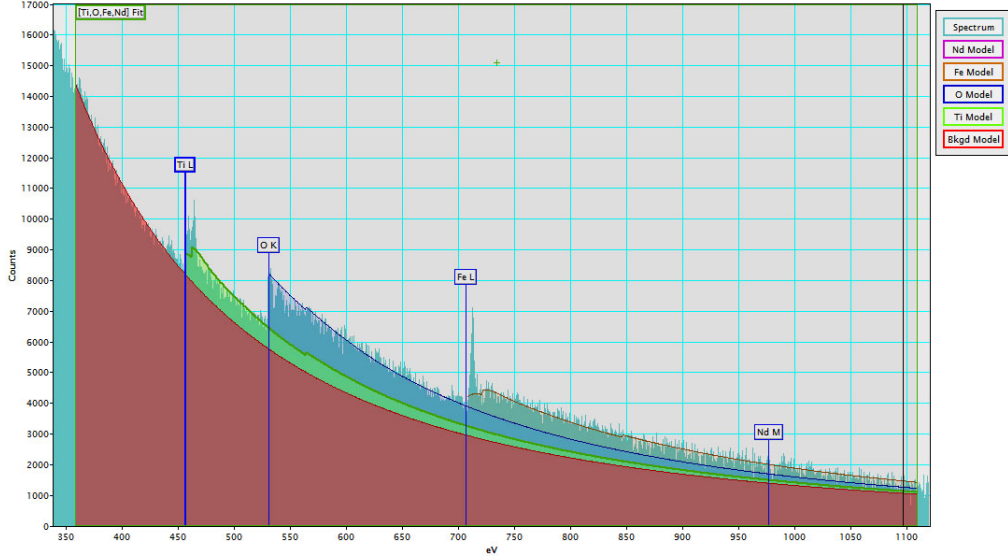


Figure 3.3: Shows the subtracted backgrounds for the whole elements.

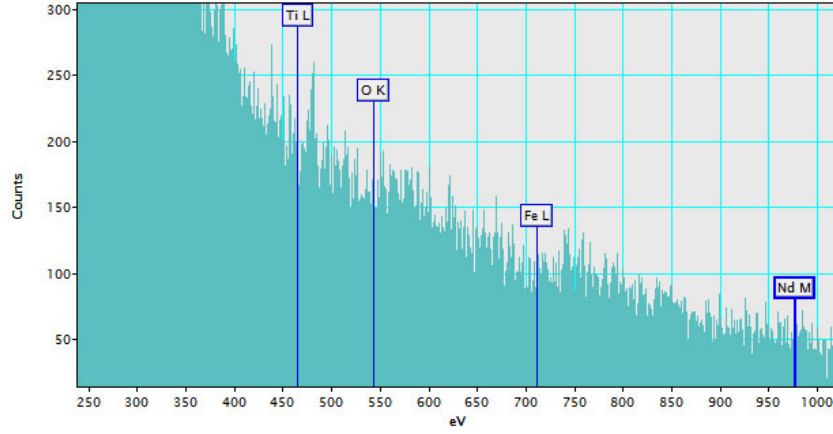
tistical manner, after applying PCA technique, random noise components will be excluded and hence the resulting spectrum is enhanced [132]. PCA was applied to the EELS-SI data using an algorithm developed by M. Watanabe *et al.* [133], through utilising the multivariate Statistical Analysis (MSA) [131] plug-in DM. Figure 3.4 shows a comparison of spectra before and after applying PCA technique, where the spiky noise signals have been removed, which are related to the random background noise, without losing significant information. In this work, the number of components were generally  $< 10$  components.

The PCA concept has been applied to a 3D EEL-SI spectrum  $\vec{D}_{(x,y,E)}$  as follows:

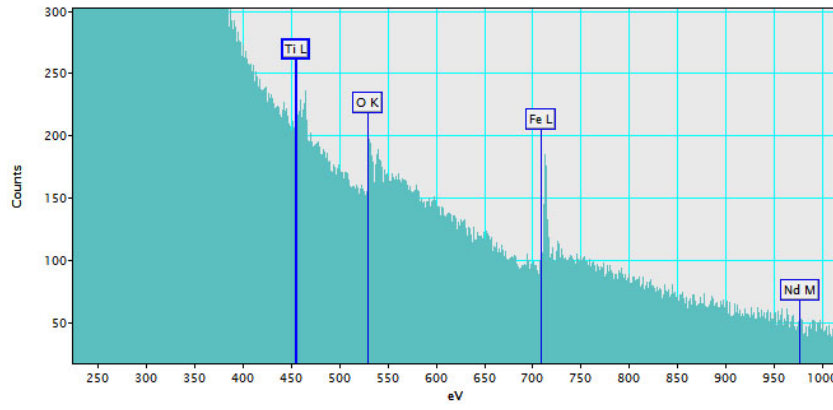
- The  $\vec{D}_{(x,y,E)}$  can be decomposed into 2D spatial data matrix  $\vec{D}_{(x,y,E)}$  as well as a one-dimensional energy data matrix (E). In terms of the PCA algorithm, the EEL-SI dataset can be formulated as follows [134]:

$$\vec{D}_{((x,y),E)} = \vec{S}_{((x,y),n)} \times \vec{L}_{(E,n)}^T \quad (3.7)$$

where  $\vec{S}_{((x,y),n)}$  is the score matrix, which covers the spatial data matrix and put in the columns of the data matrix, and  $\vec{L}_{(E,n)}^T$  the loading matrix, which



(a)



(b)

Figure 3.4: The raw spectrum a) Before PCA was applied. b) After PCA was applied.

contains the spectral information ( $E$ ) and stored in the rows; the superscript ( $T$ ) refers to a matrix transpose;  $n$  represents the number of principal components.

- Each row in the loading matrix  $\vec{L}_{(E,n)}^T$ , which represents an eigenspectrum of the data matrix, is independent or disassociated from the other rows.
- Each column in the score matrix  $\vec{S}_{((x,y),n)}$  represents the corresponding eigenspectrum in the  $\vec{L}_{(E,n)}^T$ .
- By multiplying each row of the the  $\vec{L}_{(E,n)}^T$  and its corresponding column of the  $\vec{S}_{((x,y),n)}$  individually results in a series of principal components. Mathematically, the total number of principal components ( $n$ ) is equal to the smaller

number of (x·y or E).

- In the decomposed matrix, the resulting principal components and its corresponding eigenvalues or variance are ordered from high to low level.
- Since the number of the actual features or noiseless components ( $m$ ) that contain valuable information in the data matrix is less than  $n$ , the remains or last principal components represent the experimental noise and hence the  $m$  components can be computed. Exploiting these  $m$  principal components, the original dataset can be then reconstructed. As a result, the original dataset is enhanced without losing spatial or energy resolution due to removal of the experimental noise [132, 135, 136, 137, 138]:

$$\vec{D}_{((x,y),E)} = \vec{S}_{((x,y),m)} \times \vec{L}_{(E,m)}^T \quad m \ll n \quad (3.8)$$

## 3.6 Conclusion

In the current work, both rigid and non-rigid methods have been used in order to align HRSTEM images and to remove local distortion. These methods are used in next two chapters. Additionally, two-dimensional Gaussian peak fitting through a DM Image Analysis plug-in, and iMtools were used to determine atom column positions from atomic resolution electron microscope images. In order to confirm the structures, images were simulated using the Dr. Probe multislice software package. The structures were then analysed by STEM using HAADF imaging combined with EELS-SI. These will be shown in the next chapters, 4 and 5.

# Chapter 4

## Imaging polarisation around charged antiphase boundaries

### 4.1 Introduction

As already noted in chapter 1, novel APBs were recently discovered in Nd, Ti codoped BiFeO<sub>3</sub>, and the structures of the flat terraces and steps on these structures were determined [67, 68]. The charge at these APBs is originated from counting up ions in the perovskite [108, 67, 9]. It was also shown [139, 67, 68] that they result in strong polarisation of the surrounding perovskite due to high level of negative charges in their cores. Such atomic resolution polarization quantifications have been utilized as a part of many further investigations of the nanoscale polarization distribution in a variety of perovskites utilizing both HRTEM [140] and HRSTEM [141, 142, 143, 144, 139, 67, 68]]. These negative charges are not part of any other surrounding material consequence in a perpendicular electric field. As this is in the material, this can be considered as far as a the electric displacement field ( $\mathbf{D}$ ) including commitments from both electric field and polarisation [108]. According to Gaussian law ( $\nabla \cdot \mathbf{D} = \epsilon_o \nabla \cdot \mathbf{E} + \nabla \cdot \mathbf{P} = \rho_c$ , where  $\rho_c$  is the free charge

density), the  $\mathbf{D}$ -field reduces and falls to zero as unit cells of perovskite go away from the APB boundaries. The apparent boundary conditions for solving Gaussian equation are that  $\mathbf{E}=\mathbf{D}=0$  away from the boundaries. It is therefore  $\mathbf{D}=0$  after several perovskite unit cells and thus  $\nabla \cdot \mathbf{D}$  falls to zero at the same region of perovskite unit cells. The boundary conditions accordingly compel a circumstance where  $\mathbf{E}$  and  $\nabla \cdot \mathbf{E}=0$ . This enduring drop in  $\nabla \cdot \mathbf{D}$  with distance must compare to a  $\rho_c$  relating to positive charge spreaded in this area. In a material this could be supplied by the excess of charges and in our case it would be  $\text{Ti}^{4+}$ , which requires that all the Ti are fully ionised -3 electrons/atom would be dedicated to bonding in the  $\text{TiO}_6^{-3}$  octahedra. The result of this is that a free electron is donated to the material and the normal target of these free electrons would be the excess of O atoms in the APB. This process would address a stabilized structure where APB is negatively charged and outside APB is positively charged. This could be used as an explanation for the polarisation profile that covered in the current work. In this thesis, investigations were made on the composition  $(\text{Bi}_{0.85}\text{Nd}_{0.15})(\text{Fe}_{0.9}\text{Ti}_{0.1})\text{O}_{0.3}$  using two techniques: high resolution scanning transmission electron microscopy (HRSTEM) with simultaneous dark and bright field imaging, and high resolution transmission electron microscopy (HRTEM) using the negative  $C_s$  imaging (NCSI) technique. This correlation of HRTEM and HRSTEM based polarisation measurements for the same object has not previously been undertaken and it is important to understand if the measurement technique has any effect on the results. These investigations reveals quantitative differences although similar trends in structure and polarization were found and are detailed in section 4.2. Models are proposed to interpret these discrepancies followed by calculating and visualising the electric field to support the explanation, which is detailed in section 4.2.4. Also, the effect of thickness on apparent atom positions in HRSTEM imaging is detailed in section 4.2.5. Finally, some general conclusions are drawn about the applicability of atomic resolution imaging to quantitative polarisation mapping in materials.

## 4.2 Quantification of the differences between HRTEM and HRSTEM for imaging polarisation around charged planar APBs

In the current work, two common atomic resolution imaging techniques HRTEM and HRSTEM (see sections 2.3.2.1 and 2.3.3.1, respectively) used to study the structures (see section 2.2.3.4). Apparently, in the current study, the same structures are seen in both HRTEM and HRSTEM imaging techniques and image patches then were extracted from the same region. However, the raw data for HRSTEM was previously reported by MacLaren *et al.* [67] but in the current study reanalysed and used to conduct the calculations, as detailed in next sections.

### 4.2.1 Atomic column position determination

Images of a suitable area of sample containing an antiphase boundary were taken in SuperSTEM using acquisition of several images at short pixel dwell times of  $10\mu\text{s}$  per pixel in order to minimize the drift effect on the individual images. High signal to noise images with minimal drift distortion were then carried out by alignment and summation using the SDSD plug-in for DM (Gatan Inc., Pleasanton, CA) [100]. On the other hand, images for HRTEM were taken using a Gatan Ultrascan 1000P camera from a similar antiphase boundary in an ultrathin specimen, thin enough to avoid contrast reversals.

In both HRSTEM and HRTEM imaging techniques, the atomic column positions were calculated using 2D Gaussian peak fitting using the iMtools software (see section 3.3), as in previous publications from the Jülich group, e.g. [145]. In both cases, the full list of peak positions was analysed quantitatively to correct for

any distortions through simple affine transformations similar to those done previously [146, 66, 67, 68]. This is necessary both STEM and TEM: for STEM due to deviations from calibration while for TEM due to slight defects in the manufacture and mounting of the camera. Once the images corrected, similar structural units were identified along the APBs in each image. Following this, the atom positions were determined for several structural units. These were then used to create a mean structure with calculated positional uncertainties for both the area analysed in HRSTEM and that analysed in HRTEM.

#### **4.2.2 Quantitative comparison of HRTEM and HRSTEM images of the same kind of APB**

Figure 4.1 demonstrates a comparison between negative  $C_s$  HRTEM imaging and HAADF/BF HRSTEM imaging of one of these antiphase boundaries (APBs) recorded at 300 kV on a Titan 80-300 TEM operated at 300 kV. Whilst this voltage is high, no noticeable beam damage was ever seen on the specimen. Figure 4.1a demonstrates a typical NCSI contrast, where all atoms in a structure are imaged in positive contrast (bright spots) on a dark background. However, all atoms in the structure are imaged simultaneously without any chemical information. Luckily, it was possible to recognize all atoms depending on previous published structures for the APB flat terraces [67] and APB steps [68].

Figure 4.1b demonstrates an HRSTEM overlay of BF and HAADF images, which was found in previous work to determine the O and cation peak positions, respectively [68]. On careful inspection, it is clear that the structure imaged is reasonably comparable in both cases; however the degree of similarity is examined in figure 4.2. This shows a quantitative examination of apparent atomic positions in the planar antiphase boundary (APB) structural unit from both techniques. It is

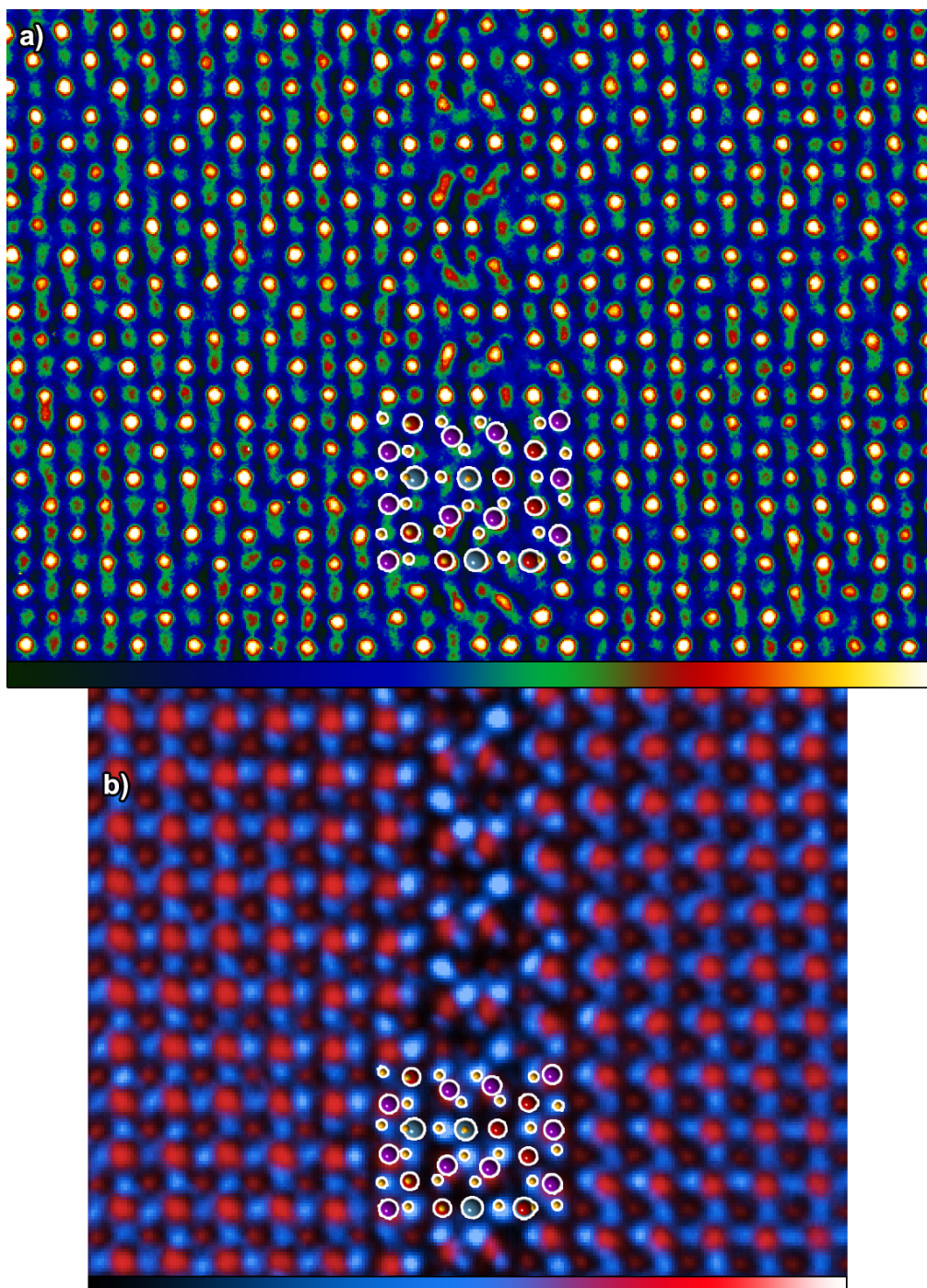


Figure 4.1: Atomic resolution images of similar antiphase boundaries in  $\text{Bi}_{0.85}\text{Nd}_{0.15}\text{Fe}_{0.9}\text{Ti}_{0.1}\text{O}_3$ : a) HRTEM NCSI image, which shows all atom columns simultaneously, and b) HAADF/BF STEM overlay image, the red shows the HAADF contrast, which mainly shows the cations, whereas the cyan shows the BF contrast, which principally shows the oxygen only columns. In both cases, atomic models of the boundary structure are overlaid to aid the reader, where purple is bismuth, red is iron, blue is titanium, and yellow is oxygen.

clear that these APBs structures are extremely alike. In spite of this, there are some definite discrepancies between the results from the two techniques. In particular, the oxygen peak positions in the quantitative measurements are consistently closer to the boundary core for the HRTEM data than for the HRSTEM data. This can be seen clearly, in particular, for oxygen atoms in the first two unit cells to either side of the antiphase boundary (APB) core which are marked by orange circles. Later, these O atoms that shifted significantly toward Bi atoms are labeled by  $O_{\perp}$ . While the O that marked by black rectangles are less shifted and hence labelled by  $O_{\parallel}$ . Any consistent pattern on cation peak positions is within the experimental uncertainty estimations and difficult to reliably measure. The O atoms differences upon the imaging mode will plainly have an effect on the determined polarization and this is shown clearly in figure 4.3. There are also some consistent deviations of oxygen and iron positions in the vertical direction across the whole image, that are probably the result of sample mistilt, and which do not influence any polarisation calculation.

This data was then used to calculate the polarisation using the standard equation 1.2 (see section 1.2.1). A reference position must be characterized in the unit cell, from which all displacements are determined. In this work, the B-site positions were assumed to be fixed in the cell and polarisation was determined on the basis of movements within a cell centred on the B-site unlike in some past work where the A-sites were used as the fixed reference (this may work better close to the boundary where the last layer of A-site atoms moves a lot.). The Born effective charges used were for  $Z_{Bi} = 6.2$ ,  $Z_{Fe} = 3.9$ ,  $Z_{O_{\parallel}} = -2.5$ , and  $Z_{O_{\perp}} = -3.4$  [29, 30, 67]. It is clear that the polarization measurement is greatly decreased in the quantification made on HRTEM images to just around 40% of that measured from HRSTEM images as shown in figure 4.3. This trend persists over the entire plot, and each data point for every case originates from averaging several atoms peak positions, so

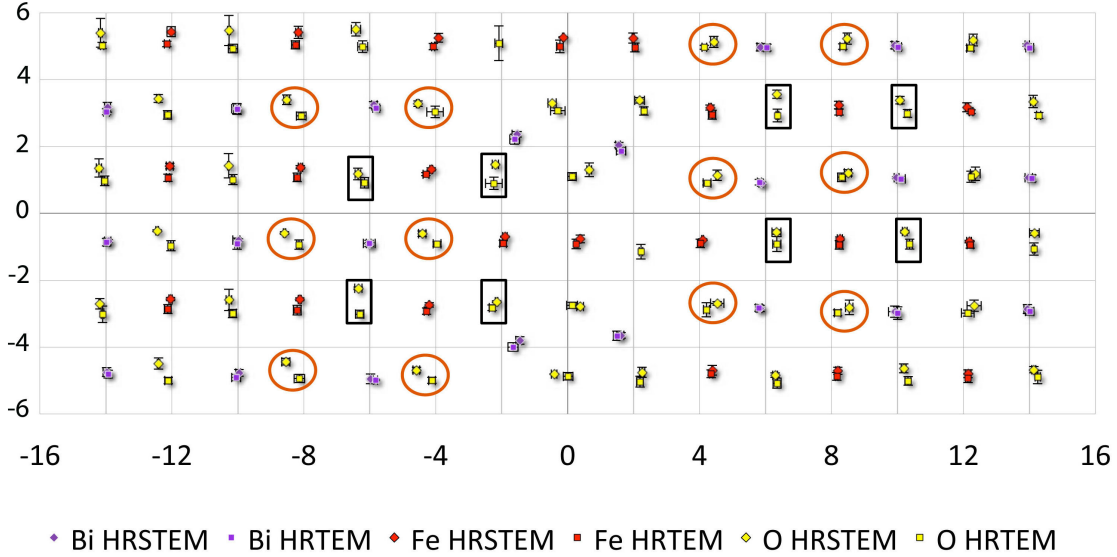


Figure 4.2: Quantitative comparisons of averaged cells for the charged antiphase boundaries (APBs) from HRTEM (negative  $C_s$  imaging) and from HRSTEM (HAADF and BF combined). This figure shows the deviation of the oxygen atoms in the out-of-plane atomic position with respect to the references in both HRSTEM and HRTEM techniques. The error bars in the two cases were calculated from the standard deviation in the out-of-plane peak position measurement after averaging for the two cases.

this outcome is reliable, even if the calculated errors on individual data points are fairly big.

It then should be asked why there is such a substantial distinction in polarization in this structure between two atomic resolution imaging methods. One thing that must be remembered, is that the specimen has very different thicknesses in the two systems. The area of interest for HRSTEM is estimated to be about 16nm thick, according to image simulations (based on matching contrast in simulated HAADF images to the experimental images) in the previous work [67]. The area examined by HRTEM is clearly much thinner than this by the lack of contrast reversals, but an exact thickness needed to be determined by simulation and image matching. In order to understand reasons for the discrepancy, the details of the sample and the imaging were considered in detail in both cases. This is discussed in more details in following sections.

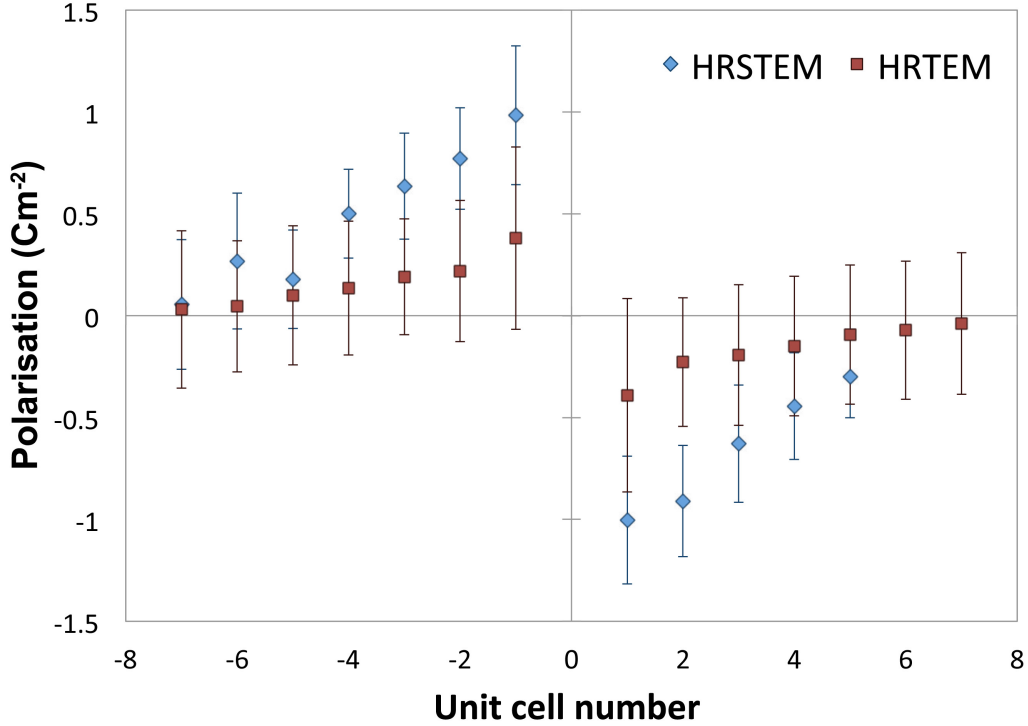


Figure 4.3: Quantitative comparison of polarisation calculations in the z-direction as a function of distance from the APB boundary for both cases. The error bars in the two cases were calculated from the standard deviation in the out-of-plane peak position measurement after averaging for the two cases.

### 4.2.3 Determining imaging parameters for HRTEM

In order to determine the thickness and microscopy parameters in the area of interest for HRTEM, HRTEM image simulations have been performed for perovskite  $\text{BiFeO}_3$  for a region of perfect perovskite crystal in the experimental HRTEM image using the Dr. Probe multi-slice imaging package for specimen thicknesses in half unit cell as mentioned in section 3.4.3 [147]. The contrast in the chosen region (marked by the yellow box in figure 4.4) is actually the highest contrast than the area in the top of the image. For comparison to simulations, an average image patch was extracted from this region containing  $2 \times 2$  perovskite units. The averaging was done over  $6 \times 6$  of these smaller patches, also removing a small image distortion based on the assumption that the Bi columns should be distributed in a square pattern.

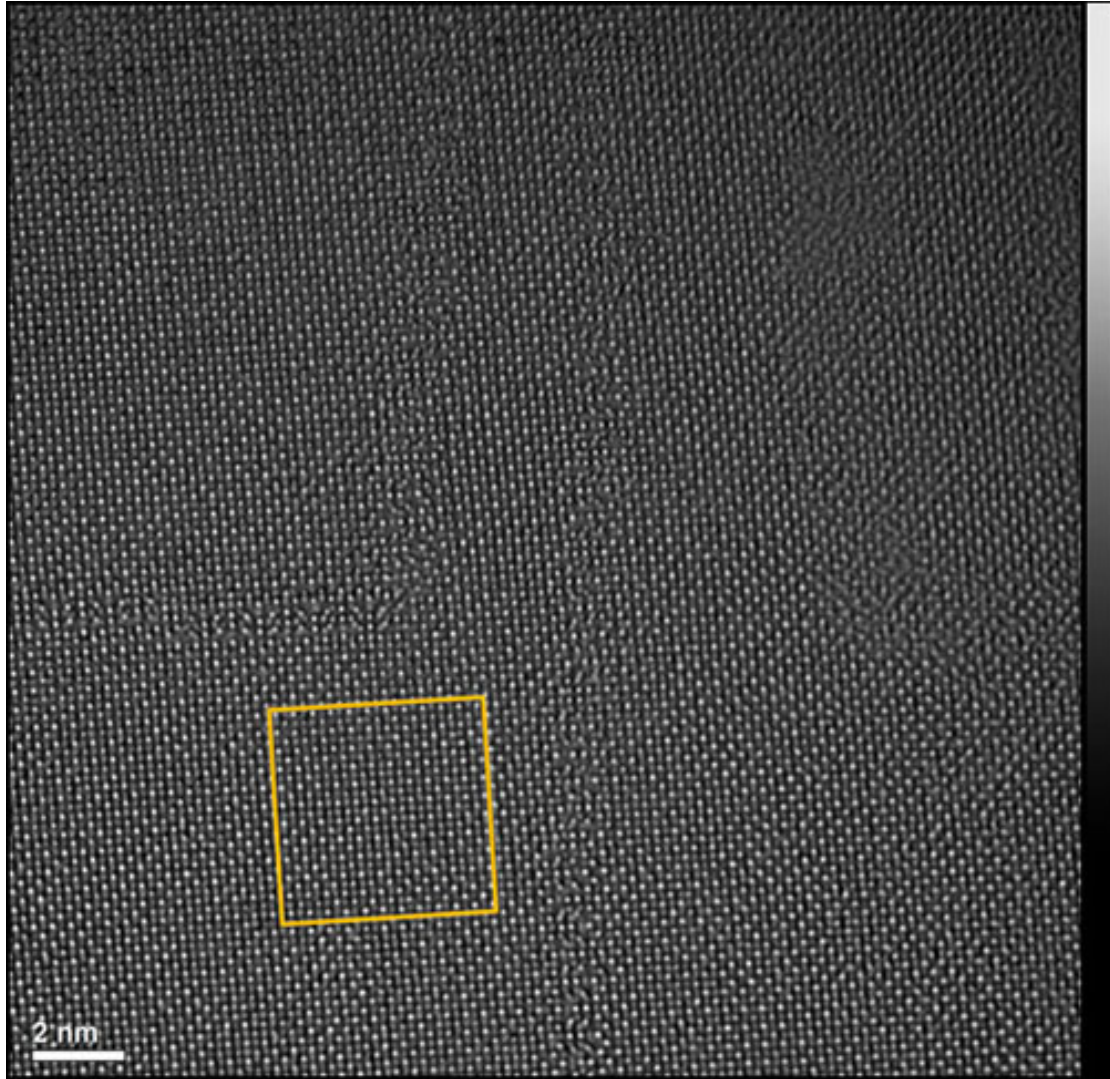


Figure 4.4: Atomic resolution images of antiphase boundaries in  $\text{Bi}_{0.85}\text{Nd}_{0.15}\text{Fe}_{0.9}\text{Ti}_{0.1}\text{O}_3$  using HRTEM NCSI image, which shows all atom columns simultaneously. The yellow box shows the area that extracted for the simulation purposes.

In order to find the best-fit simulation to the experimental image, some parameters were varied. The varying initial values included sample thickness, object tilt, relative absorption, which is a measure of incoherent absorption of inelastic contrast in the model that measured by Hashimoto *et. al* [148], defocus 2-fold astigmatism (A1) (see section 2.2.3.2), coma (B2) (see section 2.2.3.2), 3-fold astigmatism (see section 2.2.3.2), spherical aberration (see section 2.2.3.2), star aberration (S3), and vibration amplitude (rms). While electron energy, focus spread, semi convergence, and modulation transfer function (MTF), which is a measure of how well

the CCD camera reproduces the features of difference spatial frequencies), were kept constant. In a first step the object thickness was adjusted to reproduce the image contrast approximately. Then also defocus, two-fold astigmatism, absorption, and object tilt were changed iteratively maximizing the pattern correlation and minimizing the residual difference. In further iterative improvements, additional coherent and incoherent aberrations were included in the optimization of the match. The Fe and O positions were adjusted in the x-y plane in the final stage of the optimization. The final match agrees in mean value and contrast with a high pattern correlation of 0.978 and a residual difference of 0.024 (rms) and is shown in figure 4.5, which consists of the experimental image, the best fit simulation and a difference map. The residual difference image shows some small systematic and random components. The random residual differences are probably due to electron counting noise and amorphous material on top and bottom surface of the sample. The presence of the latter is for example visible in the ultrathin areas of the experimental HRTEM image in the top right of figure 4.4. Residual systematic differences may occur due to the averaging over a larger image area, where the object might change locally in thickness and z-location. Additional systematic differences may occur due to approximations made in the image calculation, such as the rather simple object structure, the neglect of surface relaxations, the use of Debye-Waller factors to simulate thermal diffuse scattering, and the applied phenomenological model of absorption. The best contrast matching was found with parameters listed in Table 4.1.

Of particular interest in the parameters determined by image matching is the sample thickness, which was just 1.6nm or 4 perovskite unit cells. The errors on the object thickness fitting are not more than 1 atomic plane i.e., 0.2nm. Changing the object thickness by 0.2nm up or down leads to a significant change of the image contrast and to a reduced pattern correlation. This is considered to be an upper

limit for the object thickness at the domain boundaries.

The fitted object structure represents the average oxygen (O-site) and iron (B-site) column centroid location relative to the Bi (A-site) columns. We observe here a vertical (the vertical direction in the image) shift of  $\sim 8\text{pm}$  in both columns against the Bi sub-lattice. The vertical shift is a consequence of a local tilt of the sample away from the  $[001]$  zone axis; such local tilts are a common difficulty in performing atomic resolution microscopy of ultra-thin samples. The best fit simulation is for a large object tilt of more than  $2^\circ$  along the vertical image direction. In the case studied in the present work, the polarisations of figure 4.3 are calculated from horizontal shifts, as shown in figure 4.2, and so these local vertical shifts (whilst also visible in figure 4.2) due to mistilt will not affect our polarisation calculations. Nevertheless, it was felt important to quantify the effects of tilt on apparent atom column positions in images, and this is performed below. However, for the bulk structure the tilt issues will be insignificant as there were almost no localised bending.

Parameter	Value
electron energy	300keV
object thickness	1.6nm
object tilt	(0, 42)mrad
relative absorption	3.3%
defocus (C1)	7.2nm
2-fold astigmatism (A1)	(2.5, 0.3)nm
coma (B2)	(15, -2)nm
3-fold astigmatism	(-40, -110)nm
spherical aberr. (C3)	-10.5 $\mu$ m
star aberration (S3)	(-1.6, 0.4) $\mu$ m
4-fold astigmatism (A3)	(-0.5, -1.0) $\mu$ m
focus-spread (1/e)	4.2nm
semi convergence	0.3mrad
vibration ampl. (rms)	22pm
MTF	as measured by Thust [149]

Table 4.1: Shows the parameters that used in simulation for HRTEM imaging.

#### 4.2.3.1 Further investigation of tilt

In order to understand the effects of local tilts on apparent atomic column positions, and thus on polarisation measurements, a further series of calculations was performed. In this case, the atomic cell used was changed to a pseudotetragonal cell, as seen in the neighbourhood of the APB (e.g. in figure 4.2), since this is more relevant to polarisation measurements than a pseudocubic cell more appropriate far from the boundary, used for the image matching of figure 4.5. The atomic parameters in the pseudotetragonal cell are listed in table 4.2. In order to show the effect of tilt, areas close to APB that were modified to present pseudo-tetragonal

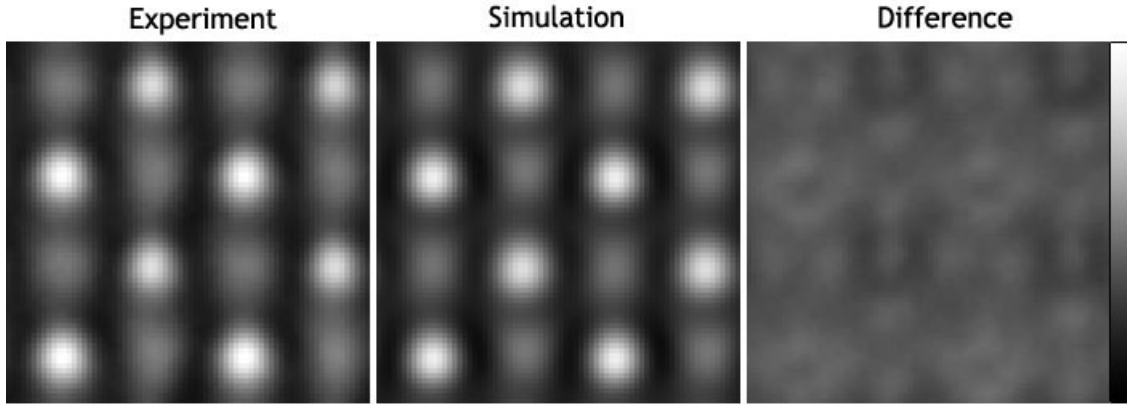


Figure 4.5: Image simulation fitting in  $\text{Bi}_{0.85}\text{Nd}_{0.15}\text{Fe}_{0.9}\text{Ti}_{0.1}\text{O}_3$  to an averaged image of perfect crystal close to the analysed region of the APB. The experimental and simulated images are on the same absolute intensity scale and agree in mean value, contrast, and have a pattern correlation of 0.98. The residual difference shown on the right has a contrast of 0.024 and contains predominantly image noise.

cells display the effect of both x and y tilts on apparent of O and Fe columns.

Symbols	Fractional coordinates			Occupancy	Biso [ $\text{nm}^2$ ]
	x	y	z		
Bi	0.00000	0.00000	0.032800	1.0	0.005
Bi	1.000000	0.00000	0.032800	1.0	0.005
Bi	0.00000	1.000000	0.032800	1.0	0.005
Bi	1.000000	1.000000	0.032800	1.0	0.005
Fe	0.500000	0.500000	0.500000	1.0	0.003
O	0.500000	0.500000	0.987700	1.0	0.008
O	0.500000	0.000000	0.450800	1.0	0.008
O	0.000000	0.500000	0.450800	1.0	0.008
O	1.000000	0.500000	0.450800	1.0	0.008
O	0.500000	1.000000	0.450800	1.0	0.008

Table 4.2: Shows the parameters that used to visualise  $2 \times 2$   $\text{BiFeO}_3$  unit cell.

Figure 4.6 shows a summary of the effects of imaging a 1.6nm thick area of a crystal with the unit cell of table 1.2 and a range of different object tilts. Figure

4.6a shows a schematic diagram of the unit cell along the [100] direction used for imaging, and the O atoms are shifted significantly to the left in this figure (i.e. the polarisation points towards the right). Bi columns, FeO columns, and  $O_{\perp}$  and  $O_{\parallel}$  columns are labelled. Figure 4.6b shows an image simulation of this structure under the electron optical conditions described (at zero tilt). Figure 4.6c then shows the shifts of atoms resulting from a range of object tilts in the x and y directions, where Bi positions in the cell are always used as the reference position. A first point to note is that  $O_{\perp}$  peak positions are shifted significantly with respect to the actual atom column positions by about 10pm to the right. This is clearly an effect of the channelling of the electrons along this column in the presence of the neighbouring Bi column (that it is shifted towards). This suggests already that an intuitive interpretation of atom positions based on the atomic resolution image is unsafe and that simulations are essential to a reliable polarisation quantification. In the present case, it suggests that our polarisation measurements from HRTEM data summarised in figure 4.2 are therefore underestimated and require correction.

As stated, figure 4.6c also shows the deviations of each column positions ( $O_{\perp}$ ,  $O_{\parallel}$ , Fe-column, and Bi) for a range (0-40mrad) of tilts of the crystal. The shifts in x and y directions are plotted against the object thicknesses. Red, green, brown and blue coloured lines represent  $O_{\perp}$ ,  $O_{\parallel}$ , FeO, and Bi atoms, respectively. When the object is tilted only through x-direction from 0mrad to 40mrad in increments of by 10mrads, no deviation is observed in the y-direction whereas significant movements of apparent column position are seen in the x-direction. In this range (0-40mrad) both oxygen columns shift to a similar degree with tilt, and the FeO column only shifts slightly less with tilt. When the object is tilted only in y-direction, the shifts are in that direction and again in increase with increasing tilt. These tilts reach a maximum of 5-7pm at a tilt of 40mrad, which is very large ( $\sim 2.3^{\circ}$ ), which while detectable, is significantly lower than those resulting from polarisation, which are

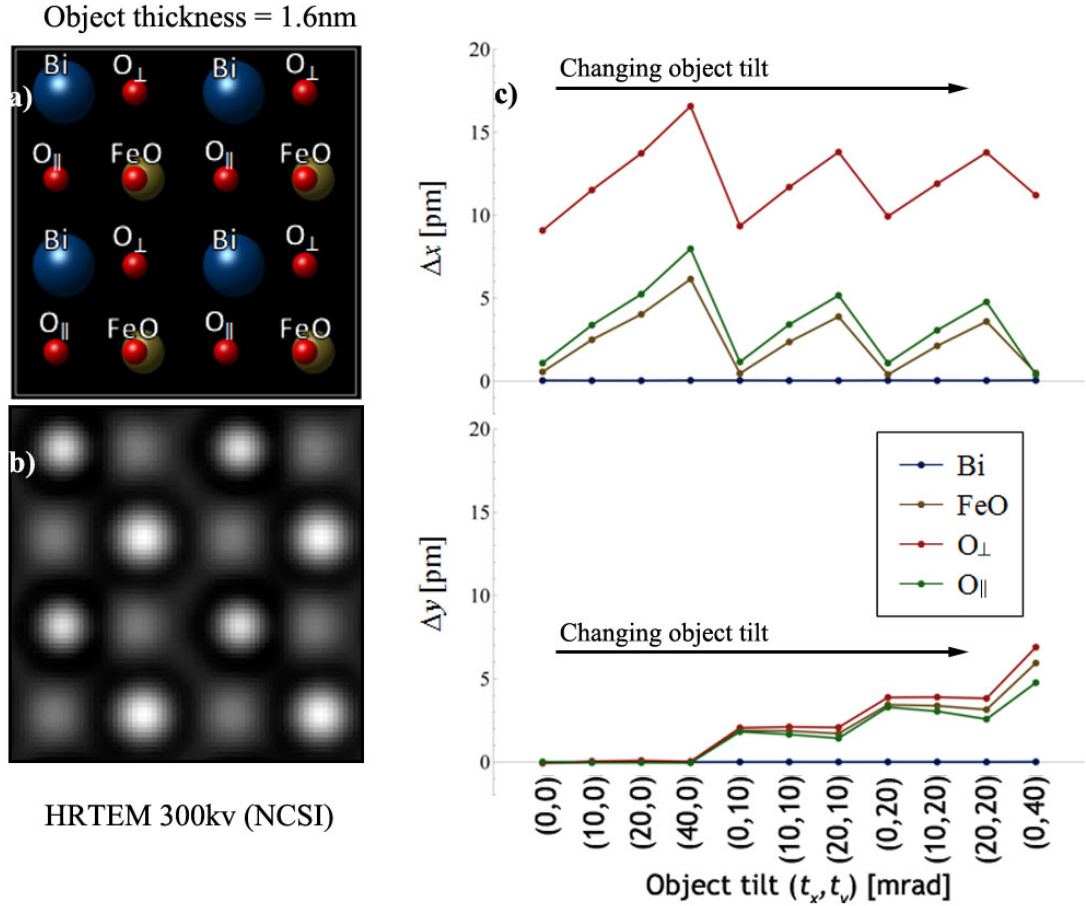


Figure 4.6: Shifting between apparent atom positions of BiFeO<sub>3</sub> structure in HRTEM images 300kV (NCSI) depending on object tilt. a) 3D visualisation where all atoms are labelled (Bi, FeO, O<sub>⊥</sub> and O<sub>∥</sub> columns). b) Image simulation from HRTEM (NCSI). c) and d) Represent apparent shifts of atom peak positions w.r.t their actual positions and the object tilts, where blue circles show fixed Bi atoms, triangles show apparent shifts of the peak positions, and where Red, green, brown and blue coloured lines represent O<sub>⊥</sub>, O<sub>∥</sub>, FeO, and Bi atoms, respectively.

typically <10pm (see section 1.2.2) [150].

As would be expected, when the HRTEM object is tilted in both x and y-direction, the deviation is observed in both x and y-direction and the shifts in the orthogonal directions are fairly well decoupled and depend on the tilt in each orthogonal direction.

It can therefore be concluded that tilt of the crystal does move atoms in a consistent direction correlated with the tilt direction, but that these shifts are small

and likely to be less than any shifts due to polarisation, except for very high tilts and very small polarisation. Additionally, the direction of the sample tilt in our case is perpendicular to the direction of polarisation, meaning that the sample tilt has no influence on the polarisation measurements. However, it is also clear from the simulations that significant shifts between apparent and actual column positions for the oxygen atoms closest to the Bi columns due to the details of channelling in the crystal, which will be of far more significance to quantitative polarisation measurements. This latter discovery makes it essential to perform simulation and image matching any time that polarisation quantification is attempted from atomic resolution TEM images.

#### **4.2.4 The effects of surfaces on HRTEM**

It has just been shown that the sample thickness for the area used in the HRTEM experiment was extremely small at 1.6nm. This may have two influences on the measured polarisation value in the images. Firstly, as shown in 1.2.3.1 above, the details of the electron channeling mean that the image of one oxygen column is significantly displaced from its actual position. Secondly, the very thickness of the sample may affect the electrostatics responsible for the polarisation, which is examined in this section.

The specimen thickness could affect the electrostatics of the charged interfaces and their surroundings in two ways. Firstly, if the specimen surface is undamaged and uncoated with conducting substance, there could be considerable stray field outside the specimen [151]. Secondly, if there are conducting layers of carbon or ion beam damaged ceramic on the specimen surface, there could be a significant reduction and reorientation of electrostatic fields near the surface of the specimen [152, 153]. Accordingly, this means that the effects of the surfaces on the surrounding material around an APB for a specimen <2nm thick will be significant.

Since dielectric properties of this material (especially the pseudotetragonal phase) are not well known, using a finite element method for simulation, which was carried out, for example, by Somodi *et al.* [152] would be very difficult. However, it is clear that the entire thickness of the object could expect to have its interior field distribution significantly influenced by the surfaces. The expectation is that the internal fields might be diminished by such boundary conditions hence resulting in the observation of polarization values that are significantly below bulk values.

In contrast to HRTEM, the sample thickness for HRSTEM studies was determined to be about  $\sim 16\text{nm}$  thick, which is much higher than the sample thickness of HRTEM. Therefore, in this case, it is expected that the surface effects are significant, and there is likely to be much larger volume of material in the core of the sample showing polarisation close to bulk values. In order to see how interpretable the obvious atomic positions are in the HRSTEM images, simulations are essential. This issue is discussed in the next section in details. To investigate the surface effects further, the electric field is calculated for simple models of both thin and thick objects and visualised to demonstrate these effects. This is discussed in the following section.

#### 4.2.4.1 Electrostatic effects of APBs

In order to address more details about the APB and hence the difference between the two samples, a model was set up, which consists of three parallel columns of point charges set next to each other in  $xy$ -plane as shown in figure 4.7. The middle column of point charges is the APB, which is denoted by  $I_3$ . The other two represent the compensating charges in the matrix, namely  $I_1$  and  $I_2$ . The electric field components for any individual point charge in  $xy$ -plane is:

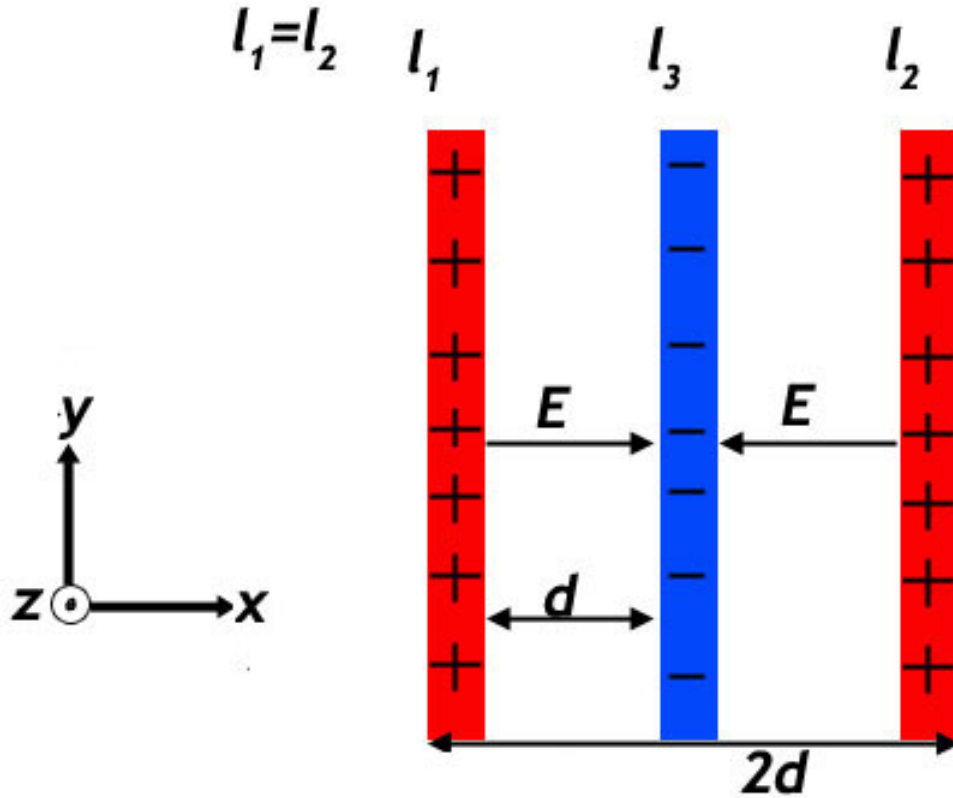


Figure 4.7: Three parallel columns of point charges which represent the APB in  $xy$ -plane and referred as  $I_1$ ,  $I_2$ , and  $I_3$ , respectively.  $E$  and  $d$  represent the electric field the distance between columns.

$$E_{xy} = \frac{kq}{r^2} \quad (4.1)$$

where  $k$ ,  $q$  and  $r$  ( $\sqrt{x^2 + y^2}$ ) are the Coulomb constant ( $8.99 \times 10^9 \text{ N.m}^2.\text{C}^{-2}$ ), the point charge, and the distance to any point in the  $xy$ -plane, respectively. Equation 4.1 has been used to visualise the vector field using a Matlab code in the next section.

#### 4.2.4.1.1 Electric field visualisation for charges in free space

A very simple model of multiple point charges fixed in free space has been visualised using Matlab using equation 4.1. At first, a simple model is assumed and described by three columns of point charges and each column, for simplicity,

has three point charges, as shown in figure 4.8. The distances between the point charges in each column is fixed and  $4\text{\AA}$  in the x direction. The distances between the columns is fixed at  $1\text{nm}$  in the y direction. It had been postulated that one reason for the low value of the polarization measured by HRTEM is that most of the electric fields go outside the specimen surface and hence reduce the field inside. Figure 4.8 shows that this is unlikely to be the sole explanation, since even for just 3 columns of point charges, the field reduction within the specimen is rather small and there is very little field rotation, even close to the surfaces. Thus, alternative explanations for the reduction of observed polarisation by electrostatic effects were considered. Specifically, the effects of conductive surfaces were considered, and this is detailed in the following section.

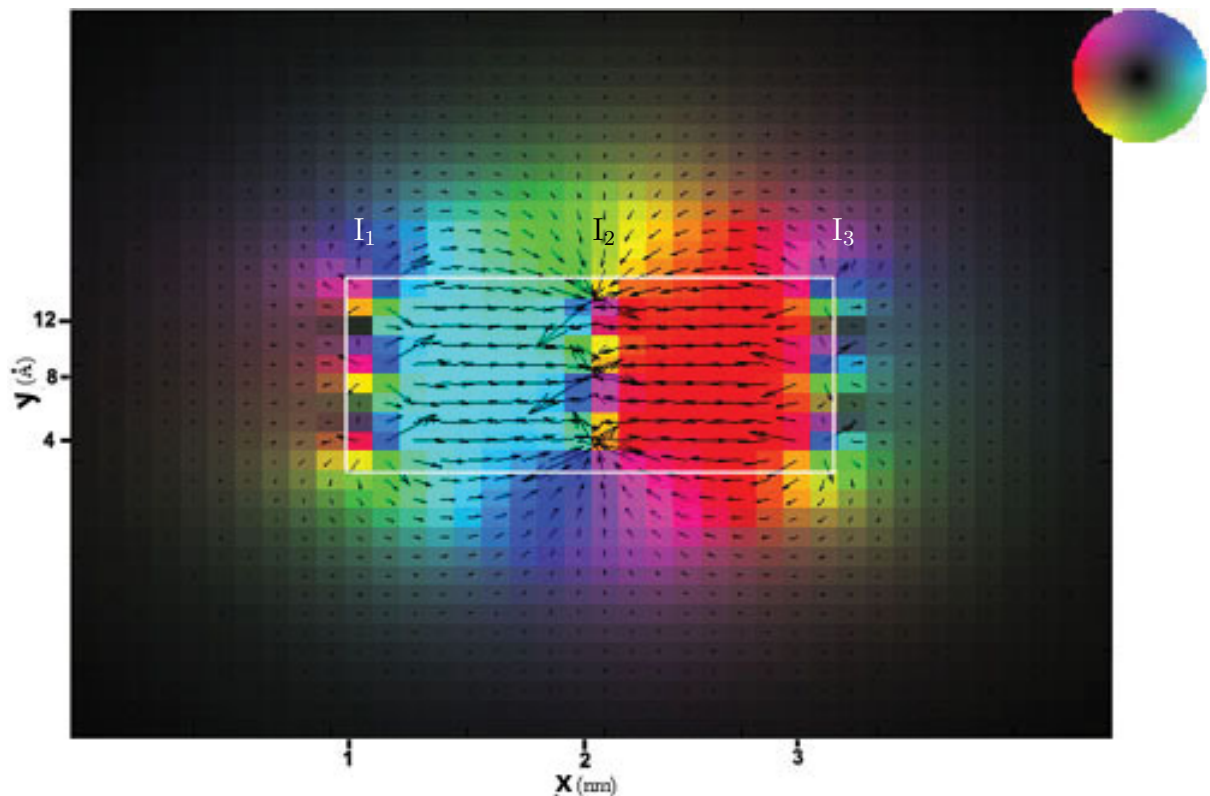


Figure 4.8:  $3 \times 3$  parallel columns of point charges which represent the APB and referred as  $I_1$ ,  $I_2$ , and  $I_3$ , respectively. Each column, for simplicity, has three point charges with fixed distance ( $4\text{\AA}$ ) in x direction, while the separation between each columns of charges is  $1\text{nm}$  in y direction. The white box refers to the specimen. The strength and the direction of the field are indicated by the color-wheel as well as by the length and the direction of the arrows.

#### 4.2.4.1.2 Modeling the effect of a conductive surface using the method of images

As mentioned previously, the depletion of polarisation at the surfaces of a thin specimen could result from the presence of a conductive surface either from surface damage and amorphisation in ion-beam preparation, or from carbon deposition. due to the effect of the coating. The effects of a conductive surface can also be calculated based on the fact that the tangential components of the electrical field distribution on the surface layer of the conductor must be zero, while the normal component is not [154]. This coating surface then behaves as if it were a mirror for the charges, and the method is commonly called the method of images. In our case, this creates three further columns of point charges as shown in figure 4.9. Note, that in the method of images, all the fields calculated above the conductive surface are not real, and only the fields calculated in the insulating dielectric are real: in actual fact, a distribution of mobile charge carriers is produced on the surface of the conductor to create this field distribution in the dielectric.

Figure 4.10 shows the visualisation of the vector field for the columns of 3x3 point charges in the xy-plane where the distances between the point charges in x-direction are set to be  $4\text{\AA}$  while the horizontal spacing (y-direction) between the columns is 2nm. The extended three columns of the point charges in x-direction are the fictitious mirror charges which flip their signs in order to calculate the effect of the conductor. Consequently, the interface layer displays a normal electric field component. This shows a significant reduction of the horizontal components of field for 1-2 unit cells. This could well explain part of the reduced polarisation seen in our HRTEM samples especially as they were only about 4 unit cells thick. The calculations of this methodology, using image charge method, show that this causes a much deeper effect of internal field reduction for ultrathin samples suitable for HRTEM. Figure 4.10b shows an increased number of point charges 8 - the same

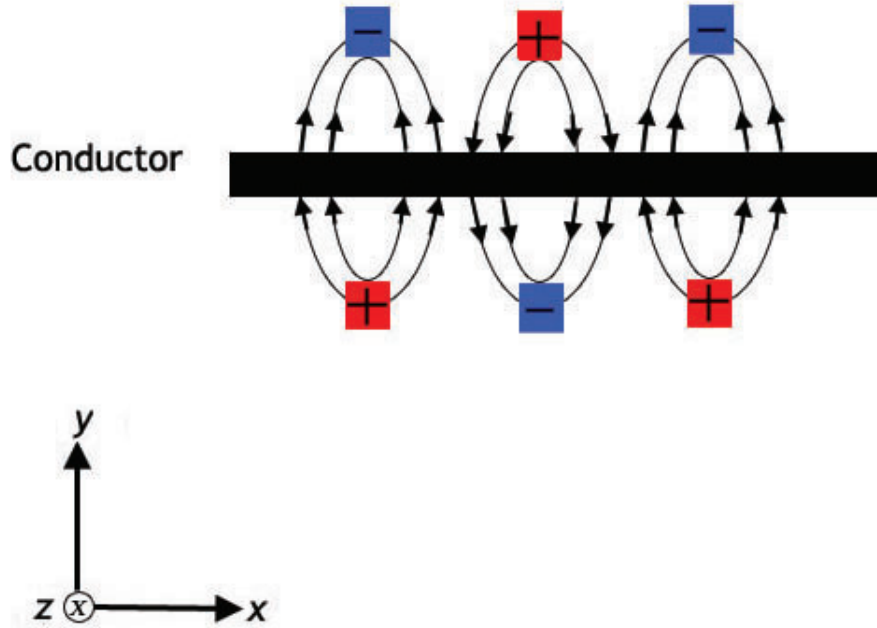


Figure 4.9: A schematic diagram illustrating the method of images for calculating the electric fields close to a conductive surface. The correct field in the insulator (below the conductor) can be generated by adding a extra set of charges mirrored in the surface of the conductor (upper charges). These are mirrored in both position and sign of the charge.

surface effect is seen, but the bulk is relatively undisturbed, and field distributions are only significantly reduced for the first 1-2 unit cells. Thus, for a thicker specimen (e.g. our HRSTEM specimen at 16nm or 80 unit cells), we do not expect a strong effect from surface cancelling out of electric field.

This work shows, therefore, that the surfaces and their electrostatic effects can have a significant influence on observations by atomic resolution electron microscopy. Unfortunately, since HRTEM requires such thin samples for some of these perovskite having a very heavy atom (such as Bi or Pb) on the A-site, the electrostatic state of the thin specimen is much different to that in the bulk specimen. As a result, direct inferences from negative  $C_s$  HRTEM imaging of ultrathin specimens about the internal structures in perovskites with ferroelectric structures could be problematic, or at least quantitatively underestimate the strength of polarisation.

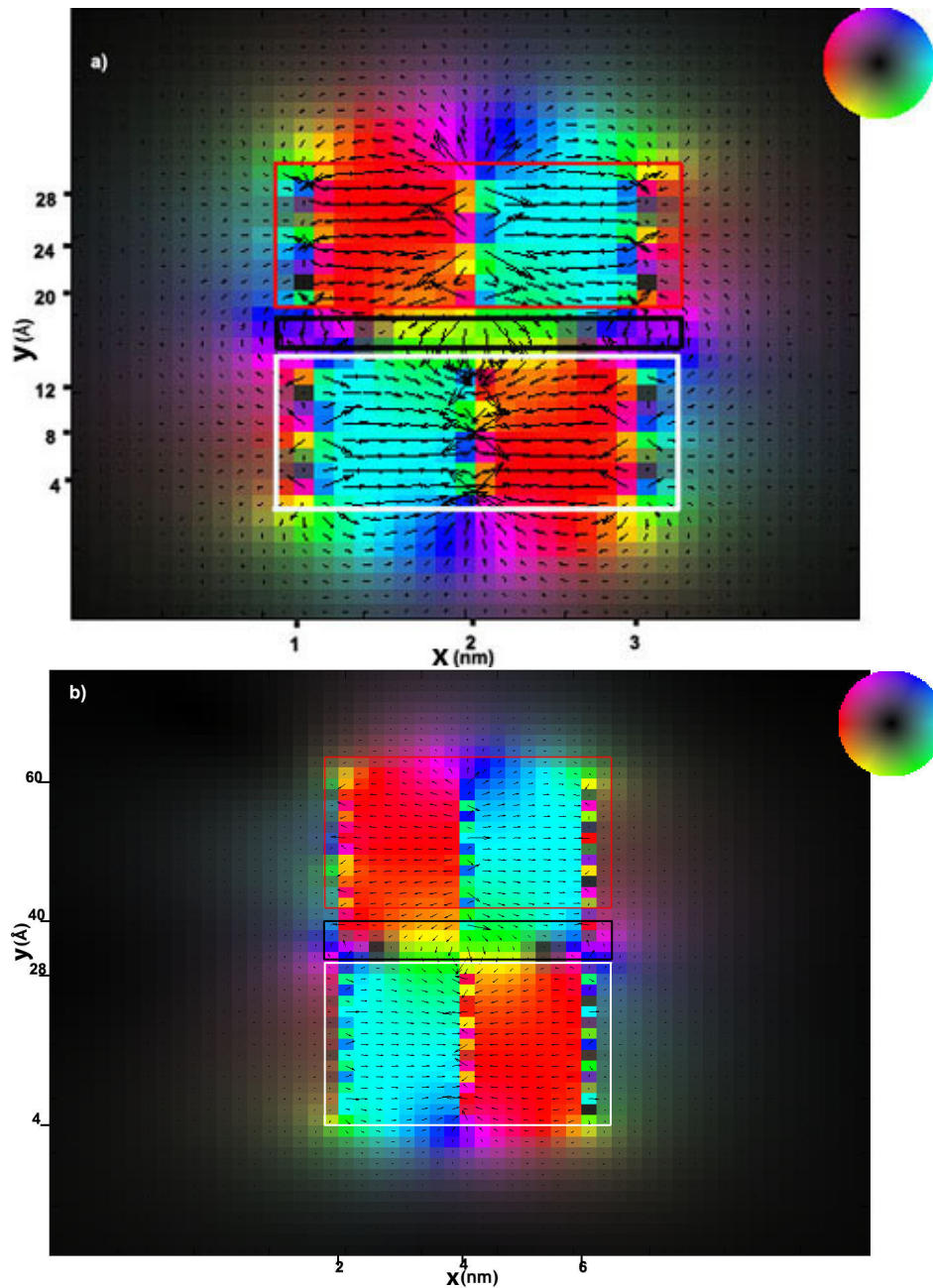


Figure 4.10: Visualisation of the field distribution calculated by the method of images for 3x3 columns of point charges a) each column contains 3 point charges and the distance between the columns is 1nm, and b) each column contains 8 point charges and the distance between the columns is 2nm in order to see more clearly. The areas that indicated by white, black and red boxes are the specimen, conductor and the image charges, respectively. Obviously, in reality, only the field distribution in the specimen (i.e. inside the white box) exists. The field is represented using colours on a colour wheel and arrows, as in figure 4.8 where the arrows represent the direction of the field.

## 4.2.5 The effect of thickness on apparent atom positions in HRSTEM

It is desirable to investigate systematically if any part of the discrepancy between HRTEM and HRSTEM is caused by some aspect of the STEM imaging or sample preparation. However, for the 16nm thickness of HRSTEM object (see section 4.2.4.1), the surface effects should be negligible at this thickness according to the electrostatic calculations above. However, the simulations for perovskite  $\text{BiFeO}_3$  of the BF imaging used to determine the oxygen positions need to be performed in order to check that this is quantitatively interpretable. For this purpose, STEM image simulation was done for 100kV incident electrons using the Dr. Probe multi-slice imaging package for specimen thicknesses in half unit cells as detailed in section 3.4.3 [147]. The illumination aperture was set to 30mrad and the probe aberrations are assumed to be sufficiently corrected. Thermal vibrations were simulated using a frozen lattice approach (see section 3.4.2). Images are calculated for a range of object thicknesses up to 25nm in steps of 0.8nm (2 perovskite layers). For detection of scattered electrons, two detectors were set up in the diffraction plane (i) a bright-field disk of 5mrad radius and (ii) an annular dark-field detector with 80mrad inner and 200mrad outer radius. The source size distribution was approximated with a Gaussian of 0.1nm FWHM and was applied to the calculated images by convolution.

Figure 4.11 shows a summary of the effects of thickness on HRSTEM imaging of a pseudotetragonal  $\text{BiFeO}_3$  crystal of a crystal with the unit cell listed in table 4.2 and a range of different sample thicknesses. Figure 4.11a shows a schematic diagram of the unit cell along the  $[100]$  direction used for imaging, and the O atoms are again shifted significantly to the left in this figure (i.e. the polarisation points towards the right). Bi columns, FeO columns, and  $\text{O}_\perp$  and  $\text{O}_\parallel$  columns are labelled. Figure 4.11b is the simulated HAADF image and figure 4.11c is the simulated BF

image for a thickness of 16nm. Figure 4.11d shows the deviation of the images of each column in the image from its actual position in the unit cell as a function of thickness.

Just as for BFO structure and HRTEM image peak positions (see section 4.2.3), figure 4.11 shows a discrepancy between the BFO-based structure and HRSTEM image intensity peak positions depending on an object thickness. In the schematic diagram of the unit cell in figure 4.11a the O atoms are shifted significantly to the left (i.e. the polarisation points towards the right). A first point to note is that, just as for HRTEM, the  $O_{\perp}$  peak positions are shifted significantly with respect to the actual atom column positions, in a way that is very sensitive to the thickness. This is clearly an effect of the channelling of the electrons along this column in the presence of the neighbouring Bi column (that it is shifted towards). This suggests already that an intuitive interpretation of atom positions based on the atomic resolution image is unsafe and that simulations are essential to a reliable polarisation quantification. In the present case, it suggests that our polarisation measurements from HRSTEM data summarised in figure 1:2 are therefore underestimated and require correction.

As stated, 4.11c also shows the deviations of each column positions ( $O_{\perp}$ ,  $O_{\parallel}$ , Fe-column, and Bi) for a range (4.5-25nm) of thicknesses of the crystal. The shifts in x and y directions are plotted against the object thicknesses. Red, green, brown and blue coloured lines represent  $O_{\perp}$ ,  $O_{\parallel}$ , FeO, and Bi atoms, respectively. When the thickness of HRSTEM object is increased through the whole range, no significant shifts for all peak positions are observed in the y-direction and always are  $<1.5\text{pm}$ . However, the shift is strong in the  $\pm x$ -direction. So, that is why the whole discussion is focused on the shift in the x-direction. For the thickness  $<5\text{nm}$ , the shift is mostly observed in  $O_{\perp}$  than the FeO and  $O_{\parallel}$  and the shifts are  $+9\text{pm}$ ,  $-3\text{pm}$  and  $1\text{pm}$ , respectively. When the thickness is  $>5\text{nm}$  and  $<9\text{nm}$ , the shifts for

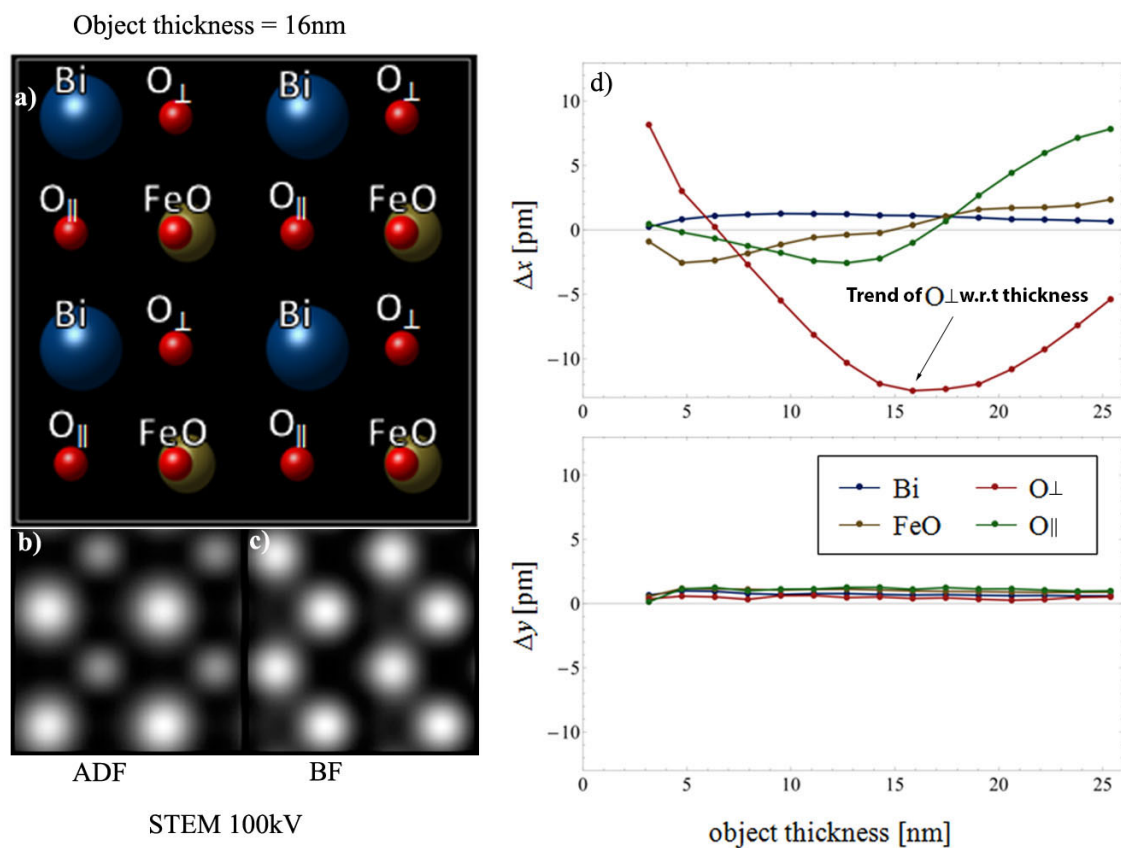


Figure 4.11: Deviation between  $\text{BiFeO}_3$  structure and HRSTEM image intensity peak positions depending on object tilt. a) 3D visualisation where all atoms are labelled (Bi, FeO,  $\text{O}_\perp$  and  $\text{O}_\parallel$  columns). b) and c) Image simulations from ADF and DF-HRSTEM 100kV, respectively. d) Represent apparent shifts of atom peak positions w.r.t their actual positions and the object thicknesses where Red, green, brown and blue coloured lines represent  $\text{O}_\perp$ ,  $\text{O}_\parallel$ , FeO, and Bi atoms, respectively.

all peak positions are in the range of -2pm to 2pm, but the shift for  $\text{O}_\perp$  atoms is still higher than the rest peak positions. Increasing the thickness starting from 9nm to 15nm, the  $\text{O}_\perp$  and  $\text{O}_\parallel$  atom are shifted more while for the FeO columns are shifted less and the values are -13pm, -3pm, and <-1pm, respectively. Further increasing the thickness after 15nm and up to <18nm, the shift is decreased for all peak positions and recorded to be <-13pm, <1pm. After that, increasing the thickness up to 25nm, the  $\text{O}_\perp$  peak position shift is significantly reduced to around -5pm, while the deviations for  $\text{O}_\parallel$  and FeO is recorded to be +8pm and 3pm, respectively. So, obviously the most peak position that significantly shifted is for the  $\text{O}_\perp$  column in

the  $\pm x$ -direction. According the thickness of the object that used in the current study, which is 16nm, the  $O_{\perp}$  peak positions are mostly deviated toward Bi (A-site) columns.

From simulation results, it was found that the  $O_{\perp}$  atoms closest to the Bi atom in a tetragonal  $\text{BiFeO}_3$  structure with O shifts of  $\sim 20\text{pm}$  off-center. Meanwhile, for the BF image the O atom was  $\sim 12\text{pm}$  closer to the Bi atom than it ought to be for the thicknesses expected in our example as shown in figure 4.12. Figure 4.12c that the channeling of electrons along the O atom column is significantly influenced by the nearby Bi column and that the channelling is pulled off-column slightly. The result is that a 32pm shift would be measured when a 20pm shift is realistic. Therefore, the polarization will be overestimated because of this specific O atom. Including the conclusion that the measured  $O_{\perp}$  shift from the image is reduced by about 40% after compensating for this channelling effect, then this reduces the peak polarisation calculated from the STEM images to  $\sim 0.75\text{Cm}^{-2}$ .

The above discussion may explain a discrepancy seen in the previous paper by MacLaren *et al.* [67], which was not completely clarified [108]. It was thought that the process of vanishing the polarisation is due to the screening occurred of the electric field and strain. However, according to electrostatics, the displacement field, in a dielectric material, can be defined as the displacement effects of an electric field on the charges such as polarisation charges. Thus,  $D = P + \epsilon_0 E$ , where P is the polarisation,  $\epsilon_0$  is the vacuum permittivity, and E is the electric field [108]. It is therefore D will definitely balance the excess negative charge with areal density,  $\sigma$ , and thus  $\sigma = P_{max}$ . Accordingly, the estimations of  $\sigma$  via atom counting that calculated previously suggested  $\sigma = 0.68\text{Cm}^{-2}$  [67], which is far from the peak polarisation estimated at  $1\text{Cm}^{-2}$ . In view of the current suggestion, if the polarisation is recalculated with a 40% (see figure 4.3) reduced  $O_{\perp}$  shift, then the new value of  $0.75\text{Cm}^{-2}$  is in much closer agreement with the expectations from atom counting.

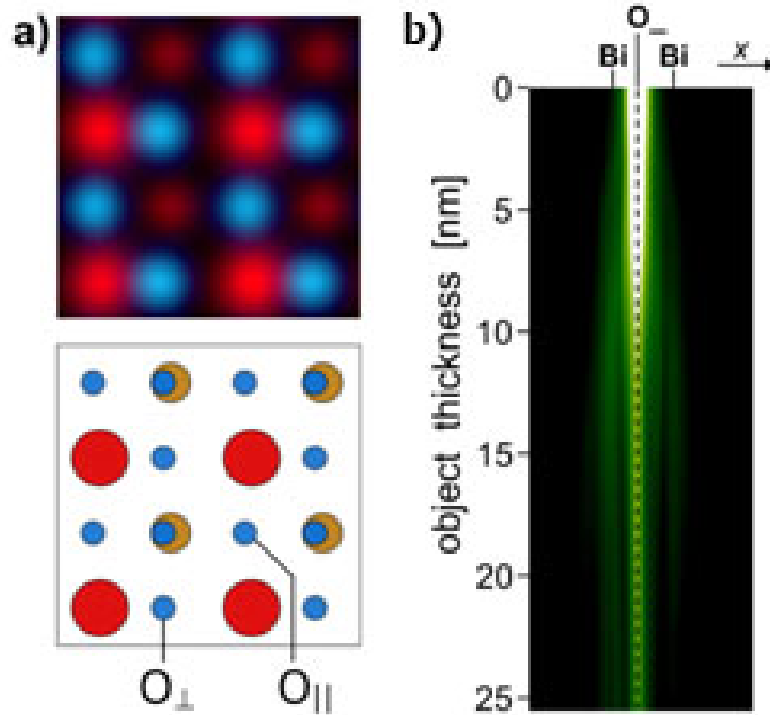


Figure 4.12: Apparent shifts of O columns in polarised BiFeO<sub>3</sub> structure as a function of sample thickness in HRSTEM. a) 3D visualisation of atoms in BiFeO<sub>3</sub> structure, red for Bi, brown for Fe, and blue for both O<sub>∥</sub> and O<sub>⊥</sub> columns. b) Deviation of O columns through the whole object thickness toward Bi columns.

### 4.3 The reliability of polarisation calculations from atomic resolution imaging in the electron microscopy

According to the above discussion, both atomic-resolution imaging techniques display quantifiable discrepancies with bulk structures in the samples under investigation for different reasons. For the HRTEM imaging technique, which requires ultra thin sample when containing a very heavy atom, for example Bi or Pb, on the A-site, then two problems can occur. Firstly, electron channelling effects can cause the oxygen columns to appear in the image with slight shifts from their real positions. Secondly, the sample is so thin that the electrostatics is strongly

affected by the surfaces, especially if they are conductive. Previous studies such as those of Farooq *et al.* [86, 87] have shown that measurements using EBSD, which is very surface sensitive, gave a reduced  $c/a$  ratio for PZT compared to X-ray diffraction or electron diffraction from thicker samples ( $>100\text{nm}$ ). Also, potential profiles calculated from the electron holography of p-n junctions are qualitatively sensible, but quantitatively too small because of surface effects [151]. Both effects act to reduce the apparent polarisation in the case studied, resulting in rather low values of polarisation measured from NCSI in HRTEM. On the other hand, for the case of HRSTEM of thicker samples, the details of the channelling within the sample can result in the apparent displacement of O columns close to heavy (Bi) atom columns from their actual positions *towards* the heavy Bi atoms resulting in a significant overestimate of polarisation.

In the light of the calculations above showing significant oxygen column displacements in the images for HRSTEM and HRTEM, the calculations in section 4.2.2 have been re-visited and polarisation was recalculated to hopefully compensate for these effects, as shown in figure 4.13. This results in an increase of estimated polarisation from HRTEM while this results in a decrease of estimated polarisation from HRSTEM. There is still a discrepancy, probably due to surface effects in HRTEM as discussed in section 4.2.2, but both are much closer to the expected peak polarisation of  $0.67\text{Cm}^{-2}$ .

In other work, attempts have been made to quantitatively measure displacements from atomic resolution images, and it has been found that sample tilts have to be very carefully controlled and accounted for, a conclusion also shown in this work. Recently, for example, Zhou *et al.* [155] have shown that apparent atomic positions can be strongly influenced by sample tilt, especially for annular bright field (ABF) imaging. Fortunately, the mirror symmetry of the polarisation across the charged AB made it possible to check for any mistilt in data and to choose

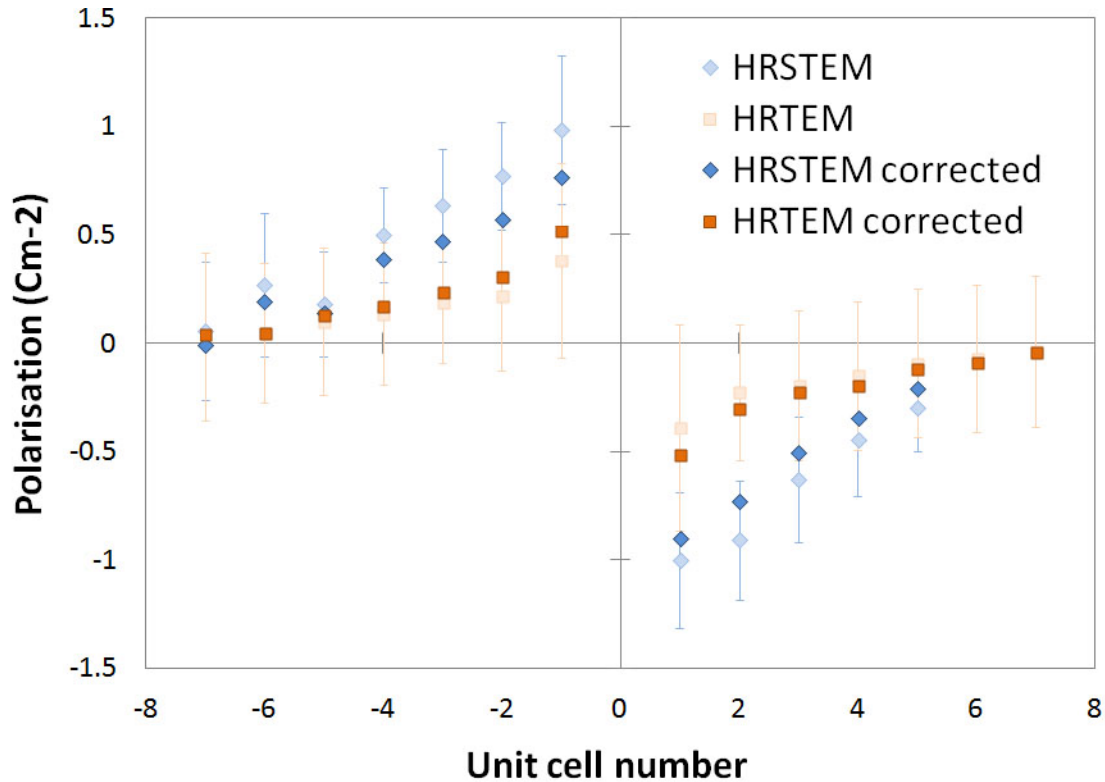


Figure 4.13: Quantitative comparison of polarisation calculations before and after including the electron channelling effects in the z-direction as a function of distance from the APB boundary for both cases. The error bars in the two cases were calculated from the standard deviation in the out-of-plane peak position measurement after averaging for the two cases.

the best areas for analysis where any mistilt did not skew the results. Clearly, diagnosing mistilt and separating this from polarisation will be more challenging and more critical for structures where there is no such head-to-head mirror symmetry. Thus to conclude, measuring polarisation quantitatively from atomic resolution images is fraught with more difficulties than are immediately obvious. Specifically, using oxygen atoms as part of the quantification is problematic as measuring the positions of these columns quantitatively is very hard as they are often displaced in the image from their true position. As a result, the only way to perform this reliably would be to perform image simulations, determine the imaging parameters, and then change the crystal model and resimulate iteratively until the image can be matched to a simulation and the actual oxygen shifts measured from the model.

## 4.4 Discussion and conclusion

In summary, the polarization of a doped BiFeO<sub>3</sub>-based perovskite of composition Bi<sub>0.85</sub>Nd<sub>0.15</sub>Fe<sub>0.9</sub>Ti<sub>0.1</sub>O<sub>3</sub> by electric fields originating from charged “APBs” has been considered in detail. Two different techniques (HRSTEM simultaneous dark and bright field imaging, and HRTEM using the negative C<sub>s</sub> imaging (NCSI) technique) have been used, and similar trends in structure and polarization were observed in both systems. However, quantitative differences were found, where for HRSTEM the peak polarization was calculated to be almost 1Cm<sup>-1</sup>, whereas for HRTEM, results show that the polarization is about 40% of the values given by HRSTEM technique. This discrepancy is related to differences in the specimen thickness required for the two imaging modes. The thickness of two samples believe to be about 16nm for STEM and about 1.6nm for TEM. As a result, there are very big differences in electron channelling between the two cases, with one critical oxygen column being shifted in the image from its real position in both techniques, but in opposite directions. For HRTEM, the oxygen column was shifted away from the nearby Bi column, whereas for HRSTEM it was shifted towards that Bi column. Additionally, polarisation is probably reduced in the HRTEM specimen since it is so thin and the surfaces are affecting the electrostatics within the sample significantly. This has the effect of overestimating polarisation from HRSTEM and underestimating polarisation from HRTEM. It is clear from this work that an iterative simulation matching procedure would be critical to any future studies in quantitative polarisation determination from atomic resolution electron microscopy.

# Chapter 5

## Novel structures at the junctions of antiphase boundaries (APBs)

### 5.1 Introduction

Antiphase boundaries occur in all sorts of ordered materials, where the origin of the unit cell is translated between two different locations in the unit cell. A simple example would be the B2 or CsCl structure where the origin could be defined at either a cell centre or a cell corner, when there would be no difference in the disordered body-centred-cubic structure. Since the origin of the unit cell shifted by half a unit cell in passing across the boundary, or the two lattices to either side can be considered in antiphase to each other this is called an antiphase boundary phase (APB). The precise structure and morphology of an APB can vary depending on the system and formation mechanism. Whilst they are often found in ordered intermetallic alloys, they can also be seen in perovskite oxides, like those observed by Lebedev *et al.* [156]. In previous work at Glasgow, APBs have also been found in highly Ti-doped  $\text{BiFeO}_3$ , and different structures have been found for flat terraces and for steps [150, 157, 53]. This shift (half of a unit cell) has also been detected in

this work when the APBs are crossed horizontally and vertically. Namely, the cross and corner APBs. These will be discussed in sections 5.d and 5.3.

In the current chapter, the structures of junctions between antiphase boundaries in Ti-doped  $\text{BiFeO}_3$  are analysed. Firstly, a crossing of two APBs is studied in detail in section 5.2. This is followed by a quantitative investigation into the use of non-rigid registration for processing of STEM image series. Finally, an initial investigation of the structures of 90 corners on APBs is presented.

## 5.2 STEM imaging of the crossing of APBs

Figure 5.1 shows a HAADF STEM image of the area of interest from a  $(\text{Bi}_{0.85}\text{Nd}_{0.15})(\text{Fe}_{0.9}\text{Ti}_{0.1})\text{O}_{0.3}$  sample taken along an  $[001]$  direction. The structure is a crossing of two APBs. This image was created by the alignment and summation of 21 images, after the correction of scan noise and distortions, as discussed in more detail in section 3.2.2. The images have been processed to take into account distortion effects (due to stage drift) and alignment using the non-rigid registration procedure discussed in section 3.2.2. Figure 5.1a represents a larger field of view (ie. a large pixel size) showing the structure of interest relative to the surrounding material. Above the APB cross-like structure, the boundary is fairly planar with only a single step in the field of view. To the left and right, the boundaries are heavily stepped and form a descending staircase morphology. Several steps are seen at the boundary below the APB cross-structure, which then has an overlapped appearance extending across two or three unit cells of the perovskite. This kind of feature has previously been seen in images of this type of material, and has been examined using a focal series and shown to correspond to a boundary inclined to the vertical within the thickness of specimen. Despite the fact that depth of field of STEM images is relatively short, it still spans several nm. This results in an overlap contrast where

the boundary inclination is sufficient.

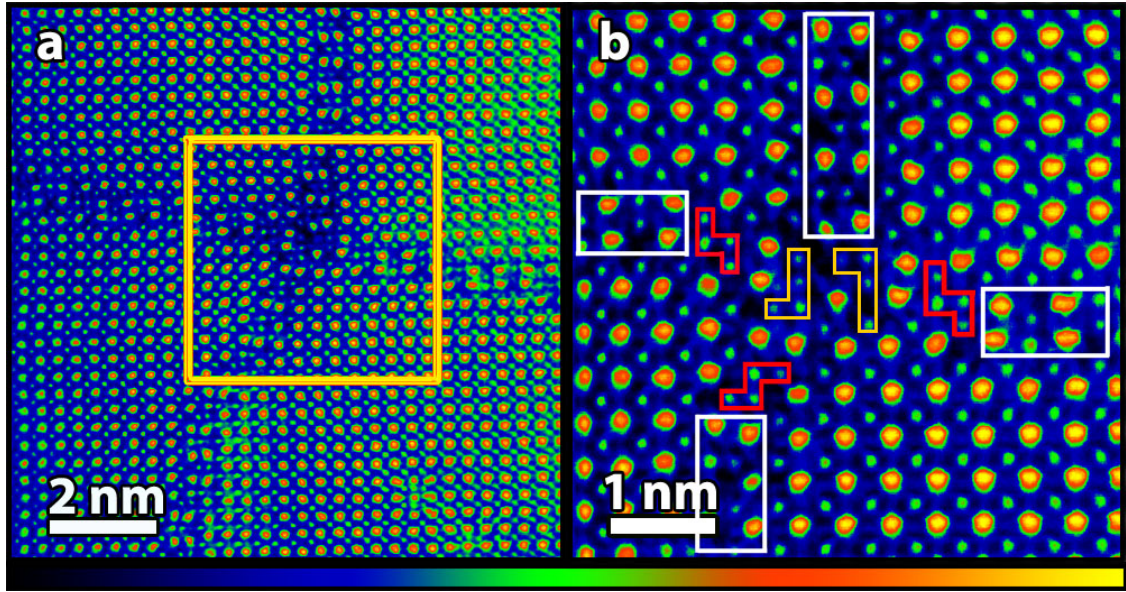


Figure 5.1: HAADF imaging of APB in  $\text{BiFeO}_3$ . Images are represented on the false colour intensity scale shown below the images; the brighter atoms are the heavy A-site atoms (Bi/Nd), whereas the less bright atoms are the B-site atoms (Fe/Ti), oxygen atoms are not visible in this imaging mode. a) a field of view of  $\sim 15\text{nm}$  at a pixel size of  $\sim 0.15\text{\AA}$  to show the context of the APB cross within the ceramic; b) a higher magnification view of an area of  $\sim 5\text{nm}$  at a pixel size of  $\sim 0.5\text{\AA}$  showing the detailed structure of the APB cross. Two “L”-shaped structures are indicated. Steps and flat terraces are indicated by red and white boxes, respectively.

Figure 5.1b was recorded using a higher magnification, to show a smaller field of view and more detail of the APB cross-like structure’s core. Comparing the structure with images of steps and terraces obtained before [68], it can be seen that the cross is composed mostly of the same features, which are indicated by the red and white boxes shown in figure 5.1b. However, there are also new structural units in this cross, that have not been seen previously: with B-site atoms arranged in “L”-shaped structures and these are marked with yellow boxes as shown in figure 5.1b.

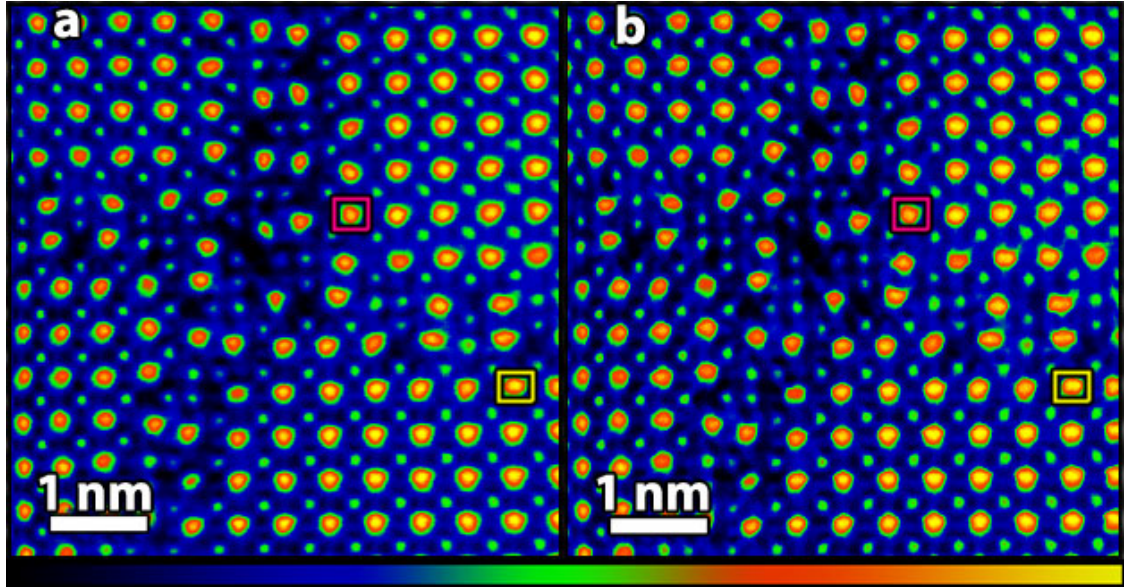


Figure 5.2: HAADF imaging of APB in  $\text{BiFeO}_3$  using a) Simple align procedure b) Smart align procedure. Images are represented on the false colour intensity scale shown beside the images, the brighter atoms are the heavy A-site atoms (Bi/Nd), whereas the less bright atoms are the B-site atoms (Fe/Ti). The line profiles (shown in figure 5.2) of peak1 and peak2 are indicated by the red and yellow boxes, respectively.

### 5.2.1 Quantitative analysis of a non-rigid registration procedure

In figure 5.2, the HAADF images shown were processed from image stacks by using the two procedures mentioned in section 3.2. In figure 5.2.a ( Simple align procedure), the images are aligned simply by diagnosing the necessary shifts to align the images. While in figure 5.2b (the Smart Align procedure), the exported data from stack of images are non-rigid registered (for distortion) and rigid registered (for drift), where the local distortions in one image are stretched to corresponding distortions in the rest images to fit them. In order to investigate the quantitative differences using the previously mentioned procedures, quantitative evaluations have been carried out on these processed images of a novel type of APB.

For an investigation into the quantitative differences, the A-site and B-site atom positions for the whole image were overlaid using Smart and Simple methods.

However, no significant difference is observed as shown in figure 5.3.

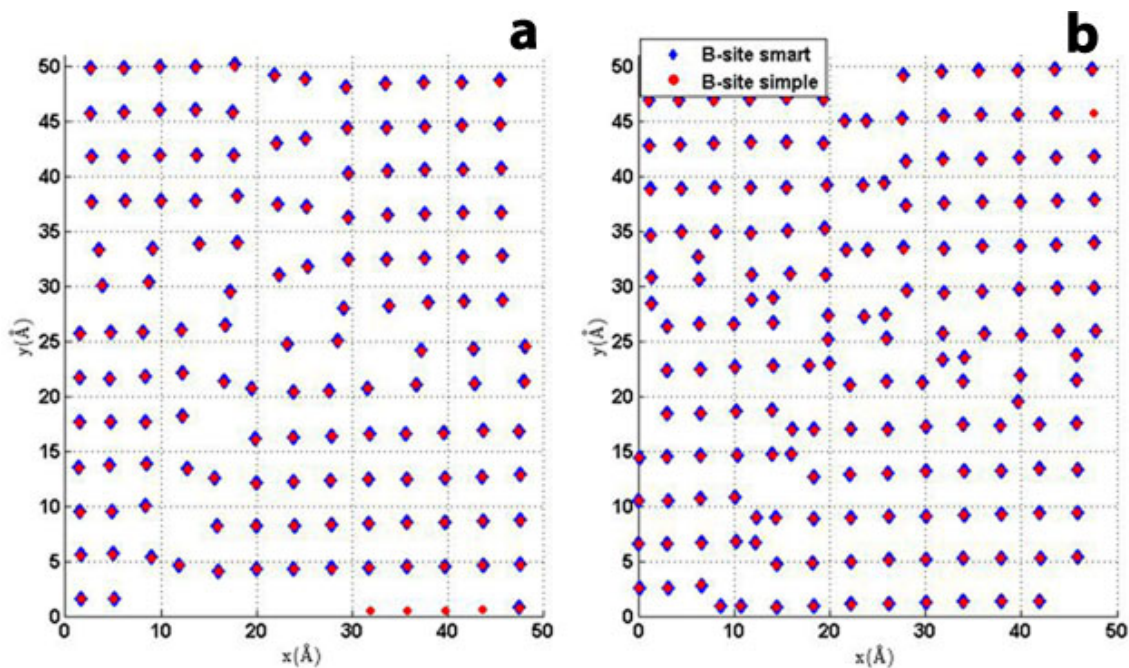


Figure 5.3: Overlays of both Simple and Smart align procedures for a) A-site positions, and b) B-site positions.

To present the quantitative differences in more details, two peaks (i.e. peak positions) were selected using Digital Micrograph in order to study their profiles quantitatively:

1) Peak1 and peak2 positions:

These are shown in figure 5.2 and their overlaid plots are shown in figure 5.3.

The line profiles of both peaks (peaks 1 and 2) are taken from the same atom columns in both images. The data from the profiles is then exported to a spreadsheet and scaled by the peak maxima and the plots are subsequently overlaid in order to see the difference between the two profiles. The most obvious difference between the profiles for both peaks (1 and 2) is that the plots of Smart align are significantly steeper and much broader than Simple align which are more likely to be gradual. This can be shown clearly in figure 5.4 (a) and (b).

As the atomic column peaks from atomic resolution electron microscopy

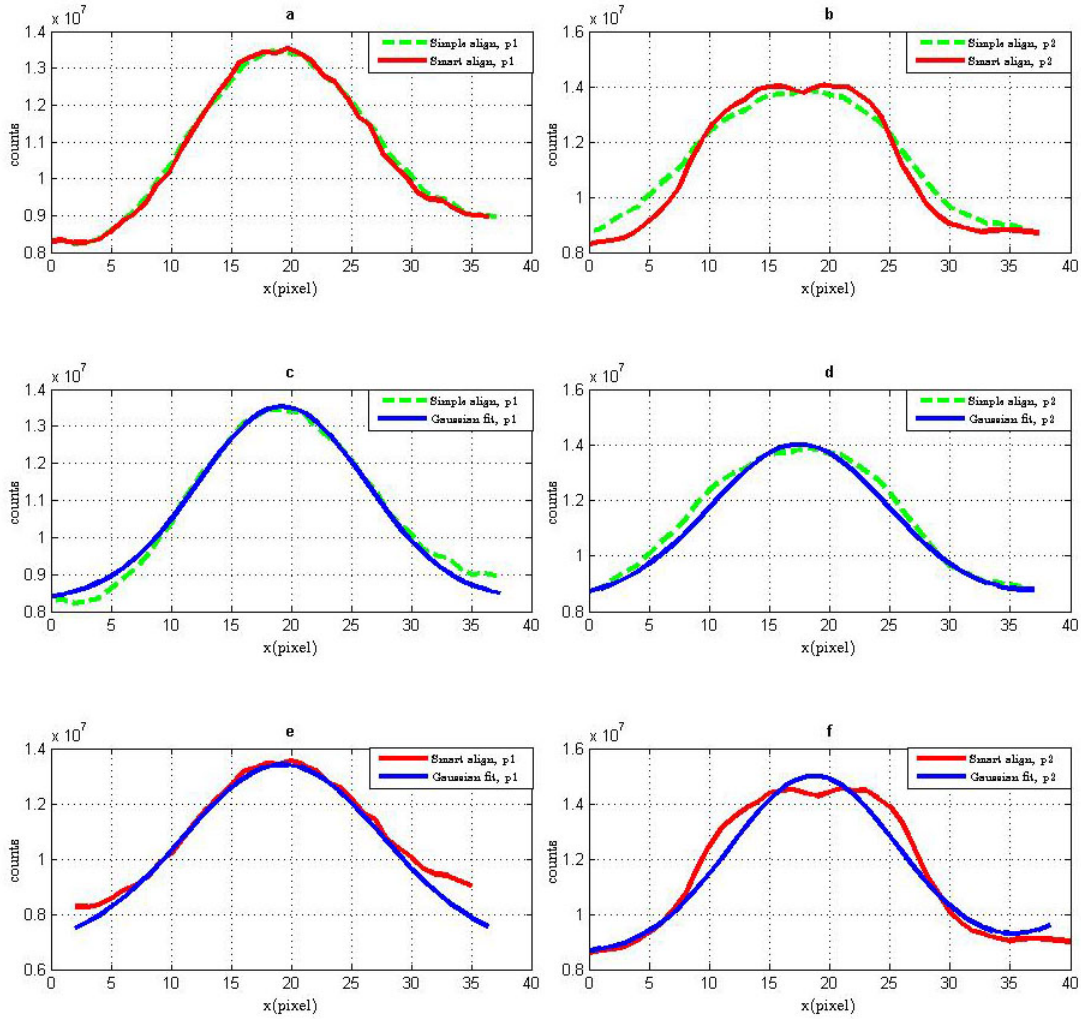


Figure 5.4: A comparison of actual peak profiles with Gaussian fits for images processed using rigid registration and using "Smart align". (a) and (b) Peak profiles using both rigid registration (green), and Smart align (red) for a) Peak1, and b) Peak2. (c)-(f) The overlay of actual peak profiles (green for rigid registration and red for Smart align), and fits (blue), for c) Simple align procedure for peak1 d) Simple align procedure for peak2 e) Smart align procedure for peak1, and f) Smart align procedure for peak2.

images are expected to have 2D Gaussian profiles, the experimental data is plotted together with the Gaussian fits to enable easy comparison.

2) Peak1 and Peak2 positions:

Positions of peak1 and peak2 in the experimental image and its Gaussian fit image for simple align and Smart align procedures are shown in figures 5.5a and b.

The data plot profiles, as shown in figures 5.4(c) and 5.4(d), compared to

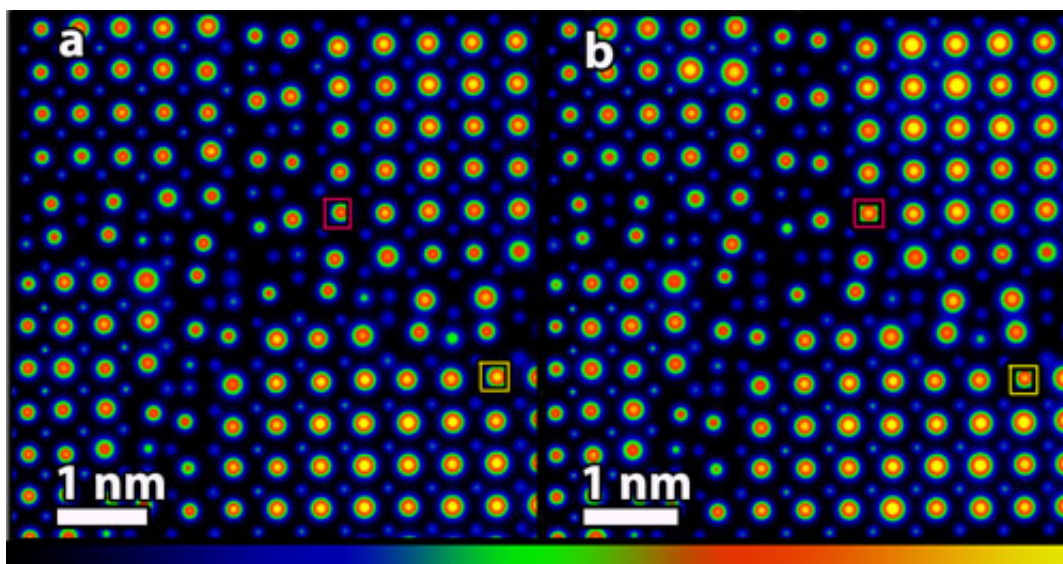


Figure 5.5: The line profiles of peak1 with red boxed and peak2 with yellow boxed produced by using the Gaussian fit for a) Simple align, and b) Smart align. The Smart align (non-rigid registration) gives a slightly sharper image, although the difference is subtle.

their Gaussian fit profiles show that the Simple align procedures show a significant improvement to their Gaussian fit profiles. Figures 5.4(e) and 5.4(f) shows that the profiles of the Smart align procedures produce a less accurate description of the data.

At first glance, the contrast after Smart align appears better, whereas the Simple align image appears more blurred. Nevertheless, the overlay of atom positions for A-site and B-site positions for both methods reveal the same tendency, as shown in figures 5.3 (a) and (b). For this reason, more quantitative evaluations are made. The profiles of peaks 1 and 2 (peak positions) using the two methods are taken as examples, which are shown in figures 5.4 (a) and (b). For Smart align the profiles of peaks 1 and 2 are steeper at the edges than the Simple align which are more likely to be gradual. The tradeoff for this is that the profiles at the peak for both peaks 1 and 2 are broader than for Simple align. Furthermore, the profiles seem less Gaussian-like after Smart align, whereas for simple averaging, the Gaussian profile is a good approximation for the main central region of the image of each column. The reasons for this differences observed after Smart align require investigation and need

to be overcome before this procedure can be widely recommended for quantitative processing of STEM imaging data. The above calculations have been done using Smart align V1.8.

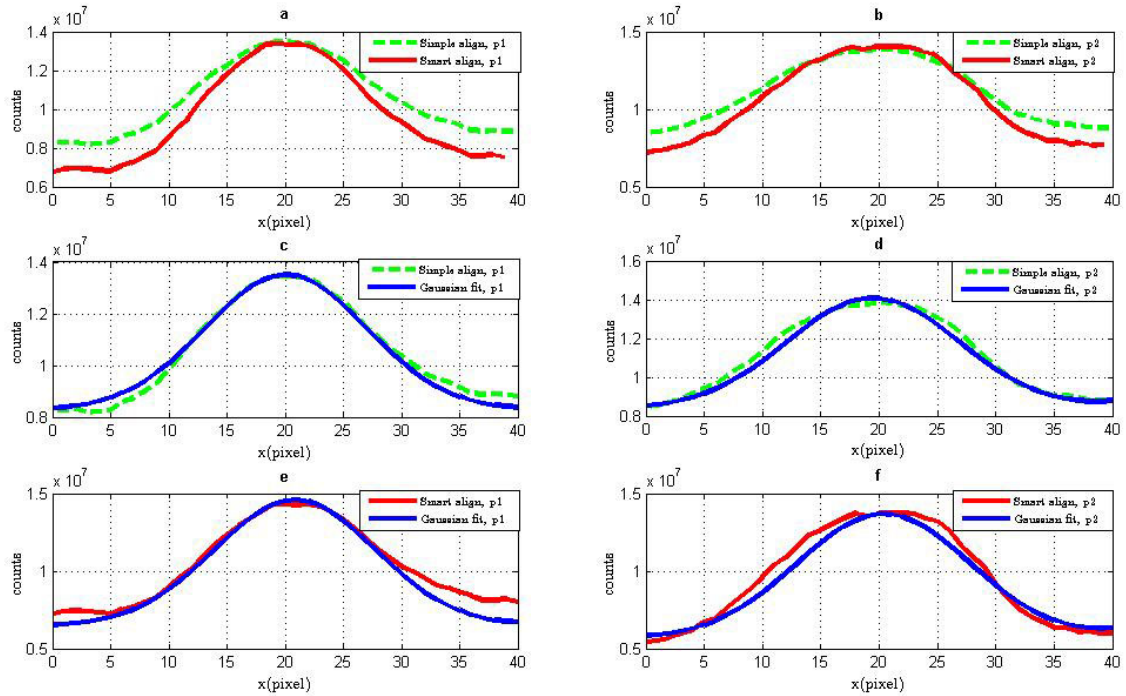


Figure 5.6: A comparison of actual peak profiles with Gaussian fits for images processed using rigid registration and using (V1.9) "Smart align" after optimisation. (a) and (b) Peak profiles using both rigid registration (green), and Smart align (red) for a) Peak1, and b) Peak2. (c)-(f) The overlay of actual peak profiles (green for rigid registration and red for Smart align), and fits (blue), for c) Simple align procedure for peak1 d) Simple align procedure for peak2 e) Smart align procedure for peak1, and f) Smart align procedure for peak2.

After this analysis was performed, a new version of "Smart align" was released which fixed a number of bugs (V1.9). This was then used on the same dataset and the results are shown for the same peaks in figure 5.6. Whilst it was not completely clear which alterations to Smart align were most significant for this, it is clear that the peak shapes were much more Gaussian than before and the results from this second alignment are used in the remainder of this chapter.

In order to show the discrepancies in fitting across the whole images, the fit images for both procedures have been subtracted from the actual images as shown in figure 5.7. The same behaviour is observed in both cases and almost no discrepancy is found between them. All atoms (A-sites and B-sites) are well subtracted except the diffuse scattering between the atoms which is probably not well described by a Gaussian anyway. Moreover, there are some atoms which they are not fitted very well and therefore the subtraction still leaves strong residuals: some specific positions are highlighted with white boxes while red boxes show the rest of the atom columns are almost uncharged. Noise or nearby columns can sometimes disturb the fitting, and that this is typical in such 2D Gaussian fitting of real experimental images. Nevertheless, in general, residuals were slightly lower for the improved (V1.9) Smart align procedure, and so this was adopted for the remainder of the work.

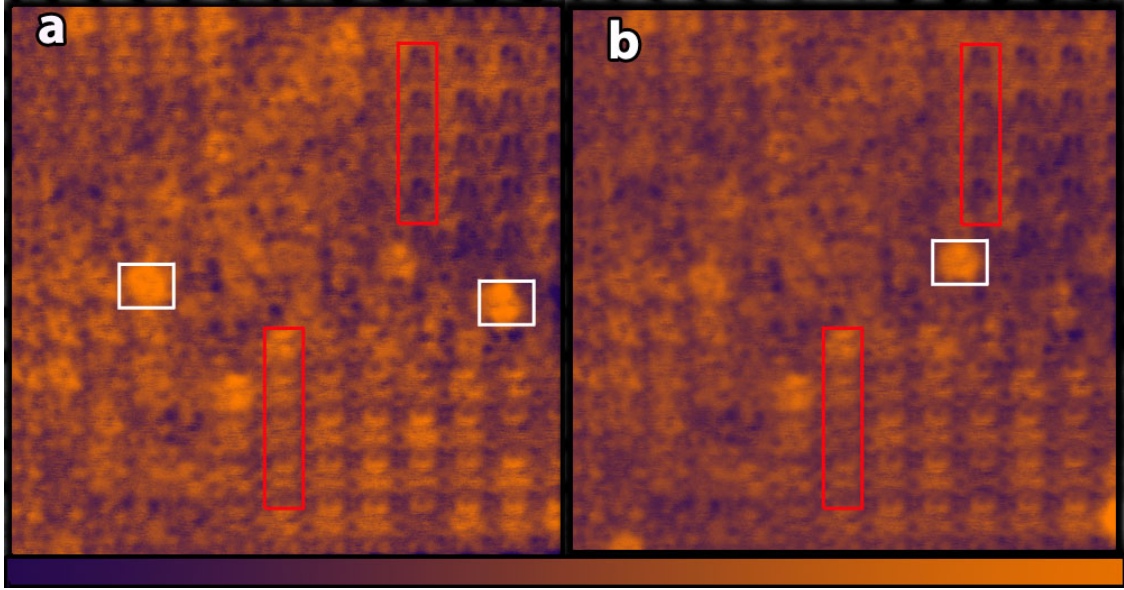


Figure 5.7: Resulting images in which the fit images were subtracted from the experimental images for a) Simple align procedure b) Smart align (V1.9) procedure. White boxes show where the procedures are failed. While red boxes show the rest of the atom columns are same.

## 5.2.2 Finding atom positions after non-rigid registration

In this work, APB cross structural images were taken at the SuperSTEM facility using a Nion UltraSTEM. For serial microscopy data, care needs to be taken to deal not just with rigid body shifts from drift, but also local distortions from environmental and electrical instabilities [113, 112], we chose to use the non-rigid registered data for further analysis.

After the local distortions have been removed from the HRSTEM images using Smart align (see section 3.2.2), a patch of interest was then cut-out from the whole HRSTEM image (figure 5.1b) to proceed the data analysis. The Image Analysis routine for DM provided by Dr Bernhard Schaffer (Gatan GmbH, München, Germany) was then used to quantify the atomic peak positions through 2D Gaussian fitting. After all the peak positions are refined, they are exported to spreadsheets for further analysis. As for previous quantitative studies of atomic resolution STEM images [139, 66, 67, 68], distortion correction was performed to set the [100] and

[010] directions perpendicular along the x and y axes. This is followed by calibrating the data to make the crystal cells to be squares in the [001] crystal direction with a lattice parameter of  $\sim 3.965\text{\AA}$ . It is worth mentioning that all of these corrections were executed utilising regions outside the APBs (i.e ideal perovskite structure) by applying least squares fitting method to assign the gradients and spacings of rows of peak positions. Then the resulted fit parameters are converted to correction matrices to apply to data set for corrections such as rotation and shear matrices. To do the rotation correction, a matrix is formed using averaged rotation gradient from the rows of peaks around (below and above) APBs and then applied to data sets. For shear correction, a matrix was formed from the averaged gradient of columns of peaks which should be vertical on either side of APBs.

### 5.2.3 Atomic resolution chemical analysis

Other defects (such as nanorod, terraces, and steps) previously observed in this material are non-stoichiometric, and therefore understanding which atom is which is (in each case) essential as well as requires atomic resolution EELS to be well comprehensible [66, 67, 68].

For the current work, the chemistry of the APB cross structure was carried out using EEL-SI utilising the following procedure. To start with, the recorded spectrum image was handled to remove X-ray spikes due to stray fields including stray scattering in spectrometer or other stray radiation [130]. Following this, in terms of reducing the noise, a multivariate statistical analysis [131] plug-in was used to perform PCA [130] (see section 3.5.2). After the PCA is carried out, datasets were then reconstructed from just those parts containing real signals from the object and ignoring the rest noise signals. Quantitative compositional mapping from core loss edges were performed over a new modelling based elemental quantification routine for DM was utilised (courtesy of Dr Paul Thomas, Gatan UK Ltd). Accordingly,

The fit windows were performed from  $\sim 400$  to  $1050\text{eV}$ , covering the Ti-L<sub>2,3</sub>, the O-K, the Fe-L<sub>2,3</sub> and the Nd M<sub>4,5</sub> edges. These maps were also run through Smart align (which combines rigid and non-rigid registration) to reduce distortions from electrical and environmental instabilities [105, 112]. Moreover, high frequency noise has been taken into account and corrected for [111]. However, it is worth mentioning that there is no beam damage effects as the HRSTEM images taken at  $100\text{keV}$ .

Figure 5.8 shows the EELS mapping used to unravel and understand the chemistry of the structure. Figure 5.8a-5.8d show the chemical elemental maps of the core of APB cross structure for Fe, Bi (simultaneously recorded HAADF image), Ti, O map, and finally RGB overlay maps except O element (red = Fe, green = HAADF (Bi), and blue = Ti). Ti segregates towards the centre of the APB if terraces occur near the edges of the APB cross. Elemental mapping highlighted a large concentration of Fe at every steps which they are shown in figure 5.1, which are also Ti deficient. Due to the small ( $\sim 2\text{\AA}$ ) separation between the columns, these maps are not atomically resolved. At the two L-shapes at the core of the APB cross, there is a large concentration of Fe, which suggests that these shapes are mainly iron oxide. Maps then overlaid as well as a false colour scale is utilised in order to be readable as shown in figure 5.8e.

#### 5.2.4 Reconstructing the 3D model of the cross

The 3D structure of an object cannot be determined from a single projection, unless prior information about the atomic ordering is known. For this particular structure, another direction allowing the individual atom columns to be seen is not available or possible. The following additional information was needed when the structure was being reconstructed: the known structure of the terraces [66] and steps [68]. The additional assumptions made are: any structures in the APB cross are BO<sub>6</sub> octahedra (either corner sharing or edge sharing) [68, 66], geometrical

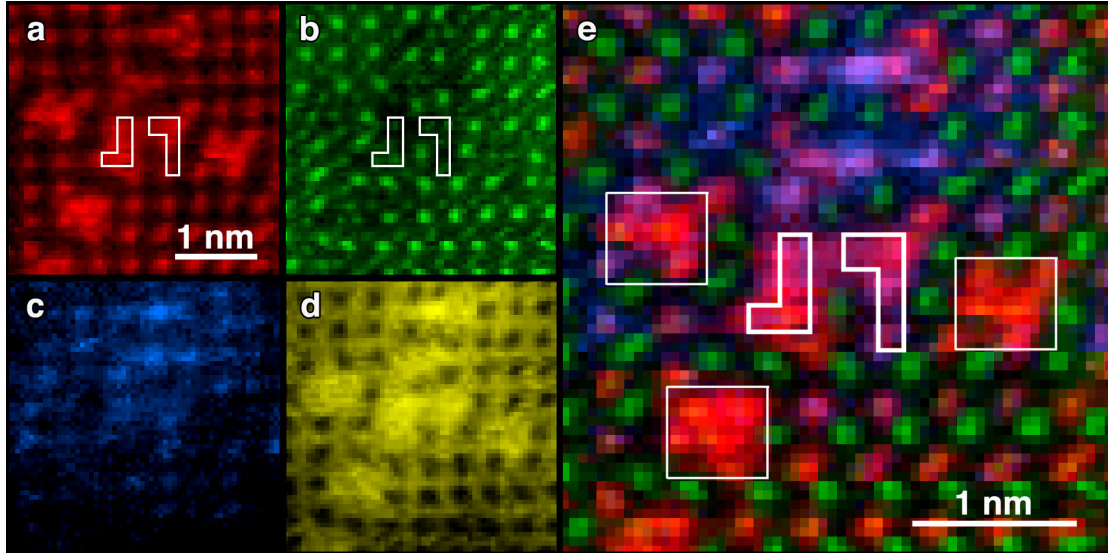


Figure 5.8: Elemental maps from EELS of the intercept of the boundaries (defects as a cross shape). (a)-(e) Chemical mapping of (APBs) showing the intercept of the boundaries: (a) Fe map, (b) simultaneously recorded HAADF image, which predominantly shows the Bi positions, (c) Ti map, (d) O map, (e) RGB mixed map with Red = Fe, Green = HAADF (Bi), and Blue = Ti. The “L” shaped arrangements of Fe atoms are marked in some maps. Square boxes indicate step regions.

compatibility between the structure and the APBs on either side and all oxygen positions in the structure are fully occupied with no significant numbers of oxygen vacancies (even if it leads to local concentrations of negative charges) [67]. This has been confirmed using simulations where the contrast is only well-fitted to the experiment when oxygen sites are fully occupied, which resulted in the conclusion that the boundaries must be negatively charged [67]. The local negatively charged boundary will act to compensate an excess of  $\text{Ti}^{4+}$  in the surrounding perovskite matrix, but will also lead to a local polarisation of the surrounding perovskite [68, 66].

In order to be classified as an APB, both vertical and horizontal shifts of half a primitive unit cell are required. The shifts are created by incorporating edge-sharing octahedra into the structure. For this composition (BFO), since B-site atom positions are usually displaced from each other by an amount of one primitive

unit lattice cell parameter,  $a$ , which  $a \sim 3.965\text{\AA}$  [67, 68], therefore edge-sharing of  $\text{BO}_6$  octahedra can easily be inferred from in figure 5.9b. When two octahedra share an edge, the Fe (B-site) atoms should be located a distance of  $a/\sqrt{2} \approx 2.8\text{\AA}$  from each other. Therefore the edge-sharing can be seen in a [001] image in two different ways:

1. Edge-sharing in-plane, where both edge-sharing octahedra lie at the same vertical height, which results in two B-site atoms imaged  $\sim 2.8\text{\AA}$  apart.
2. Edge-sharing not in-plane, where an edge-sharing octahedra displays a shift of  $a/2$  between B-site atoms both vertically and horizontally which in turn results in the Fe atoms appearing  $\sim 2\text{\AA}$  apart.

The peak positions in the STEM images were evaluated quantitatively utilising Gaussian fitting procedure, and then data was determined for A-site positions (Bi/Nd) as well as B-site (Fe/Ti) peaks in the structure. From the information detailed above, the atom positions in the  $\mathbf{z}$ -direction were determined. O-site (oxygen) positions were then included utilising the position that they would have occupied in previous work (terraces and steps), with the exception of the structures where the corresponding positions in the previous APBs are unclear such as the L-shaped structure, in which case oxygen atom positions were adopted to guarantee octahedral coordination of all B-site atoms. The O-site positions were then permitted to relax, whilst keeping the Bi, Fe and Ti positions stationary, utilising a newly developed Monte Carlo calculation incorporated with in CrystalMaker 9.1 software (CrystalMaker Software Ltd., Oxford, UK). This Monte Carlo algorithm relaxes a structure based on minimising the bonding energy of all the defined bonds for each atom, based on simple interatomic potentials. The procedure did not have a formal convergence criterion, but by inspection, whilst some considerable of atom positions were observed at the beginning, however after around  $10^6$  cycles any changes of atom positions per cycle were no longer visible and the refinement was stopped.

The algorithm was based on centrosymmetric atomic potentials, and as such took no account of spontaneous polarisation, the normal atom positions were not fully reproduced due to the unconstrained polarization, yet in any event guaranteed that the O atoms were sitting in sensible positions. To improve upon this experimentally would require BF STEM imaging of one of these structures in a material of appropriate thickness and under perfect imaging conditions, although the reader is referred to chapter 4 for a discussion of the difficulties in this method. The present APB cross-structure was in a material that was probably too thick for high quality BF STEM imaging, and also contained some bending across the area of interest, making the achievement of perfect imaging conditions at all points almost impossible. Performing a simulation using density functional theory, as used in previous work [66], is somehow unrealistic for this structure, since the number of atoms that is required is huge and the computational requirements would be unfeasibly large.

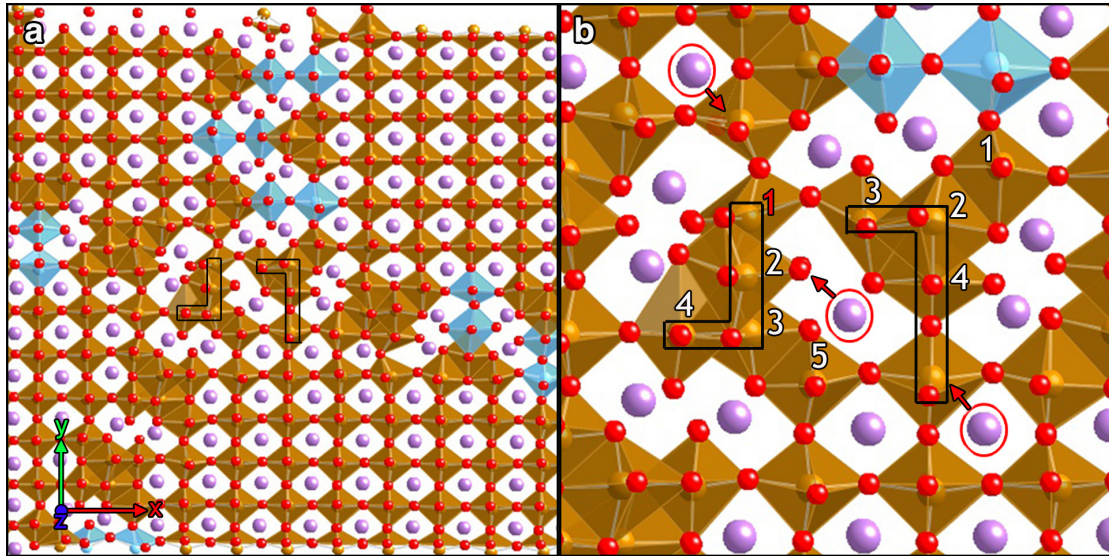


Figure 5.9: The 3D structural model for the APB cross structure: a) the overall structure; b) magnified view of the core of the APB cross showing the two L-shaped arrangements of edge-sharing FeO<sub>6</sub> octahedra. Red circles indicate the off-center movement of atoms and directions shown by red arrows.

The subsequent 3D model after reconstruction is demonstrated in figure 5.9a. This shows that the L-shaped structures are composed entirely of edge-sharing

FeO<sub>6</sub> octahedra, in a similar manner to the Fe-rich step structures previously reported [68]. It ought to be noticed that although the two structures have similar structures, the details differ. The L-shaped structure to the left (L-structure) contains five edge-sharing octahedra per layer in the **z**-direction, whilst the right hand L-shaped arrangement consists of just four edge-sharing octahedra per given layer and they are marked by numbers as shown in figure 5.9b.

The reconstructed model likewise demonstrates that Bi atom positions are shifted away from the perfect centrosymmetric positions between the octahedra close to the structural units of the APBs, whether close to the APBs that have been reported previously [67, 68] or towards the core of this APB cross structure. These off-centre movements are directed towards the centre of the APB cross for Bi (A-site) atoms on the sides of this central region as exemplified by the atoms circled in figure 5.9b. This shows a significant polarization in the surroundings of the center of the APB cross, and proposes that it is negatively charged, in a comparable way to the planar and stepped regions of the APBs addressed previously [67, 68]. Unfortunately, changes in imaging conditions over the zone taken by the APB cross, which were at least partially due to some sample bending in the area, prevent performing a dependable mapping of polarization around this component.

### 5.2.5 Model validation via image simulation

For the APB cross structure, the simulation is considered in terms of knowing the sample thickness in the defect region as well as the best fit for the Debye-Waller factors (Biso) for the Bi(A-sites) and (Fe,Ti) B-sites in the bulk structure. Consequently, the possibility to find a match between simulation and experiment can then be established qualitatively or even quantitatively. For this purpose an average of 21 ADF STEM images of a APB cross defect in BiFeO<sub>3</sub> ceramics codoped with Nd and Ti taken with 100keV electrons along an [001] direction. With the specific

end goal of confirming this structure, HAADF images were simulated utilising the Dr. Probe multislice programming bundle. The simulation results presented here were performed by Dr. J. Barthel (Forschungszentrum, Germany).

In order to do image simulation, an atomic model was provided based on the 3D structure calculated above in section 5.3.2, but represented as a crystal so that the structure could be repeated along the z-direction to allow calculations of images for any thickness.

Since sample thickness and DWFs have a similar effect on the observed ADF intensity, they were then assessed together. It is been found in all literature resources that the DWFs are agreed more on Fe values but not for Bi values. For this purpose, the simulations set up for the four small bulk patches A, B, C, and D indicated in the figure 5.10, setting B(Bi) to 0.2, 0.4, 0.5, 0.7 and 1.0Å, and for sample thickness values up to 50nm. These four different structure models (A, B, C, and D regions) extracted from the provided large super cell. These structures then overlaid to the experimental image. Within experimental microscopy settings, the STEM images were determined by 10pm of scan steps in order to achieve and match the pixel numbers of the experimental image. In both experimental and simulated images, the integrated intensities from circular areas around the intensity peaks with a radius of 11 pixels for the Bi (A-site) columns and for the Fe-O columns were exported. In the experimental image, those selected peaks are indicated by yellow circles for Bi (A-site) columns and red circles for Fe-O columns as shown in figure 5.10. Before extracting the intensities from assigned areas in the experimental image, a background level of  $6.0 \times 10^6$  counts was removed. For the current work, it has been found that removing slightly higher background (more than  $5.1 \times 10^6$ ) led to better consistency in the analysis of the four bulk regions (A, B, C, and D regions). For each region (A, B, C, and D regions), the integrated intensities Bi (A-site) and Fe-O were averaged separately, and then the ratio of the average integrated

intensities  $\langle I_{Bi} \rangle$ :  $\langle I_{Fe} \rangle$  was calculated.

From the simulation results, figure 5.11 shows that curves for the ratio of the average intensities decrease significantly with increase sample thickness, and increase with increase DWF  $B(\text{Bi})$  for the four bulk regions separately. The horizontal grey bands in figure 5.11 mark the range of values extracted from the experimental image regions respectively. It was recognised that it was unrealistic to perform a completely quantitative image comparison as there were too many free parameters to consider in order to generate the perfect unambiguous solution. Nonetheless, a set of simulations were performed to determine the utilising the Debye-Waller factors ( $B$  parameters) for BFO of Kubel *et al.* [158] of  $B(\text{Bi}) = 0.7\text{\AA}^2$ ,  $B(\text{Fe}) = 0.5\text{\AA}^2$ , and  $B(\text{O}) = 0.7\text{\AA}^2$ . According to this evaluation, the sample thickness is approximately 25nm for  $B(\text{Bi}) = 0.7\text{\AA}^2$ . It should be noted, that the thickness estimates for region A and C are systematically higher than for region B and D where the difference is estimated to be on the order of 10%. However, this contradicts to the observation where the average intensity in the left side (regions A and C) is lower than in the right side (regions B and D) of the experimental image. This inconsistency makes it impossible to extract a consistent scaling factor which would bring simulations and the whole experimental image to the same absolute intensity scale. In addition to this, the thickness estimation is quite unsafe, since the slope of the intensity ratio is very small for the estimated range of sample thickness. It has been found that the match between the simulations with the given structure model and parameters to the experimental image in the bulk regions quantitatively impossible. In contrast, figure 5.12 shows qualitative matches are possible but not 100% convincing using individual object thickness and individual intensity scaling factors for the different image areas. It is worth mentioning that the STEM probe size used in the simulations for the current work was  $0.55\text{\AA}$ (HWHM) for a Gaussian profile. Moreover, figure 5.12 shows that the intensity in the A and C regions is increased which this

could be due to the thickness gradient or due to bend upper the sample surface along the horizontal scan.

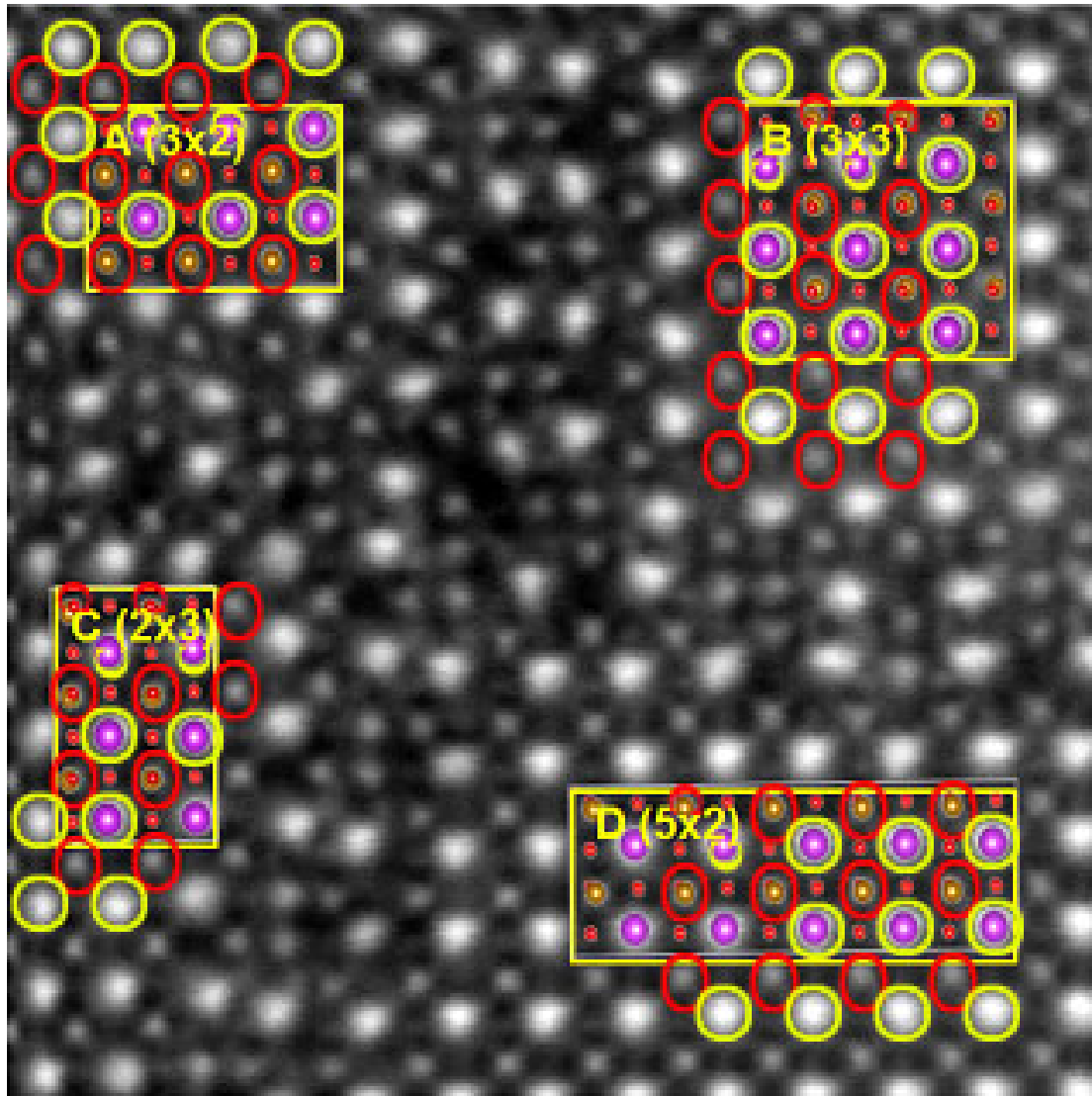


Figure 5.10: HAADF imaging of the APB cross structure shows the selected A, B, C, D regions for simulations. The purple colour indicates Bi (A-site) atoms, brown for Fe (B-site) atoms, and red for oxygen atoms. The integrated intensities that extracted from areas around the intensity peaks are indicated by yellow circles for Bi (A-site) columns and red circles for Fe-O columns.

A reasonable match was found to the experimental image for a specimen thickness of 30nm and a Gaussian source size of 0.45Å HWHM, which takes account of the electron source size, instrument and specimen instabilities, and errors from image averaging. This specimen thickness is not exact and sensible matches could be found for a critical thickness range of 24-36nm as shown in figure 5.12. A comparison

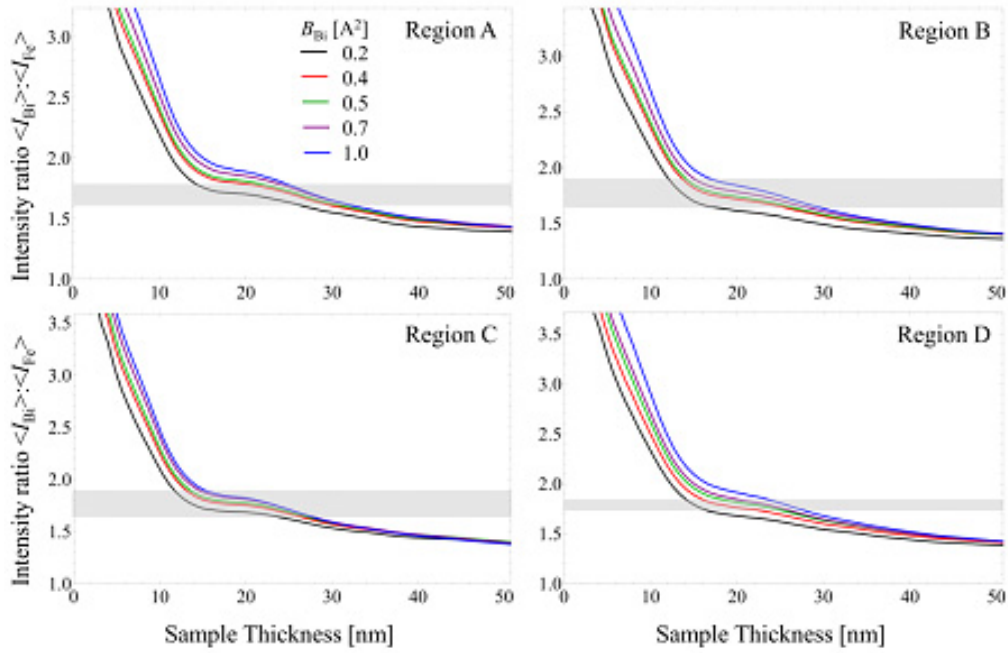


Figure 5.11: Shows the changing intensity ratio of the selected regions with respect to the sample thicknesses. The thick horizontal gray lines show the range of values that estimated from the experimental image regions. Black, red, green, pink, and blue colored lines represent the  $B_{\text{Bi}}$  parameters, 0.2, 0.4, 0.5, 0.7, and  $1.0 \text{ \AA}^2$ , respectively.

of the experiment and simulated image is demonstrated in figure 5.10. It is clear that the contrast of atom positions in both experimental and simulations are in a good agreement. For example, the area of of interest, where the two L-shaped structures are found, show a confirmation for all atom columns inside the two white boxes as shown in figure 5.13.

Since the major purpose of using simulation at this stage is matching the contrast of the HAADF image, which essentially depends upon cation peaks, it is most probable that imprecision in oxygen site position in the model of figure 5.9 would have an insignificant impact on the simulation result. Some differences are apparent in the intensities of a few sections where the two Bi (A-site) columns in the APB cross-structure and a significant amount of the B-site (Fe) columns are weaker than in the simulation, proposing that there may have been a degree of disorder (e.g. a few vacancies) on these particular columns, or that the structure

is not exactly same through the entire specimen thickness. Notwithstanding, all in all, these simulations clearly support the model in figure 5.9, which has an expected accuracy of 16pm, 17pm and 25pm for Bi (A-site), Fe (B-site) and O site areas, respectively.

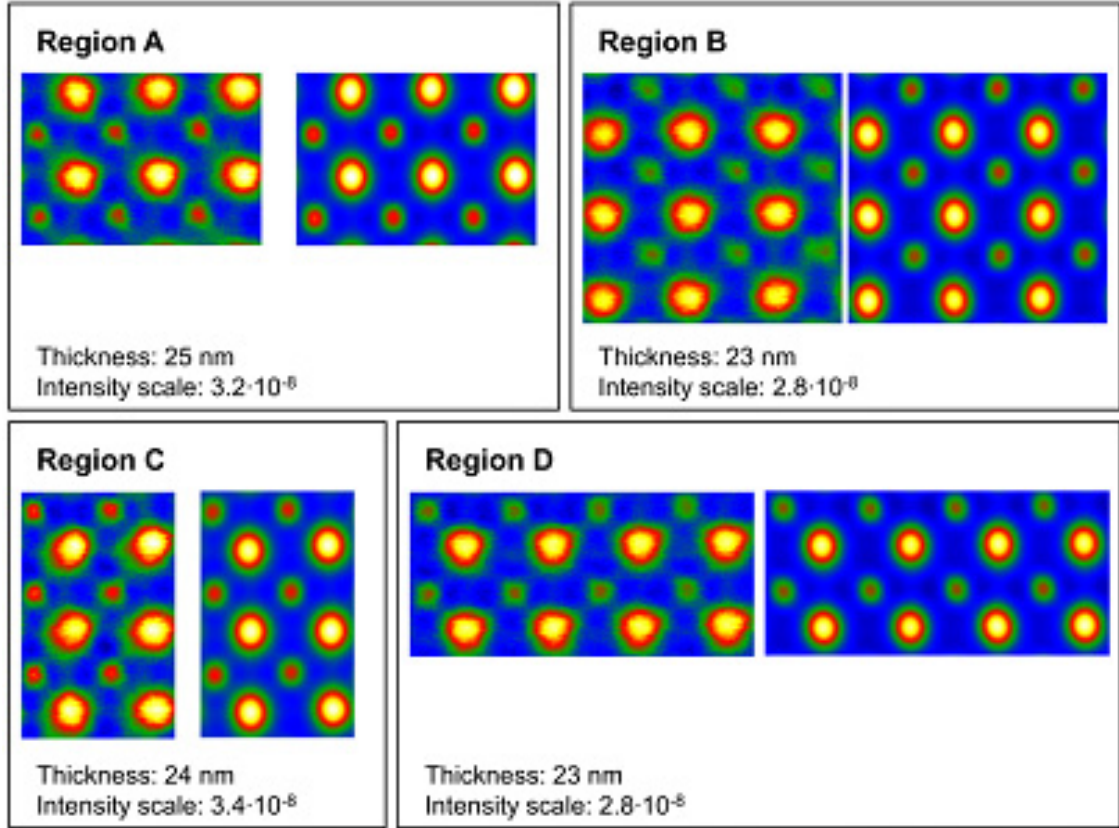


Figure 5.12: Shows the comparison of the experiment vs. simulation images for the APB cross structure (the core) of HAADF imaging with respect to the four regions. In each box, the left image represents the experiment image and the right one represents the simulation image. The intensity increases from left i.e. in A and C regions) to the right (B and D regions).

## 5.2.6 Discussion

As was previously addressed for the step regions [68], this Fe-rich APB cross structure must be comprised of a local abundance of Fe cations, with a local diffusion of Ti concentration. It appears that the unusual assembly of interlocking edge-sharing octahedra expected to make the fundamental unit cell movements to match shift-related domains together are just conceivable with edge-sharing  $\text{FeO}_6$

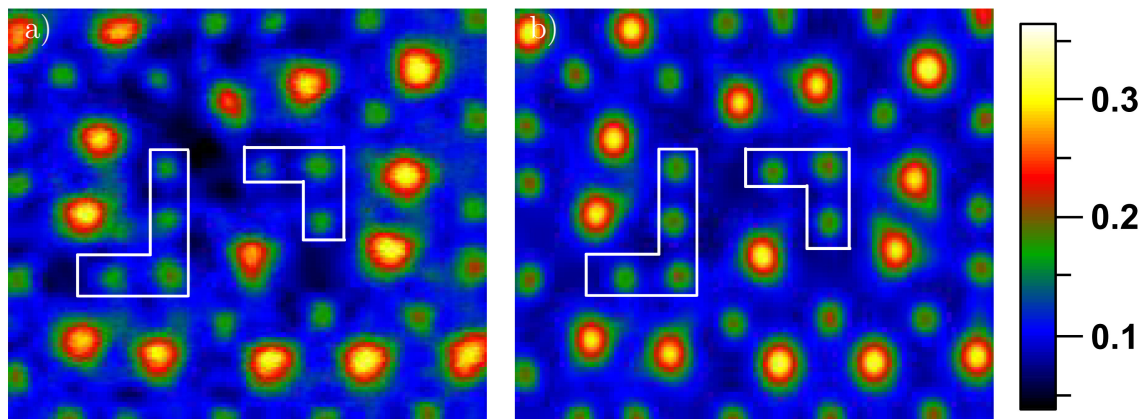


Figure 5.13: Comparison for the core of the APB cross showing a good match to atom positions for all cation columns of a) Experimental image, and b) Simulation image. The colour scale runs from  $0.06 I_0 - 0.36 I_0$ , where  $I_0$  is the incident beam intensity. The two white boxes refer to, for example, a good agreement of contrast of atomic columns for both experimental and simulation images.

octahedra; even two edge-sharing  $\text{TiO}_6$  octahedra have not been observed in all experiments performed on this novel material. This structure of edge-sharing  $\text{FeO}_6$  octahedra is seen on a considerable level in the  $\gamma\text{-Fe}_2\text{O}_3$  maghemite. It is well-known that maghemite supports permanent ferrimagnetic orderings of the  $\text{Fe}^{3+}$  cations. In particular, the magnetic spin ordering of maghemite is such that it shows near parallel arrangement of spins in  $\text{Fe}^{3+}$  edge-sharing structure, with the tetrahedrally composed  $\text{Fe}^{3+}$  ions having magnetic spins ordered antiparallel [159, 160]. What is more, further studies have uncovered some spin twisting from a perfect parallel magnetic spin arrangement [161]. Hence, the expectation is that these areas with maghemite-like edge-sharing of octahedra will support parallel magnetic spin arrangements between the  $\text{Fe}^{3+}$  ions and in this manner these L-shaped structures, and also steps on the APBs [68], are liable to display columnar areas with a permanent magnetisation behaviour. It would be interesting for future work to probe this with high resolution techniques, for example, magnetic force microscopy and electron magnetic circular dichroism [162].

### 5.3 Quantification of the structures of 90° corners on APBs

An image of a 90° corner on an APB is shown in figure 5.14a, recorded using the negative  $C_s$  imaging mode, as used in chapter 4. To allow the reader to more easily recognise the different atomic positions, a false color representation has been used. In this  $C_s$  HRTEM imaging mode, as usual, all types of atoms in the sample can be observed simultaneously. The light atoms such as oxygen ions can be seen as a very faint light blue, while the very bright yellow peaks are cation positions; it is difficult to distinguish A- and B- sites without prior knowledge. The APB structures to either side of the corner have the same structures that have been seen previously in such materials [67, 68, 163]. The vertical APB is planar as reported previously [67, 68, 163], as is the horizontal section to the left of the corner. Just above this corner, there is one step on the APB [68, 163]. Interestingly, this core structure is considered to have various possibilities in terms of modelling, the results of which were found to be somewhat controversially and are presented as an open question in the 3D model section of this chapter.

A similar APB corner structure has also been observed using HRSTEM. Figure 5.14b shows an HAADF image (taken with 100keV along an [001] direction) that was acquired in a fast scanning mode via short dwell times of just 10 $\mu$ s per pixel in order to minimize the drift effect on the individual images, and around 40 images were acquired in a sequence followed by alignment and summation, as described previously. In the HAADF imaging mode as usual the light atoms such as oxygen ions can not be seen. So, the faint light blue represent the B-site (Fe) atom positions, while the bright yellow spots show the heavy (A-site) atom positions. As for the corner shown in figure 5.14a, the APB to either side consists of flat terraces and steps of well-understood structure [67, 68].

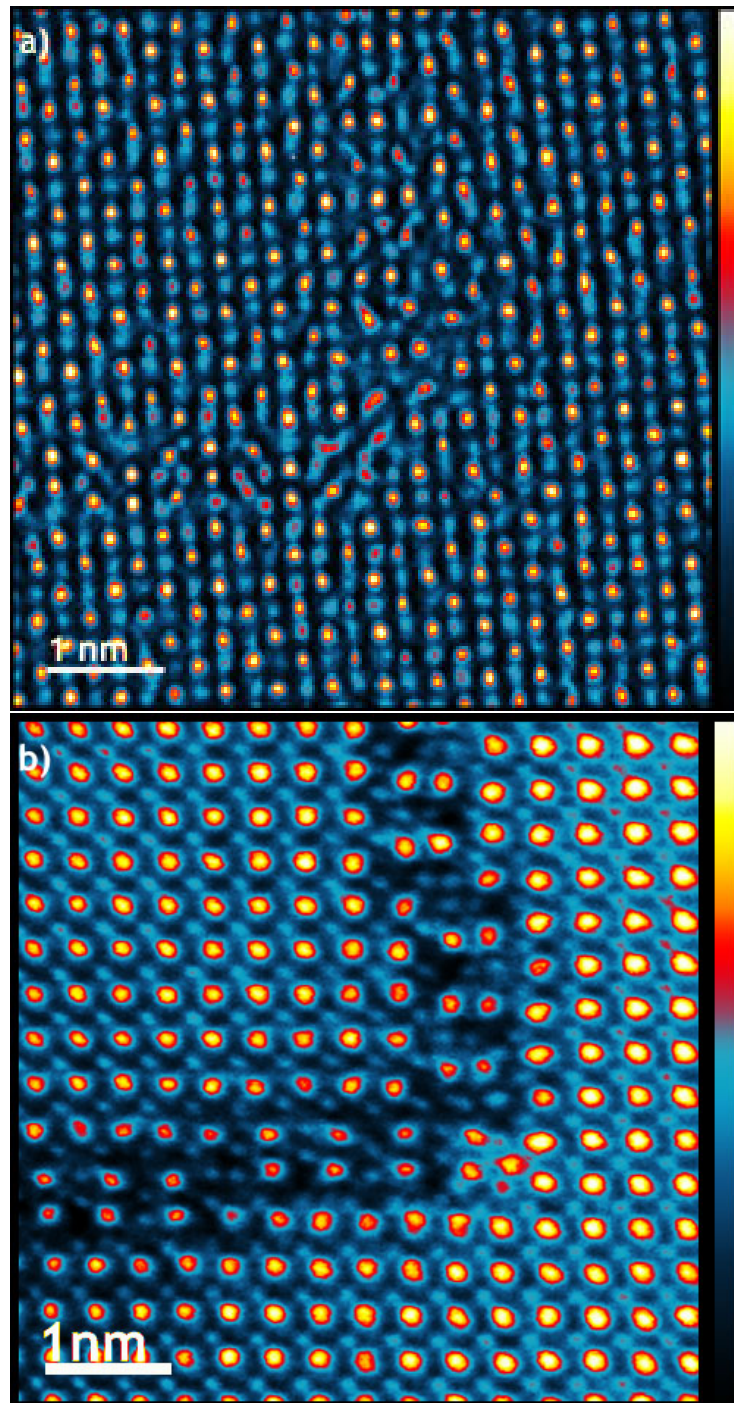


Figure 5.14: Atomic resolution images of  $90^\circ$  corners on antiphase boundaries (APBs) in  $\text{Bi}_{0.85}\text{Nd}_{0.15}\text{Fe}_{0.9}\text{Ti}_{0.1}\text{O}_3$  of a) HRSTEM image mode, and b) HRTEM NCSI imaging mode, which shows all atom columns simultaneously. The faint light blue peaks could represent the oxygen ions or iron (B-site) atom positions, while the shiny yellow spots indicate the bismuth (A-site) atom positions.

The most interesting parts of these two images of the APB corner are their cores, and there is a possibility to compare the two structures quantitatively. The atom positions were determined from the images by the methods described in section 3.3. Away from the corners, atom identification was straightforward, based on prior knowledge [67, 68]. At the corner, however, there was some uncertainty about the chemical identity of some columns, and there were no elemental maps of these features available to assist in this identification. Figure 5.15 shows the reconstructed APB corner structures for both HRTEM and HRSTEM imaging modes. Figure 5.15a represents  $C_s$  HRTEM imaging, while HRSTEM imaging mode can be seen in figure 5.15b. The  $C_s$  HRTEM images were taken with 300keV along an  $[001]$  direction and sample damage is expected in which some energy transfer to the specimen through the displacing of the atom columns. It is therefore the samples were coated during sample preparation (see 2.2.3.4) to remove undesired effects. The APB corner structures for both HRTEM and HRSTEM imaging procedures are discussed in the following section.

### 5.3.1 The 3D model of the corner APBs

A 3D model structure has been carried out for composition  $\text{Bi}_{0.85}\text{Nd}_{0.15}\text{Fe}_{0.9}\text{Ti}_{0.1}\text{O}_3$  ceramics. As mentioned above, the whole structure in both cases (HRTEM and HRSTEM) can easily be modeled except where the APBs met and form the structures of  $90^\circ$  corners. Figure 5.15 shows the entire structure of the  $90^\circ$  corners APBs. The structures of the corners have been reconstructed as well as was possible with only imaging information. Figure 5.15a shows the structure of  $90^\circ$  corners of the  $C_s$  HRTEM imaging, while figure 5.15b represents the HAADF imaging mode. In all cases, the purple colour represents Bi(A-site) atoms, the brown regions are Fe (B-site) atoms, light blue represents Ti (B-site) atoms, and red refers to oxygen atoms.

As mentioned above, the HAADF imaging mode is relatively straightforward to derive structure models from because the atom positions are readily recognizable from column intensities. However, there are some ambiguities in interpretation in the corner, and whilst the structure shown in 5.15a seems to fit the image, some bond lengths around APBs are unexpected. This is possibly due to the image distortions in all directions and these bonds are marked by yellow boxes. Consequently, the structure should be regarded as a preliminary structure, and would require further work for confirmation. Please note that separation of Ti-majority and Fe-majority sites in the corner is purely conjecture at this point and resolving this would require further experimentation.

The situation is more difficult for NCSI HRTEM, as distinguishing A-sites and B-sites is quite difficult, even in a perfect crystal. Thus, whilst the structure shown in 5.15b is a possible structure, again some bond lengths are unusually short and it would seem this needs some correction. One thing that can be categorically said, however, is that the two structures are not the same. The three Bi atoms in the corner for the structure in 5.15b are not seen in 5.15a, where the Bi arrangements are much more like those on flat terraces of APBs [67].

It seems likely from this preliminary study that there are several possible ways to turn a corner on an APB, all consisting of networks of  $(\text{Fe,Ti})\text{O}_6$  octahedra with Bi columns interspersed, and it is highly likely that many of the octahedra will be heavily distorted at the corners.

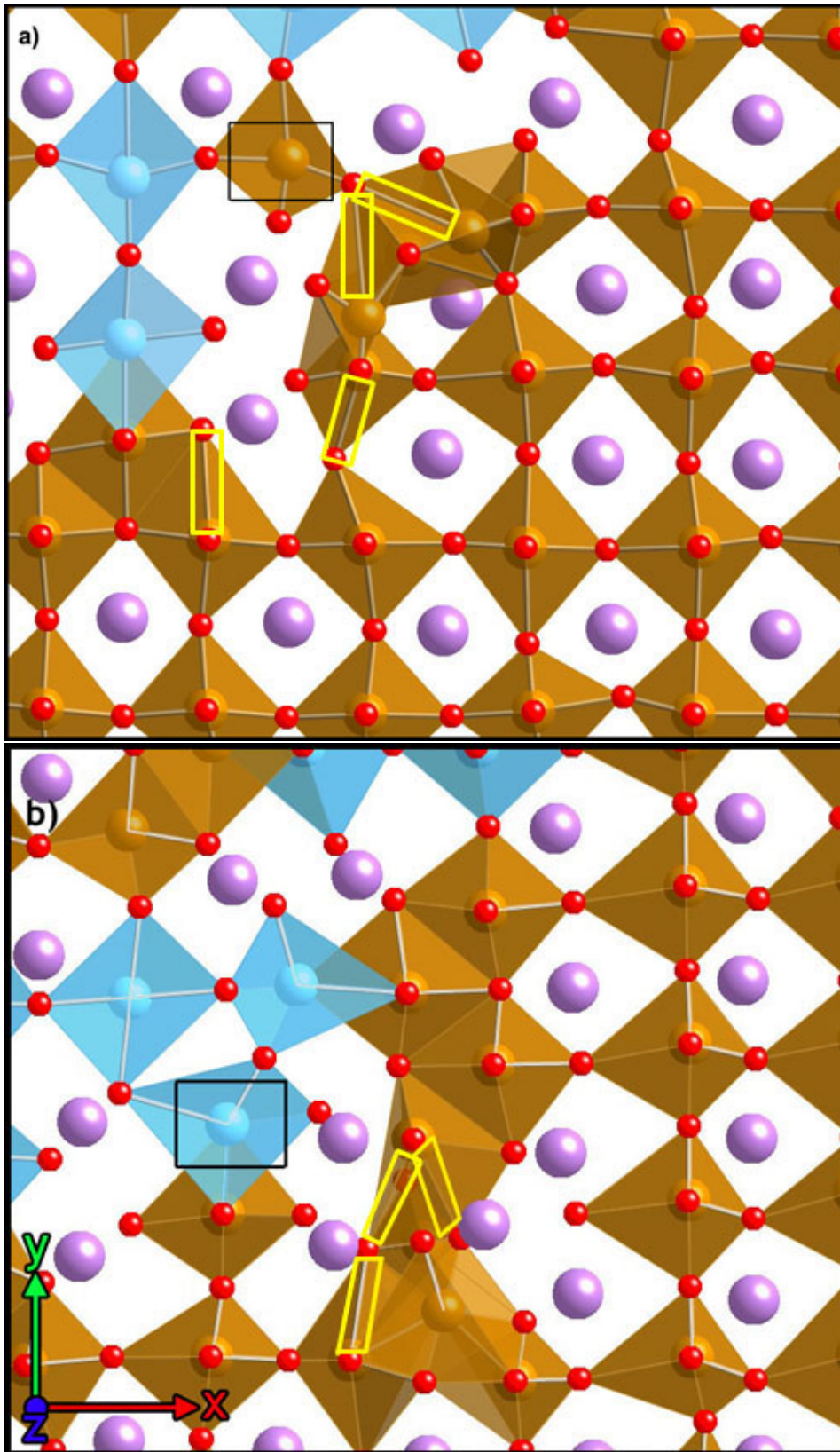


Figure 5.15: The possibility of different 3D structural model for of  $90^\circ$  corners on antiphase boundaries (APBs) have been reconstructed for both of a) HRTEM NCSI imaging mode, and b) HAADF imaging mode. Purple color indicates Bi atoms, red indicates oxygen atoms, light blue for Ti and brown for Fe. The black boxes show possible structures. While the yellow boxes show some of the unexpected bond lengths.

## 5.4 Conclusion

To summarise, a series of novel APBs with composition  $\text{Bi}_{0.85}\text{Nd}_{0.15}\text{Fe}_{0.9}\text{Ti}_{0.1}\text{O}_3$  have been observed and then modelled, namely APB cross and APB corner structures. The 3D structure of these unusual APBs were constructed by HAADF imaging combined with electron energy loss spectroscopy spectrum imaging (EELS-SI) to determine the ion positions. The model structure for the APB-cross structure was qualitatively certified by comparison with multislice frozen phonon image simulations. A preliminary analysis of the structure of two APB corners has been performed, and some initial models have been constructed, although it is clear further work would be needed to determine the structures unambiguously.

In order to have better signal to noise ratio and hence better image interpretation, a non-rigid registration procedure has been utilised. The effects of this procedure on some test data have been analysed quantitatively. Although the resulting images were better in appearance, the quantification on the HAADF images did not change significantly.

# Chapter 6

## Summary and future work

### 6.1 Summary

Previous studies have shown that combined Nd and Ti doping can cause beneficial property changes in  $\text{BiFeO}_3$ , with Nd (or other rare earths) improving the ferroelectric and piezoelectric properties [10, 29], and Ti reducing conductivity [10]. However, it was also found in previous work that overdoping with Ti can have unintended side-effects, with the formation of both Nd-rich nanorod defects [65, 66] and Ti-rich antiphase boundaries [67]. Previous studies of the antiphase boundaries has determined the structure of flat terraces parallel to  $[001]$  planes [68], steps away from these planes [68] and that these antiphase boundaries are charged [145, 67, 68]. The present thesis reports further more detailed analysis of such antiphase boundaries, including both probing the limits of what can be determined about polarisation in perovskites using atomic-resolution electron microscopy, and investigating hitherto unreported features of such antiphase boundaries.

Seeing as a reasonable amount has already been published about the atomic structure of novel antiphase boundaries in Nd,Ti co-doped  $\text{BiFeO}_3$ , this was used as a test for a detailed comparison of aberration-corrected HRSTEM and

HRTEM imaging for quantitative imaging of polarised perovskites. Whilst, it was found that similar structures are found by both imaging modes, there are significant quantitative and consistent differences in absolute atomic positions, especially for oxygen columns. This results in huge discrepancies in polarization measurements by the two techniques, where that made on HRTEM images is only around 40% of that measured from HRSTEM images. The reasons for these discrepancies were investigated exhaustively with the aid of image simulations and electrostatic calculations. For the HRTEM case, several effects can be considered. Firstly, it was found that there were consistent deviations of oxygen and iron positions in the vertical direction across the whole image, that are probably the result of sample mistilt: there was no influence of this effect on the polarisation calculations as the direction of the sample tilt in our case is perpendicular to the direction of polarisation. Secondly, the very thickness of the HRTEM sample may effect the polarisation where the effects of the surfaces on the electrostatics of the material surrounding an APB for a specimen  $<2\text{nm}$  thick will be significant. Thirdly, the electron channeling has the effect that the image of one oxygen column is significantly displaced from its actual position, which resulted in a reduction in the apparent polarisation. In the case of the HRSTEM data, there are at least two effects: Firstly, the tilt can shift the images of light atom columns with respect to heavy atom columns, although this effect was insignificant in the case analysed here. Additionally, the mirror symmetry of the polarisation across the charged APB made it possible to check for any mistilt in data and to choose the best areas for analysis where any mistilt did not influence the results. Secondly, it was also found that electron channelling shifts O column images towards the nearest Bi atom column resulting in an increase in the apparent polarisation.

According to the above discussion (significant oxygen column displacements in the images for both HRSTEM and HRTEM, and some reduction of actual

polarisation from bulk values for HRTEM due to the electrostatic effects of surfaces in an ultrathin sample), neither technique allows simple quantitative calculation of the polarisation from the raw atomic resolution data. Thus to perform quantitative measurements, the only way would be to perform image simulations, determine the imaging parameters, and then change the crystal model and re-simulate iteratively until the image can be matched to a simulation and the actual oxygen shifts measured from the model.

This detailed study of the reliability of different imaging modes was then followed by a detailed study of a crossing of two APBs using HRSTEM combining imaging and EELS-SI. HAADF imaging was used to find Bi and Fe/Ti positions through 2D Gaussian fitting. Registration and summation of fast scanned images was used to overcome sample drift whilst providing high signal to noise images.. Non-rigid registration was quantitatively compared with rigid registration and it was shown that non-rigid registration gave superior results when suitably optimised. It was shown that the APB cross is constructed from similar structural units to those found in steps on the APBs, mainly consisting of edge-sharing  $\text{FeO}_6$  octahedra. The resulting images showed new structural units not previously seen on antiphase boundary terraces or steps. Atomic resolution chemical mapping with EELS shows that the new structural units are Fe-rich, Ti-poor, as well as the expected results that terraces are Ti-rich and steps are Fe-rich [163]. A complete model of the cross was then constructed combining HAADF and EELS. This model was validated by image simulations. The new structural units with their edge-sharing octahedra have a similar atomic arrangement to iron atoms in maghemite, which is ferromagnetic, and it is therefore possible that these features also display permanent net magnetic moments below some critical temperature. Two different 90 degree corners on APBs have also been imaged in HRTEM and HRSTEM, which seem to be formed from similar structural units. Although in both cases an unambiguous reconstruction

of the atomic structure was impossible, but that it was also clear that these share similar characteristics to the cross, with edge-sharing octahedra linking up into larger units.

## 6.2 Future work

There are a number of possible future research directions suggested by things started in this thesis. Some of these are listed below.

1. If it is found that maghemite like regions in the APBs do indeed support permanent magnetic orderings at room temperature, it will be interesting to investigate whether these can be switched, and how correlated they are to the ordering in neighbouring maghemite like regions. If it were possible to produce a material containing a regular array of switchable ferromagnetic regions, it may be possible to use them for non-volatile information storage in magnetic bits at very high density. This could potentially be of great technological importance. Alternatively, it would be interesting to see if clear magnetic signals could be found from thin films of  $\text{BiFeO}_3\text{-PbTiO}_3$ , which have been found to contain a high density of such boundaries [164].
2. The fact that we found structures at boundary corners that could not be completely solved, suggests that there are more structures in these APBs to be investigated in the future, and this could yield more interesting new science.
3. Recent evidence from other work suggests that similar APBs can be generated in other perovskites including  $\text{Bi(Fe,Mn)O}_3$  [165] and  $(\text{La,Sr})\text{MnO}_3$  [D. Zhou, private communication, 2015] [166]. Further investigation of the structure, chemistry and properties of such boundaries should be undertaken, as they may have more widespread significance in complex perovskite ceramic and thin film growth. [test1]

# Bibliography

- [1] G. Catalan and J. F. Scott. “Physics and applications of bismuth ferrite”. *Advanced Materials* 21 (2009), 2463–2485.
- [2] L. W. Martin and R. Ramesh. “Multiferroic and magnetoelectric heterostructures”. *Acta Materialia* 60 (2012), 2449–2470.
- [3] M. Bibes and A. Barthélémy. “Multiferroics: Towards a magnetoelectric memory”. *Nature Materials* 7 (2008), 425–426.
- [4] S. H. Baek *et al.* “Ferroelastic switching for nanoscale non-volatile magnetoelectric devices”. *Nature Materials* 9 (2010), 309–314.
- [5] H. Béa, M. Gajek, M. Bibes, and A. Barthélémy. “Spintronics with multiferroics”. *Journal of Physics-Condensed Matter* 20 (2008), 434221.
- [6] B. G. Park *et al.* “A spin-valve-like magnetoresistance of an antiferromagnet-based tunnel junction”. *Nature Materials* 10 (2011), 347–351.
- [7] T. Moriya. “Anisotropic superexchange interaction and weak ferromagnetism”. *Physical Review* 120 (1960), 91–98.
- [8] N. A. Hill. “Why are there so few magnetic Ferroelectrics?” *The Journal of Physical Chemistry B* 104 (2000), 6694–6709.
- [9] K. Kalantari *et al.* “Ti-doping to reduce conductivity in  $\text{Bi}_{0.85}\text{Nd}_{0.15}\text{FeO}_3$  Ceramics”. *Advanced Functional Materials* 21 (2011), 3737–3743.

- [10] S. Karimi *et al.* “Crystal chemistry and domain structure of rare-earth doped BiFeO<sub>3</sub> ceramics”. *Journal of Materials Science* 44 (2009), 5102–5112.
- [11] H. Schmid. “Some symmetry aspects of ferroics and single phase multiferroics”. *Journal of Physics: Condensed Matter* 20 (2008), 434201.
- [12] D. Khomskii. “Classifying multiferroics: Mechanisms and effects”. *Physics* 2 (2009), 20.
- [13] URL: <http://www.murata.com/en-sg/support/faqs/products/capacitor/mlcc/char/0013>.
- [14] M. Zgonik *et al.* “Dielectric, elastic, piezoelectric, electro-optic, and elasto-optic tensors of BaTiO<sub>3</sub> crystals”. *Physical Review B* 50 (1994), 5941–5949.
- [15] A. Petraru, J. Schubert, M. Schmid, and C. Buchal. “Ferroelectric BaTiO<sub>3</sub> thin-film optical waveguide modulators”. *Applied Physics Letters* 81 (2002), 1375–1377.
- [16] C. Ederer and N. A. Spaldin. “Effect of epitaxial strain on the spontaneous polarization of thin film ferroelectrics”. *Physical Review Letters* 95 (2005), 1–5.
- [17] L. X. Zhang, W. Chen, and X. Ren. “Large recoverable electrostrain in Mn-doped (Ba,Sr) TiO<sub>3</sub> ceramics”. *Applied Physics Letters* 85 (2004), 5658–5660.
- [18] J. Shieh, J. H. Yeh, Y. C. Shu, and J. H. Yen. “Hysteresis behaviors of barium titanate single crystals based on the operation of multiple 90° switching systems”. *Materials Science and Engineering: B* 161 (2009), 50–54.
- [19] P. Ravindran *et al.* “Theoretical investigation of magnetoelectric behavior in BiFeO<sub>3</sub>”. *Physical Review B* 74 (2006), 224412.
- [20] D. Kan *et al.* “Universal behavior and electric-field-induced structural transition in rare-earth-substituted BiFeO<sub>3</sub>”. *Advanced Functional Materials* 20 (2010), 1108–1115.

- [21] A. Singh, V. Pandey, R. K. Kotnala, and D. Pandey. “Direct evidence for multiferroic magnetoelectric coupling in  $0.9\text{BiFeO}_3 - 0.1\text{BaTiO}_3$ ”. *Physical Review Letters* 101 (2008), 247602.
- [22] K. M. Ok, E. O. Chi, and P. S. Halasyamani. “Bulk characterization methods for non-centrosymmetric materials: second-harmonic generation, piezoelectricity, pyroelectricity, and ferroelectricity”. *Chemical Society Reviews* 35 (2006), 710–717.
- [23] A. Singh, C. Moriyoshi, Y. Kuroiwa, and D. Pandey. “Evidence for local monoclinic structure, polarization rotation, and morphotropic phase transitions  $(1 - x)\text{BiFeO}_3 - x\text{BaTiO}_3$  solid solutions: A high-energy synchrotron x-ray powder diffraction study”. *Physical Review B* 88 (2013), 024113.
- [24] W. Zhong, R. D. King-Smith, and D. Vanderbilt. “Giant LO-TO splittings in perovskite ferroelectrics”. *Physical Review letters* 72 (1994), 3618–3621.
- [25] Y-H. Chu, L. W. Martin, M. B. Holcomb and R. Ramesh. “Controlling magnetism with multiferroics”. *Materials Today* 10 (2007), 16–23.
- [26] V. M. Goldschmidt. “Die gesetze der krystallochemie”. *Naturwissenschaften* 14 (1926), 477–485.
- [27] S. Karimi, I. M. Reaney, I. Levin, and I. Sterianou. “Nd-doped  $\text{BiFeO}_3$  ceramics with antipolar order”. *Applied Physics Letters* 94 (2009), 112903.1–112903.3.
- [28] I. Levin *et al.* “Reorientation of magnetic dipoles at the antiferroelectric-paraelectric phase transition of  $\text{Bi}_{1-x}\text{Nd}_x\text{FeO}_3 (0.15 \leq x \leq 0.25)$ ”. *Physical Review B* 81 (2010), 020103.
- [29] D. Kan *et al.* “Universal behavior and electric-field-induced structural transition in rare-earth-substituted  $\text{BiFeO}_3$ ”. *Advanced Functional Materials* 20 (2010), 1108–1115.

- [30] I. MacLaren *et al.* “Atomic-scale imaging and quantification of electrical polarisation in incommensurate antiferroelectric lanthanum-doped lead zirconate titanate”. *Advanced Functional Materials* 22 (2011), 261–266.
- [31] P. Curie. “Sur la symétrie dans les phénomènes physiques, symétrie d’un champ électrique et d’un champ magnétique”. *Journal of Theoretical and Applied Physics* 3 (1894), 393–415.
- [32] E. Ascher, H. Rieder, H. Schmid, and H. Stössel. “Some properties of ferromagnetoelectric Nickel-Iodine Boracite,  $\text{Ni}_3\text{B}_7\text{O}_{13}\text{I}$ ”. *Journal of Applied Physics* 37 (1966), 1404–1405.
- [33] J. H. Vansanten and G. H. Jonker. “Electrical conductivity of ferromagnetic compounds of manganese with perovskite structure”. *Physica* 16 (1950), 599–600.
- [34] A. Urushibara *et al.* “Insulator-metal transition and giant magnetoresistance in  $\text{La}_{1-x}\text{Sr}_x\text{MnO}_3$ ”. *Physical Review B* 51 (1995), 14103–14109.
- [35] M. Paraskevopoulos *et al.* “The phase diagram and optical properties of  $\text{La}_{1-x}\text{Sr}_x\text{MnO}_3$  for  $x \leq 0.2$ ”. *Journal of Magnetism and Magnetic Materials* 211 (2000), 118–127.
- [36] A-M. Haghiri-Gosnet and J-P. Renard. “CMR manganites: physics, thin films and devices”. *Journal of Physics D-Applied Physics* 36 (2003), R127–R150.
- [37] Y. Tokura. “Critical features of colossal magnetoresistive manganites”. *Reports on Progress in Physics* 69 (2006), 797–851.
- [38] T. Koyama, Y. Togawa, K. Takenaka, and S. Mori. “Ferromagnetic microstructures in the ferromagnetic metallic phase of  $\text{La}_{0.825}\text{Sr}_{0.175}\text{MnO}_3$ ”. *Journal of Applied Physics* 111 (2012), 07B104.1–07B104.3.

- [39] I. Sosnowska, T. Peterlinneumaier, and E. Steichele. “Spiral magnetic ordering in bismuth ferrite”. *Journal of Physics C-Solid State Physics* 15 (1982), 4835–4846.
- [40] I. Sosnowska, M. Loewenhaupt, W.I.F. David and R.M. Ibberson. “Investigation of the unusual magnetic spiral arrangement in  $\text{BiFeO}_3$ ”. *Physica B: Condensed Matter* 180 (1992), 117–118.
- [41] J. R. Teague, R. Gerson, and W. J. James. “Dielectric hysteresis in single crystal  $\text{BiFeO}_3$ ”. *Solid State Communications* 8 (1970), 1073–1074.
- [42] S. V. Kiselev, R. P. Ozerov, and G. S. Zhdanov. “Detection of magnetic order in ferroelectric  $\text{BiFeO}_3$  by neutron diffraction”. *Soviet Physics Doklady* 7 (1963), 742–744.
- [43] W. Eerenstein, N. D. Mathur, and J. F. Scott. “Multiferroic and magnetoelectric materials”. *Nature* 442 (2006), 759–765.
- [44] B. Yu, M. Li, J. Liu, and D. Guo. “Effects of ion doping at different sites on electrical properties of multiferroic  $\text{BiFeO}_3$  ceramics”. *Journal of Physics D: Applied Physics* 41 (2008), 065003.1–065003.4.
- [45] T. Katsufuji *et al.* “Dielectric and magnetic anomalies and spin frustration in hexagonal  $\text{RMnO}_3$  (R=Y, Yb, and Lu)”. *Physical Review B* 64 (2001), 104419.1–104419.6.
- [46] T. Kimura *et al.* “Magnetocapacitance effect in multiferroic  $\text{BiMnO}_3$ ”. *Physical Review B* 67 (2003), 180401.1–180401.4.
- [47] R. Seshadri and N. A. Hill. “Visualizing the role of Bi 6s “lone pairs” in the off-center distortion in ferromagnetic  $\text{BiMnO}_3$ ”. *Chemistry of Materials* 13 (2001), 2892–2899.
- [48] D. Kothari *et al.* “Study of the effect of Mn doping on the  $\text{BiFeO}_3$  system”. *Journal of Physics: Condensed Matter* 19 (2007), 136202.1–136202.8.

- [49] M. Kumar and K. L. Yadav. “Study of room temperature magnetoelectric coupling in Ti substituted bismuth ferrite system”. *Journal of Applied Physics* 100 (2006), 074111.1–074111.4.
- [50] C. F. Chung, J. P. Lin, and J. M. Wu. “Influence of Mn and Nb dopants on electric properties of chemical-solution-deposited BiFeO<sub>3</sub> films”. *Applied Physics Letters* 88 (2006), 242909.1–242909.3.
- [51] M. Fiebig. “Revival of the magnetoelectric effect”. *Journal of Physics D: Applied Physics* 38 (2005), R123–R152.
- [52] J. Wang *et al.* “Epitaxial BiFeO<sub>3</sub> multiferroic thin film heterostructures”. *Science* 299 (2003), 1719–1722.
- [53] D. Lebeugle *et al.* “Electric-field-induced spin flop in BiFeO<sub>3</sub> single crystals at room temperature”. *Physical Review Letters* 100 (2008), 227602.1–227602.4.
- [54] R. J. Zeches *et al.* “A strain-driven morphotropic phase boundary in BiFeO<sub>3</sub>”. *Science* 326 (2009), 977–980.
- [55] J. X. Zhang *et al.* “Microscopic origin of the giant ferroelectric polarization in tetragonal-like BiFeO<sub>3</sub>”. *Physical Review Letters* 107 (2011), 147602.1–147602.5.
- [56] M. D. Rossell *et al.* “Atomic structure of highly strained BiFeO<sub>3</sub> thin films”. *Physical Review Letters* 108 (2012), 047601.
- [57] H. J. Lee *et al.* “Depth resolved lattice-charge coupling in epitaxial BiFeO<sub>3</sub> thin film”. *Scientific Reports* 6 (2016), 1–6.
- [58] A. J. Hatt, N. A. Spaldin, and C. Ederer. “Strain-induced isosymmetric phase transition in BiFeO<sub>3</sub>”. *Physical Review B* 81 (2010), 054109.1–054109.5.
- [59] Y. Li *et al.* “Giant optical enhancement of strain gradient in ferroelectric BiFeO<sub>3</sub> thin films and its physical origin”. *Scientific Reports* 5 (2015), 1–7.

- [60] A. Morelli *et al.* “Deterministic switching in bismuth ferrite nanoislands”. *Nano Letters* 16 (2016), 5228–5234.
- [61] H. Wen *et al.* “Capturing ultrafast photoinduced local structural distortions of BiFeO<sub>3</sub>”. *Scientific Reports* 5 (2015), 1–8.
- [62] D. Chen *et al.* “Interface engineering of domain structures in BiFeO<sub>3</sub> thin films”. *Nano Letters* 17 (2017), 486–493.
- [63] A. Y. Borisevich *et al.* “Atomic-scale evolution of modulated phases at the ferroelectric–antiferroelectric morphotropic phase boundary controlled by flexoelectric interaction”. *Nature Communications* 3 (2012), 1–8.
- [64] E. Aksel and J. L. Jones. “Advances in lead-free piezoelectric materials for sensors and actuators”. *Sensors* 10 (2010), 1935–1954.
- [65] I. M. Reaney *et al.* “Defect chemistry of Ti-doped antiferroelectric Bi<sub>0.85</sub>Nd<sub>0.15</sub>FeO<sub>3</sub>”. *Applied Physics Letters* 100 (2012), 182902.1–182902.3.
- [66] I. MacLaren *et al.* “Novel nanorod precipitate formation in neodymium and titanium codoped bismuth ferrite”. *Advanced Functional Materials* 23 (2013), 683–689.
- [67] I. MacLaren *et al.* “Local stabilisation of polar order at charged antiphase boundaries in antiferroelectric (Bi<sub>0.85</sub>Nd<sub>0.15</sub>)(Ti<sub>0.1</sub>Fe<sub>0.9</sub>)O<sub>3</sub>”. *APL Materials* 1 (2013), 021102.1–021102.7.
- [68] I. MacLaren *et al.* “The atomic structure and chemistry of Fe-rich steps on antiphase boundaries in Ti-doped Bi<sub>0.9</sub>Nd<sub>0.15</sub>FeO<sub>3</sub>”. *APL Materials* 2 (2014), 066106.1–066106.6.
- [69] H. Rose and W. Wan. “Aberration correction in electron microscopy”. *IEEE* (2005), 44–48.
- [70] M. Haider *et al.* “A spherical-aberration-corrected 200 kV transmission electron microscope”. *Ultramicroscopy* 75 (1998), 53–60.

- [71] C-L. Jia, M. Lentzen, and K. Urban. “High-resolution transmission electron microscopy using negative spherical aberration”. *Microscopy and Microanalysis* 10 (2004), 174–184.
- [72] D. B. Williams and C. B. Carter. Springer Science & Business Media, LLC, 2009.
- [73] M. H. Loretto. *Electron beam analysis of materials*. Chapman & Hall, London, 1994. Chap. 3 (Layout and Operational Modes of Electron Beam Instruments).
- [74] H. Kohl *et al.* *Transmission Electron Microscopy*. Springer, 2007. Chap. 4 (Elements of a Transmission Electron Microscope).
- [75] R. F. Egerton. *Electron energy-loss spectroscopy in the electron microscope*. Springer Science & Business Media, LLC, 2011. Chap. 2 (Energy-Loss Instrumentation).
- [76] O. Scherzer. “Über einige Fehler von Elektronenlinsen”. German. *Zeitschrift für Physik* 101 (1936), 593–603.
- [77] O. Scherzer. “The theoretical resolution limit of the electron microscope”. *Journal of Applied Physics* 20 (1949), 20–29.
- [78] O. Scherzer. “Sphärische und chromatische Korrektur von Elektronenlinsen”. German. *Optik* 2 (1947), 114–132.
- [79] P. W. Hawkes and E. Kasper. *Principles of Electron Optics: Wave optics*. Academic Press, London and San Diego, 1994. Chap. 41 (Aberration Correction).
- [80] D. Typke and K. Dierksen. “Determination of image aberration in high-resolution electron-microscopy using diffractogram and cross-correlation methods”. *Optik* 99 (1995), 155–166.

- [81] S. Uhlemann and M. Haider. “Residual wave aberrations in the first spherical aberration corrected transmission electron microscope”. *Ultramicroscopy* 72.3-4 (1998), 109–119.
- [82] O. L. Krivanek, N. Dellby, and A. R. Lupini. “Towards sub-Å electron beams”. *Ultramicroscopy* 78 (1999), 1–11.
- [83] J. Zach and M. Haider. “Aberration correction in a low voltage SEM by a multipole corrector”. *Nuclear Instruments and Methods in Physics Research Section A: Accelerators, Spectrometers, Detectors and Associated Equipment* 363 (1995), 316–325.
- [84] M. Haider *et al.* “Electron microscopy image enhanced”. *Nature* 392 (1998), pp.768–769.
- [85] P. D. Nellist. *Aberration-corrected analytical transmission electron microscopy*. Ed. by R. Brydson *et al.* John Wiley and sons, Ltd, 2011. Chap. 4 (*Lens aberrations: Diagnosis and correction*).
- [86] M. U. Farooq *et al.* “Electron backscatter diffraction mapping of herringbone domain structures in tetragonal piezoelectrics”. *Journal of Applied Physics* 104 (2008), 024111.1–024111.8.
- [87] M. U. Farooq *et al.* “Using EBSD and TEM-Kikuchi patterns to study local crystallography at the domain boundaries of lead zirconate titanate”. *Journal of Microscopy* 230 (2008), 445–454.
- [88] J. M. Cowley. “Image contrast in a transmission scanning electron microscope”. *Applied Physics Letters* 15 (1969), 58–59.
- [89] A. Howie. “Image contrast and localized signal selection techniques”. *Journal of Microscopy* 117 (1979), 11–23.

- [90] C. R. Hall and P. B. Hirsch. “Effect of thermal diffuse scattering on propagation of high energy electrons through crystals”. *Proceedings of the Royal Society of London A: Mathematical, Physical and Engineering Sciences* 286 (1965), 158–177.
- [91] S. J. Pennycook and D. E. Jesson. “High-resolution incoherent imaging of crystals”. *physical Review Letters* 64 (1990), 938–941.
- [92] P. E. Batson, N. Dellby, and O. L. Krivanek. “Sub-angstrom resolution using aberration corrected electron optics”. *Nature* 418 (2002), 617–620.
- [93] P. D. Nellist *et al.* “Direct sub-angstrom imaging of a crystal lattice”. *Science* 305 (2004), 1741–1741.
- [94] J. E. Allen *et al.* “High-resolution detection of Au catalyst atoms in Si nanowires”. *Nature Nanotechnology* 3 (2008), 168–173.
- [95] O. L. Krivanek *et al.* “Atom-by-atom structural and chemical analysis by annular dark-field electron microscopy”. *Nature* 464 (2010), 571–574.
- [96] C.E. Hall. *Introduction to electron microscopy*. McGraw-Hill, New York, 1953.
- [97] P. D. Nellist. *Aberration-corrected analytical transmission electron microscopy*. Ed. by R. Brydson *et al.* John Wiley and sons, Ltd, 2011. Chap. 5 (*Theory and Simulations of STEM Imaging*).
- [98] T. Mitsui and J. Furichi. “Domain structure of rochelle salt and  $KH_2PO_4$ ”. *Physical Review* 90 (1953), 193–202.
- [99] C. Jeanguillaume and C. Colliex. “Spectrum-image - The next step in EELS digital acquisition and processing”. *Ultramicroscopy* 28 (1989), 252–257.
- [100] B. Schaffer, W. Grogger, and G. Kothleitner. “Automated spatial drift correction for EFTEM image series”. *Ultramicroscopy* 102 (2004), 27–36.

- [101] L. Jones. *Smart align imaging processing software*. URL: <http://lewysjones.com/designing-robust-procedures-for-rigid-a%20d-non-rigid-registration-of-stem-image-data/>.
- [102] L. Houben. *iMtools imaging processing software*. URL: <http://www.er%20org/centre/software/imtools.htm>.
- [103] J. Barthel. “Time-efficient frozen phonon multislice calculations for image simulations in high-resolution STEM”. *EMC 2012 15th European Microscopy Congress 16-21, Manchester, United Kingdom* (2012).
- [104] A. M. Sanchez *et al.* “An approach to the systematic distortion correction in aberration-corrected HAADF images”. *Journal of Microscopy* 221 (2006), 1–7.
- [105] D. A. Muller *et al.* “Room design for high-performance electron microscopy”. *Ultramicroscopy* 106 (2006), 1033–1040.
- [106] L. Jones and P. D. Nellist. “Post-processing of STEM data for instability and drift compensation”. *Microscopy and Microanalysis* 18 (2012), 1232–1233.
- [107] I. MacLaren and Q. M. Ramasse. “Aberration-corrected scanning transmission electron microscopy for atomic-resolution studies of functional oxides”. *International Materials Reviews* 59 (2014), 115–131.
- [108] I. MacLaren *et al.* “On the origin of differential phase contrast at a locally charged and globally charge-compensated domain boundary in a polar-ordered material”. *Ultramicroscopy* 154 (2015), 57–63.
- [109] J. N. Sarvaiya, S. Patnaik, and K. Kothari. “Image registration using log polar transform and phase correlation to recover higher scale”. *Journal of Pattern Recognition Research* 7 (2012), 90–105.

- [110] Y. Keller, A. Averbuch, and M. Israeli. “Pseudopolar-based estimation of large translations, rotations, and scalings in images”. *IEEE Transactions on Image Processing* 14 (2005), 12–22.
- [111] L. Jones and P. D. Nellist. “Identifying and correcting scan noise and drift in the scanning transmission electron microscope”. *Microscopy and Microanalysis* 19 (2013), 1050–1060.
- [112] L. Jones *et al.* “Smart Align—a new tool for robust non-rigid registration of scanning microscope data”. *Advanced Structural and Chemical Imaging* 1 (2015), 1–16.
- [113] B. Berkels *et al.* “Optimized imaging using non-rigid registration”. *Ultramicroscopy* 138 (2014), 46–56.
- [114] A. B. Yankovich *et al.* “Picometre-precision analysis of scanning transmission electron microscopy images of platinum nanocatalysts”. *Nature Communications* 5 (2014), 1–7.
- [115] A. Rečnik, G. Möbus, and S. Šturm. “Image-warp: A real-space restoration method for high-resolution STEM images using quantitative HRTEM analysis”. *Ultramicroscopy* 103 (2005), 285–301.
- [116] Pascal C., X. Pennec, and N. Ayache. “Fast non rigid matching by gradient descent: Study and improvements of the ”demons” algorithm”. PhD thesis. 1999.
- [117] Julie G. *et al.* “Direct observation of ferroelectric domain walls in LiNbO<sub>3</sub>: wall-meanders, kinks, and local electric charges”. *Advanced Functional Materials* 26 (2016), 7599–7604.
- [118] L. Jones *et al.* “Optimising multi-frame ADF-STEM for high-precision atomic-resolution strain mapping”. *Ultramicroscopy* 179 (2017), 57–62.

- [119] T. Vogt, D. A. Blom, L. Jones, and D. J. Buttrey. “ADF-STEM imaging of nascent phases and extended disorder within the Mo–V–Nb–Te–O catalyst system”. *Topics in Catalysis* 59 (2016), 1489–1495.
- [120] L. Houben. *iMtools*. URL: (<http://www.er-c.org/methods/sta./houben.htm>).
- [121] L. Houben. *iMtools*. URL: <http://www.er-c.org/centre/software/imtools.htm>.
- [122] L. Houben, A. Thust, and K. Urban. “Atomic-precision determination of the reconstruction of a 90° tilt boundary in YBa<sub>2</sub>Cu<sub>3</sub>O<sub>7-δ</sub> by aberration corrected HRTEM”. *Ultramicroscopy* 106 (2006), 200–214.
- [123] E. J Kirkland, R. F. Loane, and J. Silcox. “Simulation of annular dark field stem images using a modified multislice method”. *Ultramicroscopy* 23 (1987), 77–96.
- [124] J. Kirkland. *Advanced computing in electron microscopy*. Springer Science & Business Media, LLC, 2010.
- [125] P. G. Self, M. A. O’Keefe, P. R. Buseck, and A. E. C. Spargo. “Practical computation of amplitudes and phases in electron diffraction”. *Ultramicroscopy* 11 (1983), 35–52.
- [126] J. Kirkland. *Advanced computing in electron microscopy*. Springer Science & Business Media, LLC, 2010.
- [127] R. F. Loane, P. Xu, and J. Silcox. “Thermal vibrations in convergent-beam electron diffraction”. *Acta Crystallographica Section A* 47 (1991), 267–278.
- [128] C. Koch. “Determination of core structure periodicity and point defect density along dislocations”. PhD thesis. 2002.

- [129] D. Rez, P. Rez, and I. Grant. “Dirac–Fock calculations of X-ray scattering factors and contributions to the mean inner potential for electron scattering”. *Acta Crystallographica Section A* 50 (1994), 481–497.
- [130] J. Bobynko, I. MacLaren, and A. J. Craven. “Spectrum imaging of complex nanostructures using DualEELS: I. digital extraction replicas”. *Ultramicroscopy* 149 (2015), 9–20.
- [131] G. Lucas, P. Burdet, M. Cantoni, and C. Hébert. “Multivariate statistical analysis as a tool for the segmentation of 3D spectral data”. *Micron* 52 (2013), 49–56.
- [132] I. T. Jolliffe. *Principal Component Analysis*. Springer, New York, 2002.
- [133] M. Watanabe, D. B. Williams, and M. G. Burke. “Atomic-level analytical electron microscopy of diffusional phase transformations”. *Proceedings of an International Conference on Solid-Solid Phase Transformations in Inorganic Materials 2005*. Ed. by J.M. Howe *et al.* Vol. 2. 2005.
- [134] E. R. Malinowski. *Factor analysis in chemistry*. John Wiley & Sons, Ltd., 2002.
- [135] M. G. Burke, M. Watanabe, D. B. Williams, and J. M. Hyde. “Quantitative characterization of nanoprecipitates in irradiated low-alloy steels: Advances in the application of FEG-STEM quantitative microanalysis to real materials”. *Journal of Materials Science* 41 (2006), 4512–4522.
- [136] M. Bosman, M. Watanabe, D.T.L. Alexander, and V.J. Keast. “Mapping chemical and bonding information using multivariate analysis of electron energy-loss spectrum images”. *Ultramicroscopy* 106 (2006), 1024–1032.
- [137] M. Watanabe *et al.* “Applications of electron energy-loss spectrometry and energy filtering in an aberration-corrected JEM-2200FS STEM/TEM”. *Microscopy and Microanalysis* 13 (2007), 1264–1265.

- [138] M. Watanabe, E. Okunishi, and K. Ishizuka. “Analysis of spectrum-imaging datasets in atomic-resolution electron microscopy”. *Microscopy and Analysis* 23 (2009), 5–7.
- [139] I. MacLaren *et al.* “Atomic-scale imaging and quantification of electrical polarisation in incommensurate antiferroelectric lanthanum-doped lead zirconate titanate”. *Advanced Functional Materials* 22 (2012), 261–266.
- [140] C-L. Jia *et al.* “Direct observation of continuous electric dipole rotation in flux-closure domains in ferroelectric  $\text{Pb}(\text{Zr},\text{Ti})\text{O}_3$ ”. *Science* 331 (2011), 1420–1423.
- [141] G. Catalan *et al.* “Flexoelectric rotation of polarization in ferroelectric thin films”. *Nature Materials* 10 (2011), 963–967.
- [142] H. J. Chang *et al.* “Atomically resolved mapping of polarization and electric fields across ferroelectric/oxide interfaces by z-contrast imaging”. *Advanced Materials* 23 (2011), 2474–2479.
- [143] C. T. Nelson *et al.* “Spontaneous vortex nanodomain arrays at ferroelectric heterointerfaces”. *Nano Letters* 11 (2011), 828–834.
- [144] A. Lubk *et al.* “Evidence of sharp and diffuse domain walls in  $\text{BiFeO}_3$  by means of unit-cell-wise strain and polarization maps obtained with high resolution scanning transmission electron microscopy”. *Physical Review Letters* 109 (2012), 047601.1–047601.5.
- [145] C-L. Jia *et al.* “Atomic-scale study of electric dipoles near charged and uncharged domain walls in ferroelectric films”. *Nature Materials* 7 (2008), 57–61.
- [146] L. Q. Wang *et al.* “Atomic-resolution STEM imaging and EELS-SI of defects in  $\text{BiFeO}_3$  ceramics co-doped with Nd and Ti”. *Electron microscopy and*

- analysis group conference 2011 (EMAG 2011)*. Vol. 371. Journal of Physics Conference Series. 2012.
- [147] J. Barthel. *Dr. Probe - STEM multislice image calculation program*. URL: <http://lewysjones.com/designing-robust-procedures-for-rigid-a%20d-non-rigid-registration-of-stem-image-data/>.
- [148] H. Hashimoto, A. Howie, and M. J. Whelan. “Anomalous electron absorption effects in metal foils: Theory and comparison with experiment”. *Proceedings of the Royal Society of London A: Mathematical, Physical and Engineering Sciences* 269 (1962), 80–103.
- [149] A. Thust. “High-Resolution transmission electron microscopy on an absolute contrast scale”. *Physical Review letters* 102 (2009), 220801.1–220801.4.
- [150] J. Li *et al.* “Dramatically enhanced polarization in (001), (101), and (111)BiFeO<sub>3</sub> thin films due to epitaxial-induced transitions”. *Applied Physics Letters* 84 (2004), 5261–5263.
- [151] R. E. Dunin-Borkowski and W. O. Saxton. “The electrostatic contribution to the forward-scattering potential at a space charge layer in high-energy electron diffraction. II. Fringing fields”. *Acta Crystallographica Section A* 53 (1997), 242–250.
- [152] P. K. Somodi *et al.* “Finite element simulations of electrostatic dopant potentials in thin semiconductor specimens for electron holography”. *Ultramicroscopy* 134 (2013), 160–166.
- [153] A. C. Twitchett, R. E. Dunin-Borkowski, R. F. Broom, and PA Midgley. “Quantitative electron holography of biased semiconductor devices”. *Journal of Physics-condensed Matter* 16 (2004), S181–S192.
- [154] W.J. Duffin. *Electricity and magnetism*. McGRAW-HILL Book Company (UK) Limited., 1980.

- [155] D. Zhou *et al.* “Sample tilt effects on atom column position determination in ABF-STEM imaging”. *Ultramicroscopy* 160 (2016), 110–117.
- [156] O. I. Lebedev *et al.* “A study of the domain structure of epitaxial  $La_{1-x}Ca_xMnO_3$  films by high-resolution transmission electron microscopy”. *Philosophical Magazine A* 79 (1999), 1461–1478.
- [157] J. B. Neaton *et al.* “First-principles study of spontaneous polarization in multiferroic  $BiFeO_3$ ”. *Physical Review B* 71 (2005), 014113.1–014113.8.
- [158] F. Kubel and H. Schmid. “Structure of a ferroelectric and ferroelastic monodomain crystal of the perovskite  $BiFeO_3$ ”. *Acta Crystallographica Section B: Structural Science* 46 (1990), 698–702.
- [159] C. Greaves. “A powder neutron diffraction investigation of vacancy ordering and covalence in  $\gamma$ - $Fe_2O_3$ ”. *Journal of Solid State Chemistry* 49 (1983), 325–333.
- [160] M. P. Morales, C. Pecharroman, T. G. Carreno, and C. J. Serna. “Structural characteristics of uniform  $\gamma$ - $Fe_2O_3$  particles with different axial (length/width) ratios”. *Journal Solid State Chemistry* 108 (1994), 158–163.
- [161] M. P. Morales, C. J. Serna, F. Bodker, and S. Morup. “Spin canting due to structural disorder in maghemite”. *Journal of Pphysics-Condenced Matter* 9 (1997), 5461–5467.
- [162] P. Schattschneider *et al.* “Detection of magnetic circular dichroism using a transmission electron microscope”. *Nature* 441 (2006), 486–488.
- [163] J. M. Salih *et al.* “Maghemite-like regions at crossing of two antiphase boundaries in doped  $BiFeO_3$ ”. *Materials Science and Technology* 32 (2016), 242–247.
- [164] F. East. Private communication. 2015.

- [165] I. MacLaren *et al.* “Strain localization in thin films of  $\text{Bi}(\text{Fe},\text{Mn})\text{O}_3$  due to the formation of stepped  $\text{Mn}^{4+}$ -Rich antiphase boundaries”. *Nanoscale Research Letters* 10 (2015), 1–7.
- [166] D. Zhou. Private communication. 2015.